January 2013

Hydrogen Storage in Hypercrosslinked Polystyrene and Li-Mg-N-H Complex Hydride

Dervis Emre Demirocak
University of South Florida, emredemirocak@yahoo.com

Hydrogen Storage in Hypercrosslinked Polystyrene and Li-Mg-N-H Complex Hydride

by

Derviş Emre Demirocak

A dissertation submitted in partial fulfillment
of the requirements for the degree of
Doctor of Philosophy
Department of Mechanical Engineering
College of Engineering
University of South Florida

Co-Major Professor: Elias K Stefanakos, Ph.D.
Co-Major Professor: Ashok Kumar, Ph.D.
Yogi Goswami, Ph.D.
Manoj K. Ram, Ph.D.
Muhammad M. Rahman, Ph.D.
Shengqian Ma, Ph.D.

Date of Approval:
April 2, 2013

Keywords: porous polymers, spillover, hydrogen storage measurements,
lithium amide, magnesium hydride

Dedication

To my parents Sabire and Yılmaz Demirocak for their continued support throughout my life.

Acknowledgments

I would like to thank my research supervisors Dr. Elias K Stefanakos, Dr. Yogi Goswami and Dr. Ashok Kumar for giving me the opportunity to work in this hydrogen storage project, and for their scientific guidance, support and kindness during my Ph.D. studies at the Clean Energy Research Center. I also would like to thank Dr. Sesha Srinivasan and Dr. Manoj K. Ram for their support on all aspects of the experimental works in this project, the invaluable discussions to overcome the challenges, and for their mentorship and friendship. Moreover, I would like to thank Dr. Muhammad Rahman for his precious advice throughout my Ph.D. studies. Additionally, I am deeply grateful to Dr. Shengqian Ma, Dr. Xisen Wang and Dr. John Kuhn for their scientific guidance and helpfulness. In addition, I would also like to thank Mark A. Ross for being the chairperson of my Ph.D. defense. Finally, I would like to thank the US Department of Energy through the Florida Hydrogen Initiative (FHI) administered by the Florida Solar Energy Center (FSEC), University of Central Florida for supporting this project.

Additionally, I would like to thank Ginny Cosmides and Barbara Graham at the Clean Energy Research Center for their support, friendship and understanding.

This work would not be possible without the support of my friends in Tampa. I would like to thank Aret Karademir, Onursal Önen, Sinan Önal, Çiğdem Akan, Gökmen Demirkaya, Jamie Trahan, John Shelton and Anthony D'Angelo who made my life bearable during my Ph.D. studies.

Finally, I would like to thank my parents, Sabire and Yılmaz Demirocak for all they did throughout my life and for their understanding, support and patience during my graduate studies abroad.

Table of Contents

List of Tables

List of Figures

Abstract

In this dissertation, hydrogen storage enhancement in hypercrosslinked polystyrene, effects of single walled carbon nanotubes (SWCNTs) supported ruthenium (Ru) catalyst on the kinetics and ammonia suppression in the $LiNH_2$–MgH_2 complex hydride system and the accuracy of hydrogen storage measurements are investigated in detail.

High surface area physisorption materials are of interest for room temperature hydrogen storage enhancement by spillover. Six different commercially available hypercrosslinked polystyrenes are screened by considering the specific surface area, average pore size, pore volume, and adsorption enthalpy. MN270 is selected mainly due to its high surface area and narrow pores for investigation of the spillover enhancement at room temperature. Two different platinum (Pt) doped MN270 samples are prepared by wet impregnation (MN270-6wt%Pt) and bridge building technique (MN270-bridged) with an average Pt particle size of 3.9 and 9.9nm, respectively, as obtained from X-ray diffraction analysis. Pt doping altered the surface property of MN270, and reduced the nitrogen and hydrogen uptake at 77 K and 1 atm due to pore blocking. The room temperature hydrogen uptake at 100 atm demonstrated a 10% enhancement for the MN270-bridged (0.36 wt. %) compared to the pristine MN270 (0.32 wt. %), but did not show any enhancement for the MN270-6wt%Pt under the same conditions. The hydrogen uptake of MN270-bridged has little value for practical applications; however, it showed the effectiveness of the bridge building technique.

The $LiNH_2 – MgH_2$ (2:1.1) complex metal hydride system (Li-Mg-N-H), which is prepared by high energy ball milling, is investigated in terms of the hydrogen ab/desorption kinetics and the concomitant NH_3 emission levels. By selecting more intense ball milling parameters, the hydrogen ab/desorption kinetics were improved and the NH_3 emission reduced. However, it is shown that NH_3 emission cannot be completely eliminated by ball milling. The hydrogen desorption kinetics of the Li-Mg-N-H system is much faster than the absorption kinetics at a specific T and P, but the desorption kinetics degraded considerably over a number of cycles as opposed to the stabilized absorption kinetics. Furthermore, SWCNTs and 20 wt. % Ru doped SWCNTs (SWCNT-20Ru) are utilized as catalysts to study their effects on NH_3 emission and kinetics characteristics of the Li-Mg-N-H system. The SWCNT doped sample did not show any kinetics improvement, whereas the SWCNT-20Ru doped sample showed similar kinetics performance as that of the base sample. More importantly, the presence of SWCNT increased the NH_3 emission as compared to the base sample. On the other hand, SWCNT-20Ru doping reduced the NH_3 emission compared to the SWCNT doping, but did not eliminate it completely. As revealed from the mass spectrometry signals, the SWCNT-20Ru catalyst starts to decompose NH_3 at a temperature as low as 200°C. However, an optimal catalyst still needs to be developed by fine tuning the Ru particle size and the SWCNT structural properties to maximize its effectiveness to suppress NH_3 release in the Li-Mg-N-H system.

The design of a volumetric measurement apparatus is studied by means of an uncertainty analysis to provide guidelines for optimum hydrogen sorption measurements. The reservoir volume should be as small as possible (i.e., 10 cc) to minimize the

uncertainty. In addition, the sample mass loading has a profound effect on the uncertainty and the optimum loading is a function of the sample's intrinsic storage capacity. In general, the higher the sample mass loading the lower is the uncertainty, regardless of any other parameters. In cases where the material to be tested is not available in gram quantities, the use of high accuracy pressure and temperature transducers significantly mitigates the uncertainty in the sample's hydrogen uptake. Above all, the thermal equilibration time is an important parameter for high accuracy measurements and needs to be taken into consideration at the start of the measurements. Based on computational analysis, a 5 min wait time is required for achieving thermal equilibrium when the instrument enclosure temperature is different than the ambient temperature.

Chapter 1. Introduction[1]

1.1. Motivation behind the Hydrogen Economy

Depletion of fossil fuels especially oil in the near-future [1,2], rising environmental concerns due to global warming as a result of excessive anthropogenic CO_2 emission [3] and the necessity of a secure energy supply [4-6] have created worldwide interest in renewable energy technologies in the last decade. Among many forms of renewable energy, hydrogen attracted attention mainly as an energy carrier due to its potential for the replacement of oil in stationary and mobile applications. When hydrogen is utilized in internal combustion engines or fuel cells, only nitrogen oxides (NO_x) are emitted at trace levels to the atmosphere (i.e., no CO_2 emission) [7]. Moreover, since hydrogen is an energy carrier not an energy source, it can be produced locally from renewable energy based technologies such as solar thermochemical hydrogen production [8], photocatalytic water splitting [9] and biomass based hydrogen production [10]. However, as of now, 98% of hydrogen is produced by fossil fuel reforming [11], mainly from methane [12].

Hydrogen economy consists of three parts as shown in Figure 1.1 [13]. As mentioned previously, hydrogen production is mostly based on methane reformation

[1] Some parts of the work presented in this chapter have been previously published in the following two articles. 1. DE Demirocak, MK Ram, SS Srinivasan, A Kumar, DY Goswami, EK Stefanakos, Spillover enhancement for hydrogen storage by Pt doped hypercrosslinked polystyrene, International Journal of Hydrogen Energy, 2012, 37(12), p. 12402-10. 2. DE Demirocak, SS Srinivasan, MK Ram, DY Goswami, EK Stefanakos, Volumetric Hydrogen Sorption Measurements − Uncertainty Error Analysis and the Importance of Thermal Equilibration Time, International Journal of Hydrogen Energy, 2012, 38(3), p. 1469–77). See Appendix C for copyright information.

which is the most efficient (83%) and cost effective (0.75 $/kg of hydrogen) option today [14]. Hydrogen must be produced from renewable energy based sources to make a significant impact on global warming mitigation. However, renewable energy based production methods (i.e., photocatalytic water splitting has a 10-14% efficiency and costs 4.98 $/kg of hydrogen) are not yet competitive with methane reforming [14].

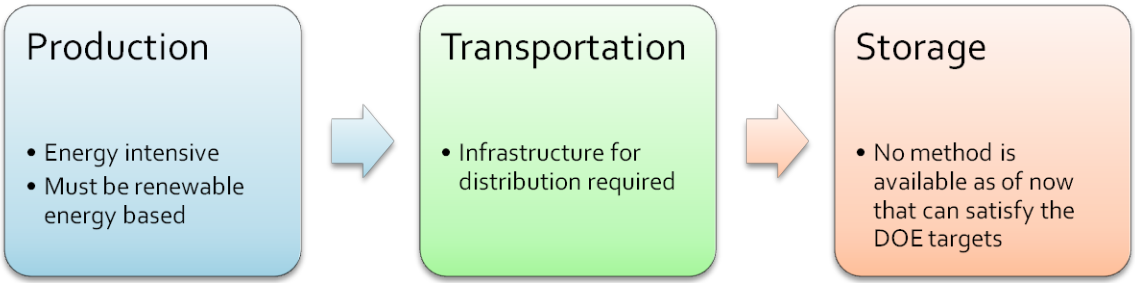

Figure 1.1. Hydrogen economy

Transportation of hydrogen requires a new distribution network and closely related to the prospective hydrogen storage technology. Hydrogen can be transported by pipelines, tube trailers and cylinders in gaseous form as well as by cryogenic tanks in liquid form [15]. The hydrogen distribution cost is estimated to be 15 times more expensive than liquid hydrocarbon fuels [16]. From the foregoing discussion, it is clear that the hydrogen economy suffers from high costs associated with the production and transportation steps; however, the main obstacle in realizing a hydrogen economy is the hydrogen storage step. As of now, there is no hydrogen storage technology that can satisfy the US Department of Energy (DOE) targets [17]. Hydrogen storage is discussed in more detail in section 1.2.

On the other hand, the hydrogen economy is also criticized due to significant energy losses involved in each step presented in Figure 1.1 [18,19]. In other words, considering a hydrogen fuel cell car, hydrogen needs to be produced using electricity

generated from renewable energy sources, then hydrogen needs to be delivered to the end users, and finally hydrogen is converted back to electricity by a fuel cell; therefore, the overall efficiency of the hydrogen economy is considerably lower than the electric economy [18,20]. Biofuels and electricity (i.e., battery storage) are the main alternatives to hydrogen [21-23].

1.2. Hydrogen Storage

As the worldwide energy generation portfolio involves more renewable energy based technologies, there will be a more urgent need for efficient and cost effective energy storage technologies for both mobile and stationary applications. Among many others, hydrogen was proposed to be a viable energy storage medium for mobile applications with zero greenhouse emission when utilized in an internal combustion engine or a fuel cell. However, hydrogen storage continues to be the bottleneck for the widespread utilization of hydrogen in mobile applications [24]. The DOE set targets for hydrogen storage systems for light-duty vehicles in collaboration with the automotive industry partners [17]. As of now, there is no material or hydrogen storage technology available that can satisfy all the DOE targets regardless of cost.

1.3. Hydrogen Storage Technologies

Hydrogen storage technologies can be broadly classified into four categories: (1) gaseous hydrogen storage, (2) liquefied hydrogen storage, (3) solid state hydrogen storage materials and (4) chemical hydrogen storage materials as presented in Figure 1.2. Both solid state and chemical storage materials are chemical methods of storing hydrogen contrary to physical methods of storage by compression and liquefaction. The primary

distinction between the solid state (i.e., reversible hydrides and porous materials[2]) and chemical hydrogen storage materials (i.e., ammonia-borane, methanol, liquid organics) is: solid state materials can be regenerated on-board, whereas chemical storage materials need to be regenerated off-board in centralized facilities [25]. Chemical storage materials have high energy densities [17]; however, spent fuel needs to be regenerated off-board in centralized facilities. On the other hand, on-board regenerable materials are visualized as the key element for the market penetration of fuel cell vehicles [23].

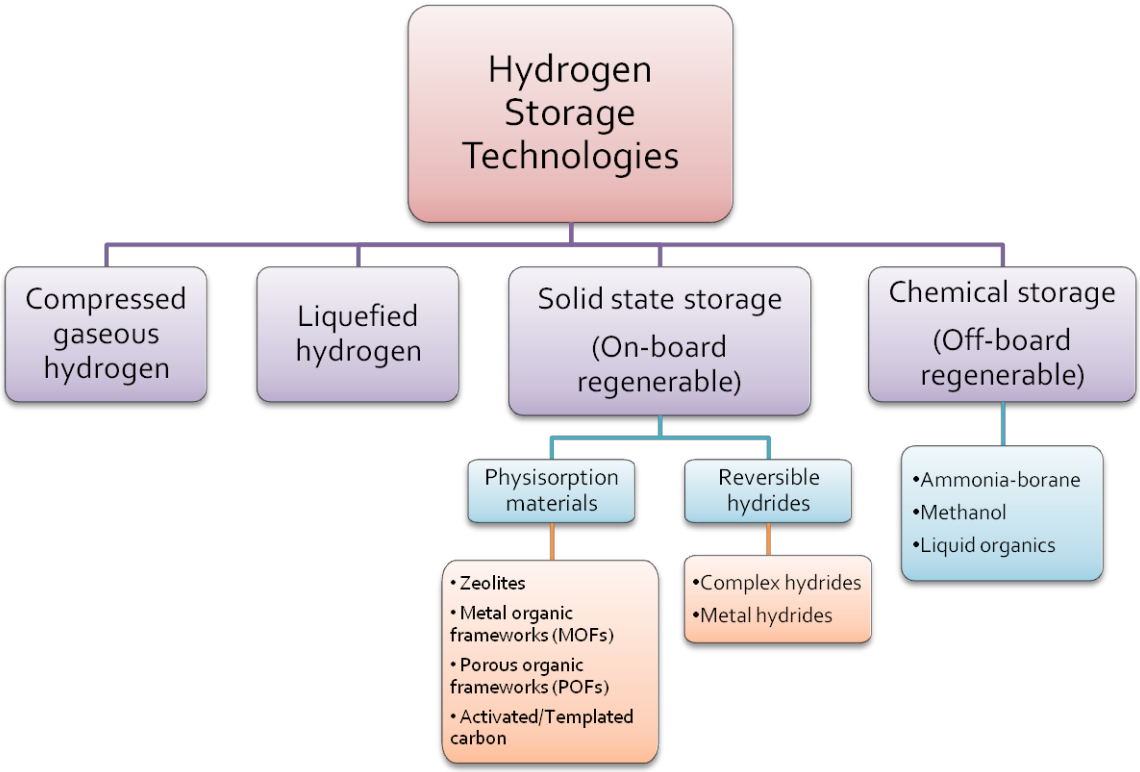

Figure 1.2. Classification of hydrogen storage technologies

Among the hydrogen storage technologies given in Figure 1.2, gaseous and liquefied hydrogen storage technologies are the most mature as of now, and utilized in various mobile applications [26]. However, significant energy losses during compression

[2] Porous materials and physisorption materials are used interchangeably throughout the text.

or liquefaction [27], safety concerns and low gravimetric capacity (i.e., especially for gaseous storage) [28] prevented the widespread market penetration of the gaseous and liquefied hydrogen storage technologies. Automotive industry considers the gaseous storage as being the most practical option as of now despite its shortcomings [29]. Therefore, shortcomings of the gaseous and liquefied hydrogen storage technologies led to intense research efforts on solid state and chemical storage technologies during the last decade [25,30-33]. This dissertation is focused on solid state storage materials which are discussed in more detail in section 1.3.2.

1.3.1. DOE Targets for Hydrogen Storage Systems for Light Duty Vehicles

A summary of the DOE targets for hydrogen storage systems for light duty vehicles is given in Table 1.1 [34]. The most stringent DOE targets are the gravimetric density and the volumetric density. In addition, operational cycle life (i.e., reversibility), system fill time (i.e., fast kinetics) and fuel purity are problematic for complex hydrides as discussed in more detail in section 1.3.2.1.2. The DOE targets presented in Table 1.1 are for the system level hydrogen storage system; therefore, in addition to storage materials' weight, the balance of the plant elements such as storage tank, valves, tubing, control system etc. also need to be accounted for. As a rule of thumb, the material's gravimetric storage capacity should be at least two times the system level targets to achieve the DOE system level targets [35].

1.3.2. Solid State Hydrogen Storage Technologies (On-board Regenerable Materials)

During the last decade, the research on hydrogen storage materials that can be regenerated on-board mostly concentrated on complex hydrides [36] and porous materials [33,37] which comprise a significant portion of the solid state hydrogen storage materials.

Table 1.1. DOE hydrogen storage targets for on-board hydrogen storage systems for light duty vehicles [34].

Storage parameter	Units	2010	2017	Ultimate
System gravimetric capacity	kg H_2 / kg system	0.045	0.055	0.075
System volumetric capacity	kg H_2 / L system	0.028	0.040	0.070
Operating ambient temperature	°C	-30/50 (sun)	-40/60 (sun)	-40/60 (sun)
Min/max delivery temperature	°C	-40/85	-40/85	-40/85
Operational cycle life	cycles	1000	1500	1500
Well to power plant efficiency	%	60	60	60
System fill time (5 kg H_2)	min	4.2	3.3	2.5
Fuel purity	% H_2	99.7 % (dry basis)		
Loss of useable H_2	(g/h) / kg H_2 stored	0.1	0.05	0.05

The complex hydrides have relatively high hydrogen storage capacity (i.e., high gravimetric and volumetric density); however, they suffer from high operating temperatures, sluggish kinetics and reversibility [38]. On the other hand, physisorption based porous materials have fast kinetics and complete reversibility; however, they can only store significant amount of hydrogen at cryogenic temperatures (i.e., 77 K) due to the weak interaction of hydrogen with the porous material matrix (i.e., low adsorption enthalpy) at or near room temperature (i.e., 298 K) [25]. Therefore, among the DOE targets, gravimetric density, operating temperature and charging/discharging times are the most stringent goals to achieve.

1.3.2.1. Reversible Hydrides

1.3.2.1.1. Metal Hydrides

Metal hydrides, AB_5–type alloys (i.e., $LaNi_5$) and AB_2–type alloys (i.e., $ZrMn_2$), are relatively old classes of reversible hydrides that date back to 1960s [39]. Extensively

studied metal hydrides are presented in Table 1.2. Metal hydrides form by dissociation of the hydrogen molecule on the metal surface, and the subsequent migration of the hydrogen atoms to the crystal lattice [40]. AB_5 and AB_2 type metal hydrides are also called intermetallic hydrides since hydrogen atoms are located at the interstitial crystal lattice sites of the metal hydride. Major drawbacks of the metal hydrides are their low gravimetric density (i.e., $LaNi_5H_6$), high operating temperature (i.e., MgH_2) and high cost of rare earth metals (i.e., La and Ti). Since AB_5 and AB_2 type metal hydrides usually have low gravimetric densities (1-2 wt.%), they are not suitable for mobile applications; however, due to their good reversibility and favorable operating conditions, they can be useful in stationary applications [40]. Among the metal hydrides, MgH_2 attracted significant attention due to its high gravimetric capacity (7.6 wt.%). The chemical bond in MgH_2 shows both ionic and covalent character; therefore, MgH_2 has a quite high operating temperature [41,42]. The studies on MgH_2 concentrated on lowering the desorption temperature and enhancing the kinetics by destabilization via different metal oxides and transition metals (i.e., Nb_2O_5, V_2O_5, Ti, Fe) [43,44].

Table 1.2. Extensively studied metal hydrides [45].

Metals	**Hydrides**	**Capacity (wt.%)**	**Temperature for 1 bar H_2 (°C)**
$LaNi_5$	$LaNi_5H_6$	1.37	12
FeTi	$FeTiH_2$	1.89	-8
Mg_2Ni	Mg_2NiH_4	3.59	255
$ZrMn_2$	$ZrMn_2H_2$	1.77	440
Mg	MgH_2	7.60	279

1.3.2.1.2. Complex Hydrides

The complex hydrides were brought to the attention of the hydrogen storage community by the prominent work of Bogdanovic et al. on Ti doped $NaAlH_4$ [46]. They

showed that by adding a small amount of Ti (i.e., 2 mol %), the $NaAlH_4$ complex hydride system can be regenerated reversibly by applying hydrogen pressure. Elemental hydride MgH_2 has a theoretical storage capacity of 7.6 wt. % and a desorption temperature around 300 °C as shown in Table 1.2. Attaining a higher gravimetric storage capacity is only possible by incorporating metals lighter than Mg, such as Li and Na. Therefore, research efforts concentrated on light metal complex hydrides during the last decade. The bonding in complex hydrides shows both ionic and covalent character. For instance, in $LiNH_2$, the N–H bond in the $(NH_2)^-$ anion shows mainly covalent character [47], whereas the Li–N bond shows a mixed ionic and covalent character [48]. Complex hydrides have high theoretical gravimetric densities; $NaAlH_4$ (7.5wt. %) [46], $LiAlH_4$ (10.6 wt. %) [49,50], $LiBH_4$ (18.4 wt. %) [51], Li_3N (11.5 wt. %) [52]. However, their reversible gravimetric capacities are around 4-5 wt. % under practical operating temperatures and pressures [36]. The reversible capacities of the most studied complex hydride systems are; $LiAlH_4$ (3-5 wt.%, 150-200°C) [49,50], $NaAlH_4$ (3-5 wt.%, 120-150°C) [50], $LiNH_2$-MgH_2/LiH (4-6 wt.%, 200-250°C) [53,54] and $LiBH_4$-$LiNH_2$-MgH_2 (4-8 wt.%, 200-280°C) [55,56]. Studies on complex hydrides mainly have focused on destabilization, and overcoming the reversibility, sluggish kinetics and toxic/poisonous gas emission issues [36,57-60].

1.3.2.2. Porous Materials

Porous materials (also called nanoporous, microporous, mesoporous, macroporous materials depending on the pore dimensions as well as high surface area and physisorption based materials in the literature [33,61-66]), include a wide range of organic and inorganic materials [67-71] with ordered (i.e., zeolites) and amorphous (i.e., activated carbon) structures. Porous materials have a wide range of applications in

purification [72,73], ion exchange [69], separation [74], catalysis [75], gas storage [33], drug delivery [76-78] and biomaterials [79]. Porous materials can be classified according to their pore dimensions. According to the International Union of Pure and Applied Chemistry (IUPAC), pores are divided into three categories based on their diameters; micropores (< 2 nm), mesopores (2 – 50 nm) and macropores (> 50 nm) [80]. Development of novel high surface area porous materials (i.e., metal organic frameworks (MOFs) [81-83], covalent organic frameworks (COFs) [84], templated carbons [62], porous aromatic frameworks (PAFs) [85], hypercrosslinked polymers [86-88], polymers of intrinsic porosity (PIMs) [89,90] and conjugated microporous polymers (CMPs) [91]) in the last decade resulted in extensive research efforts on gas storage applications of these materials [33]. Within the hydrogen storage context, porous materials extensively studied due to their fast sorption kinetics, reversibility and promising gravimetric capacity. Storage of hydrogen in the high surface area porous materials is realized by the interaction of hydrogen with the porous material surface via physisorption (i.e., adsorption) which is based on weak van der Waals forces [92]. Due to weak intermolecular forces (i.e., <6 kJ/mol [93]) involved in the physisorption of hydrogen to porous materials' surface, porous materials can only achieve significant hydrogen uptake at cryogenic temperatures (i.e., 77 K), with their hydrogen uptake at room temperature being usually less than 1wt. % at moderate pressures (i.e., 100 atm) [32,94,95]. The most important parameters that determine the porous materials' hydrogen storage capacity are surface area, pore volume, pore size and adsorption enthalpy [96,97]. The adsorption enthalpy of porous materials is low (<6 kJ/mol) [93], and needs to be improved (20-40 kJ/mol) [98] for significant hydrogen uptake at room temperature. The tuning of the

adsorption enthalpy and/or improving hydrogen uptake at room temperature can be realized via multiple modification methods, such as optimizing pore size [96], enhancing specific surface area (SSA), and doping with impurity atoms (B, N, alkali/transition metals) [99-103]. Therefore, studies concentrated on enhancing the adsorption enthalpy (i.e., creating open metal sites in MOFs [104]), maximizing the surface area [105] and fine tuning the pore size dimensions of the porous materials [106,107].

1.4. Scope and the Significance of the Dissertation

From the foregoing discussion, it is clear that developing a hydrogen storage material that can store sufficient hydrogen to satisfy the DOE targets and can operate reversibly near room temperature is of utmost importance. Therefore, this dissertation work is concentrated on developing a solid state material with a considerable hydrogen storage capacity near room temperature. To achieve this goal, spillover enhancement [108] in hypercrosslinked polystyrene and destabilization [27,54] of the Li-Mg-N-H complex hydride system are investigated. Hypercrosslinked polystyrene and Li-Mg-N-H complex hydride, both of which are solid state materials, belong to physisorption materials and reversible hydrides, respectively (see Figure 1.2 for reference). The advantages and disadvantages of the porous materials and complex hydrides are discussed in the following paragraph.

Porous materials have fast kinetics, complete reversibility and high gravimetric density only at cryogenic temperatures[3]; however, they have low gravimetric capacity (i.e., 1 wt. % <) near room temperature and high pressures (i.e., 100 atm). On the other

[3] Cooling hydrogen to cryogenic temperatures causes significant energy losses [109]; hence, not favorable to be used in mobile applications.

hand, complex hydrides have high volumetric density and relatively[4] high gravimetric capacity; however, they suffer from sluggish kinetics, irreversibility and toxic/poisonous gas emissions. To further elaborate, the main problem of solid state hydrogen storage materials is the insufficient gravimetric capacity of these materials near room temperature. A hydrogen storage system which operates at cryogenic temperatures (i.e., 77 K for a typical porous material [110,111]) or at high temperatures (> 150°C for a typical complex hydride [112,113]) is not favorable due to significant energy penalties involved in cooling and heating processes [114]. In other words, additional cooling and heating losses will cause significant reduction in the well to wheel efficiency of the hydrogen fueled car.

Another important part of this dissertation work is to develop guidelines for accurate volumetric hydrogen storage measurements via uncertainty analysis. Accurate hydrogen storage measurements are of paramount importance since the progress in the field relies on the accuracy of the reported values in the literature. In other words, go/no-go decisions, the effects of synthetic manipulations on the previously reported materials and the comparative studies on the existing materials heavily rely on the accuracy of the hydrogen storage measurements.

To sum up, this dissertation work includes three interrelated areas as follows;

- Spillover enhancement for hydrogen storage by Pt doped hypercrosslinked polystyrene (see section 1.4.1 for more details).

[4] Gravimetric density of complex hydrides is around 4-6 wt .% at or above 150°C [36] which is still relatively higher than the DOE targets.

- Reversible hydrogen storage in the Li-Mg-N-H system – The effects of Ru doped single walled carbon nanotubes (SWCNTs) on NH_3 emission and kinetics (see section 1.4.2 for more details).
- Volumetric hydrogen sorption measurements – Uncertainty error analysis and the importance of thermal equilibration time (see section 1.4.3 for more details).

1.4.1. Spillover Enhancement in Hypercrosslinked Polystyrene

Hydrogen storage enhancement of porous materials by the spillover mechanism was claimed to be one of the promising methods to achieve significant hydrogen storage capacity (4-5 wt. %) at room temperature (298 K) and high pressure (10 MPa) [108]. The schematic of the spillover phenomenon is given in Figure 1.3.

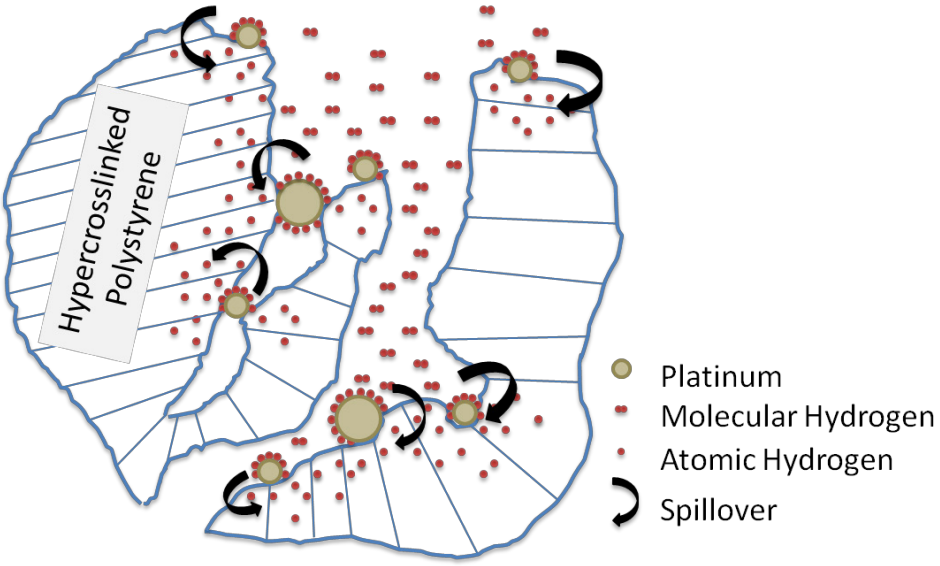

Figure 1.3. Spillover phenomenon.

Briefly, spillover is the dissociation of the hydrogen molecules into atoms by transition metals and subsequent diffusion of these atoms to the host material, in which hydrogen atoms can hydrogenate the unsaturated C-C bonds (i.e., activated carbon, graphite and SWCNTs) [115] or the benzene ring (i.e., MOFs, COFs and polymers) [116].

However, spillover enhancement for hydrogen storage is a highly disputable topic due to lack of understanding of the exact mechanism [117], and the contrary results reported for the same materials prepared at different laboratories [118,119]. In addition, spillover enhancement studies on porous polymers are scarce [120]. Therefore, the spillover enhancement in Pt doped hypercrosslinked polystyrene (i.e., porous polymer) is investigated to shed light on the effectiveness of the spillover enhancement in porous polymeric materials, and to understand if it is a viable option for room temperature hydrogen storage. Moreover, since the hypercrosslinked polystyrene mostly consists of benzene rings, this study also would make it possible to compare the spillover enhancement in other porous materials such as MOFs and COFs, where the main building block is the benzene ring, with the hypercrosslinked polystyrene.

1.4.2. Effects of Ru Doped SWCNTs on Kinetics and NH_3 Emission in the Li-Mg-N-H System

The $LiNH_2$–MgH_2 (i.e., Li-Mg-N-H) system is a promising complex hydride which has a 4.5 wt. % gravimetric capacity with a plateau pressure of 30 bar at 200 °C [53]. The main drawbacks of the $LiNH_2$–MgH_2 system are sluggish kinetics, high operating temperature and ammonia emission during hydrogen desorption [121]. Ammonia release is known to be detrimental to proton exchange membrane (PEM) fuel cells even at trace levels [122], and also causes loss of gravimetric capacity over a number of cycles [123]. The mechanistic investigations on the $LiNH_2$–MgH_2 system revealed that Li ion diffusion plays an important role in the reaction mechanism. On the other hand, Ru is known to be an active catalyst for ammonia decomposition [124], and Li ion diffusion is barrierless in SWCNTs [125]. Therefore, SWCNTs supported Ru catalyst can both enhance the kinetics and limit the ammonia emission in the $LiNH_2$–

MgH_2 system. The schematic of the proposed study is given in Figure 1.4. Therefore, the effects of Ru doped SWCNTs and pristine SWCNTs mixed $LiNH_2$–MgH_2 system are investigated to reveal their effects on the kinetics and ammonia suppression. Moreover, the relation of the kinetics and ammonia emission with the ball milling parameters is also studied to determine the optimal ball milling conditions.

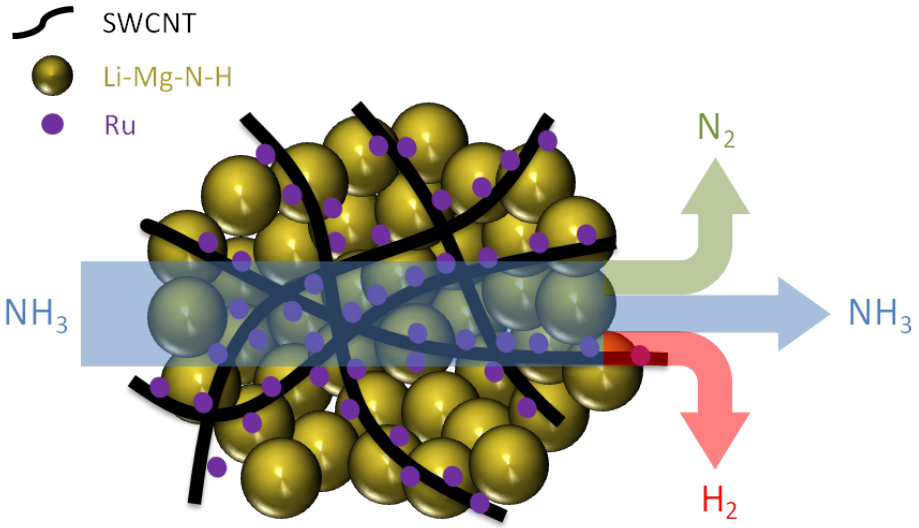

Figure 1.4. Schematic of ammonia decomposition by Ru doped SWCNTs in the Li-Mg-N-H complex hydride system.

1.4.3. Development of Guidelines for Accurate Hydrogen Storage Measurements

Accuracy of the hydrogen storage measurements is of major concern in the hydrogen storage community which impedes the down selection process of candidate materials and sets back progress in the field. Hydrogen storage measurements are prone to various sources of error [126], and especially problematic for the physisorption materials since their capacity is usually less than 1 wt. % at room temperature and high pressure. The Round-Robin study conducted by 14 different laboratories around the world clearly demonstrated the significance of accurate hydrogen storage measurements; in addition, results also experimentally showed that the standards deviation of the

adsorption isotherms increases with pressure increase due to propagation of the errors [127]. The majority of the hydrogen storage measurements reported in the literature makes use of the volumetric (Sievert's) type apparatus. Therefore, the volumetric apparatus is investigated by an uncertainty analysis to determine the uncertainties in the high pressure hydrogen sorption measurements. Based on the uncertainty analysis, practical guidelines are presented on the selection of the reservoir and sample cell volumes and sample mass loading as a function of the sample's intrinsic storage capacity for high accuracy measurements.

The volumetric gas sorption apparatus uses the real gas equation of state for calculating the hydrogen sorption of the sample (see chapter 5 for details). Therefore, any change in the temperature of the hydrogen gas admitted to the reservoir volume after the start of the measurement will result in pseudo absorption; hence, errors. Therefore, thermal equilibration time, which is an important parameter to be considered when the instrument enclosure and the hydrogen gas admitted to the reservoir volume are at different temperatures, is analyzed computationally by using COMSOL to eliminate pseudo sorption.

1.5. Dissertation Outline

Chapter 3 discusses the spillover enhancement for hydrogen storage in the Pt doped hypercrosslinked polystyrene and compares the effectiveness of the wet impregnation and bridge building sample preparation methods on spillover enhancement for hydrogen storage. Chapter 4 discusses the ammonia suppression by Ru doped SWCNTs in the Li-Mg-N-H reversible complex hydride system. Chapter 5 gives the design stage uncertainty analysis of the volumetric hydrogen storage measurements and

discusses the important error sources in hydrogen storage measurements. Finally, chapter 6 summarizes the most important outcomes from this study and gives recommendations for future work.

Chapter 2. Experimental Tools and Methods

This chapter gives the overview of the experimental tools and methods utilized in the dissertation work. Step by step synthesis and preparation procedures of the samples and the starting materials used can be found in the experimental sections of chapters 3 (i.e., section 3.2) and 4 (i.e., section 4.2).

2.1. Synthesis and Material Handling

2.1.1. Ball Milling

Use of ball milling (also known as mechanical milling [128,129]) for the preparation of metal hydrides dates back to 1968 [130]. The ball milling of complex hydrides is a mechanochemical synthesis due to chemical reactions taking place during mechanical milling [128]. The ball milling of complex hydrides reduces the onset temperature of desorption, enhances the kinetics and lower the activation energy due to creation of nano crystallites, smaller particle sizes and increased surface area [39,131,132]. Regarding the Li-Mg-N-H complex hydride system (see chapter 4 for more details), ball milling is especially important in preventing the release of NH_3 by enhancing the complete mixing of metal-amide ($LiNH_2$) and metal-hydride (MgH_2). Various groups showed that increasing the ball milling time decreases the grain size monotonically and increases the surface area up to some point (i.e., ≈ 5 hours ball milling) and also enhances the desorption kinetics considerably [131,133-135]. Moreover, ball milling is also very effective in dispersing a catalyst homogeneously in another

powder (see sections 3.2 and 4.2) and as an initial step in thorough mixing of solid state compounds for subsequent reactions (see section 3.2 for details).

The planetary ball mill, Fritsch Pulverisette 6, and an 80 ml stainless steel bowl with stainless steel balls (Ø 10 mm) are utilized for processing the solid state samples in this dissertation work as shown in Figure 2.1 [136].

Figure 2.1. (A) Fritsch Pulverisette P6 and (B) 80 ml stainless steel bowl, lid and Ø 10 mm stainless steel balls [136].

2.1.2. Glove Box

Complex hydride powders (see section 4.2 for more details) are air and moisture sensitive (i.e., forming oxides and hydroxides when exposed to air and moisture, respectively) as well as pyrophoric due to constituent elements such as Li and Mg. Therefore, complex hydrides should be handled, stored and processed in an inert atmosphere at all times. Since complex hydrides are solid state materials, conventional

methods of handling air/moisture sensitive materials via Schlenk line techniques are not suitable. Additionally, Pt doped hypercrosslinked polystyrene samples (see section 3.2 for more details) are also need to be handled and stored in an inert atmosphere to minimize the oxidation of the Pt particles. Moreover, most of the samples in this dissertation work were prepared over months; hence, to minimize the adverse effects of long term storage and to improve the comparability of the samples prepared at different times, all materials were stored in an inert atmosphere.

Figure 2.2. Innovative Technology System One glove box [137].

The glove box, Innovative Technology System One as shown in Figure 2.2 [137], filled with 99.999% pure (i.e., ultra high purity) argon is utilized to handle all air and moisture sensitive samples. Glove box operates at a slightly higher pressure as compared to the atmospheric pressure. Argon atmosphere inside the glove box is circulated through

the purification column continuously to remove oxygen and water impurities both of which were kept below 0.1 ppm.

2.2. Characterization

Structural (XRD, SEM and TEM), thermal (TGA), spectroscopic (FTIR, Raman and mass spectrometry) and gas sorption (volumetric) characterization tools are extensively utilized in this dissertation work as explained in more detail in the following sections.

2.2.1. Thermogravimetric Analysis (TGA)

TGA is an invaluable tool to assess the thermal stability of the samples under different atmospheres (for instance, nitrogen and air) [138]. Basically, for TGA experiments, small amount of sample is heated at a specific heating rate under gas flow of choice, and the change in weight is recorded.

Thermal stability of the samples in this work is investigated by a TA Instruments' SDT Q600, as shown in Figure 2.3, which is a simultaneous thermogravimetric analysis and differential scanning calorimetry tool. The SDT Q600 is equipped with a horizontal dual beam system with 0.1 μg sensitivity [139]. The SDT Q600 is calibrated for weight at regular intervals by using reference weights purchased from TA Instruments, and following a built-in procedure in TA Instruments' Advantage software. In addition, SDT Q600 is also utilized for quick screening of the hydrogen release characteristics of the complex hydride samples (see Figure 4.6). Since complex hydrides are air and moisture sensitive as mentioned previously, SDT Q600 is placed in a glove box during these experiments. Samples (around 10 mg) are loaded to a 90 μl alumina cups for TGA

experiments. More experimental details, such as heating rate, purge gas flow rate and purge gas type are given in the relevant sections throughout the dissertation.

Figure 2.3. TA Intruments SDT Q600, thermogravimetric analysis equipment [140].

2.2.2. X-Ray Diffraction (XRD)

Powder XRD is a powerful method to analyze the crystal structure of the materials. In 1913, William Lawrence Bragg and William Henry Bragg showed that crystal structures reflect incident X-rays in a specific pattern depending on their crystal lattice structures [141]. Bragg's law of diffraction can be expressed as,

$$n \cdot \lambda = 2 \cdot d \cdot \sin\theta \qquad (2.1)$$

where n is an integer, λ is the wavelength of the of X-rays, d is the spacing between the planes of atoms in the crystal lattice and θ is the angle (also known as Bragg angle) in between scattered and incident X-rays.

Each of the crystalline elements and compounds has a unique diffraction pattern (i.e., XRD spectrum). Therefore, it is possible to determine the constituent phases and elements of an unknown sample by comparing it with the known XRD database. International Centre for Diffraction Data (ICDD) is the leading organization for collecting, distributing, editing and publishing the XRD data [142].

Figure 2.4. Philip X'Pert Pro MD powder X-ray diffraction.

Philips X'Pert Pro MD, as shown in Figure 2.4, is employed to collect XRD spectrum of the samples. Since most of the samples prepared in this work are air and moisture sensitive, XRD data are collected with a custom built airtight sample holder [143] or using a zero diffraction sample holder. Samples are protected from air and

moisture by using a Kapton® or Mylar® film depending on the XRD peaks of interest. All samples are prepared in the glove box as mentioned previously. All the XRD data are analyzed with an X'Pert Highscore 1.0f software which includes 2001 release of the ICDD powder diffraction file.

XRD spectrum of a sample can also be utilized to determine the average crystallite size of a sample. The peak broadening in an XRD spectrum is an indication of a small crystallite size. Since ball milling, which creates smaller crystallite sizes, is employed in processing the complex hydrides in this work, peak broadening in the XRD spectrum is utilized to determine the average crystallite size of the complex hydrides subjected to different ball milling conditions (see chapter 5 for details). The relation between the peak broadening and crystallite size is formulated by Paul Scherrer in 1918 as given in Eq. 2.2 [144].

$$L=\frac{K\cdot\lambda}{B\cdot\cos\theta} \tag{2.2}$$

where L is the crystallite size, K is a numerical constant, θ is the Bragg angle and B is the peak broadening at FWHM (i.e., full width at half maximum).

The average crystallite size of the samples in this work are calculated with the built-in Scherrer calculator in the X'Pert Highscore 1.0f software after subtracting the instrumental peak broadening which is obtained from the XRD spectrum of a single crystal Si wafer.

2.2.3. Scanning Electron Microscopy (SEM)

Scanning electron microscope, Hitachi S-800 as shown in Figure 2.5, equipped with energy dispersive X-rays (EDX) attachment [145] is employed to determine the morphological changes in the samples upon ball milling and synthetic procedures, and to

determine the elemental composition of the samples (see sections 3.3.2 and 4.3.2 for more details).

All samples are loaded to the SEM on a double sided carbon tape. Samples exposed to air less than a minute during the transfer to the SEM. For elemental composition analysis by EDX, measurements are taken from multiple sites to obtain an average distribution of the elements.

Figure 2.5. Hitachi S-800 scanning electron microscope.

2.2.4. Transmission Electron Microscopy (TEM)

Transmission electron microscope [146], Tecnai F20 as shown in Figure 2.6, equipped with energy dispersive X-rays (EDX) attachment [145] is employed to determine the particle sizes of nanoparticles (i.e., Pt in hypercrosslinked polystyrene and Ru in SWCNTs as discussed in sections 3.3.2 and 4.3.2, respectively), structural characteristics of SWCNTs (i.e., bundling and defects created upon synthetic procedures

in SWCNTs, see section 4.3.2 for details) and to determine the elemental composition of the samples.

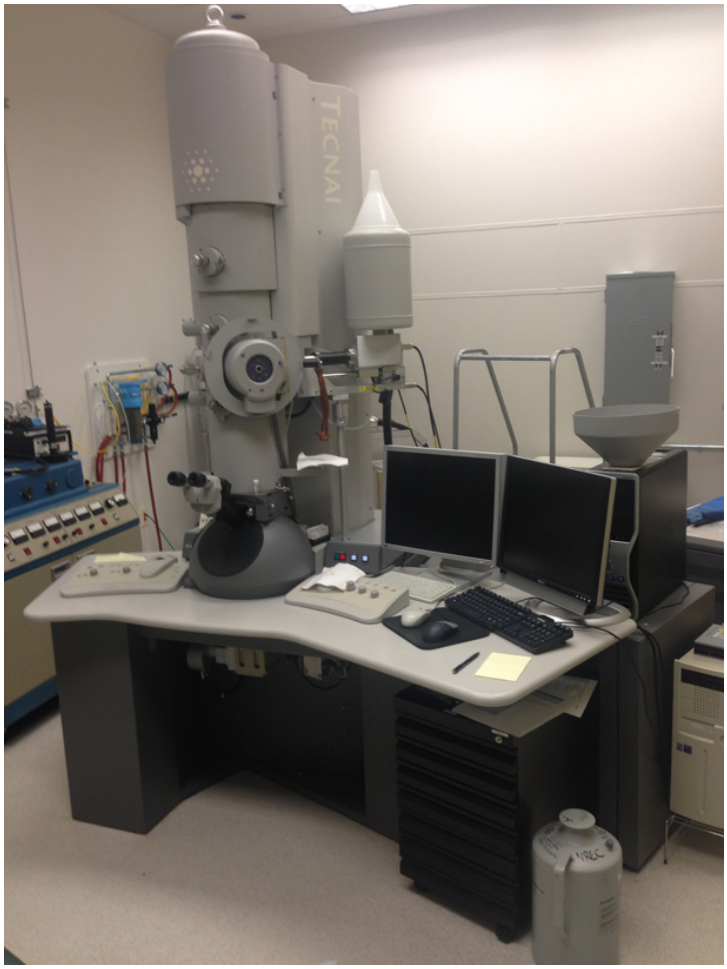

Figure 2.6. Tecnai F20 transmission electron microscope.

TEM samples are prepared as the following method: 1 mg of a sample is dispersed in a 5 ml of methanol, after sonicating the solution for 5 min, couple of drops of the solution, which is withdrawn by a Pasteur pipette, are dropped to a 300 size mesh copper grid. Finally, copper grid is first dried at room temperature overnight and then in an oven at 80 °C for couple of hours to ensure that all the solvent is evaporated before loading to the TEM. For particle size analysis, measurements are taken from multiple

sites to obtain an average size distribution of the nanoparticles. All measurements are conducted at 200 kV acceleration voltage.

2.2.5. Fourier Transform Infrared Spectroscopy (FTIR)

FTIR is an effective and facile method to determine the chemical structure (i.e., functional groups or type of chemical bonds) of the amorphous materials (i.e., polymers) [147]. Perkin Elmer Spectrum One, as shown in Figure 2.7, is utilized to characterize the hypercrosslinked polystyrene samples in this work (see section 3.3.2 for details).

Figure 2.7. Perkin Elmer Spectrum One FTIR.

Samples for FTIR analysis are prepared by the KBr pellet method. KBr is a crystalline material which is infrared transparent. Typically, 1 mg of a sample is thoroughly mixed with a 10 mg of a KBr powder in a mortar. After pelletizing the powder to create a couple of mm thick sample-KBr thin film, sample is placed in between

KBr windows and infrared spectrum is collected. All data are analyzed by a Perkin Elmer Spectrum software.

2.2.6. Raman Spectroscopy

Raman spectroscopy is utilized to determine the structural characteristics (i.e., defects) of the SWCNTs (see section 4.3.2 for details). As discussed by Dillon et al., the full width at half maximum (FWHM) value of D band indicates the presence of non-SWCNTs carbonaceous impurities; in addition, the intensity ratio of D band to G band (I_D/I_G) is related to the defects introduced into the SWCNTs [148].

Raman experiments are carried out using a confocal Raman microscope (Olympus, IX71 [149]) purchased from Horiba Jovin Yvon. For all experiments, an excitation wavelength at 647 nm from an argon and krypton laser (Coherent, Innova 70C series [150]) is used with a 5 mW of power, 10 s of exposure time and 3-5 accumulations. The spectrograph grating is 600 grooves/mm and the 20X objective is used throughout the experiments. Raman measurements are taken at various locations on the samples to account for the heterogeneity of the solid samples.

2.2.7. Mass Spectrometry (MS)

Mass spectrometry, MKS Cirrus as shown in Figure 2.8 [151], is utilized to qualitatively determine the species emitted (i.e., hydrogen and ammonia) from the Li-Mg-N-H complex hydride (see chapter 4 for details). The custom built step shown in Figure 2.8 consists of mass flow controllers, a tube type furnace and an MKS Cirrus quadrupole mass spectrometer. The transfer line in between the tube type furnace and the MKS Cirrus MS is heated slightly above 100 °C to prevent the condensation of the emitted species.

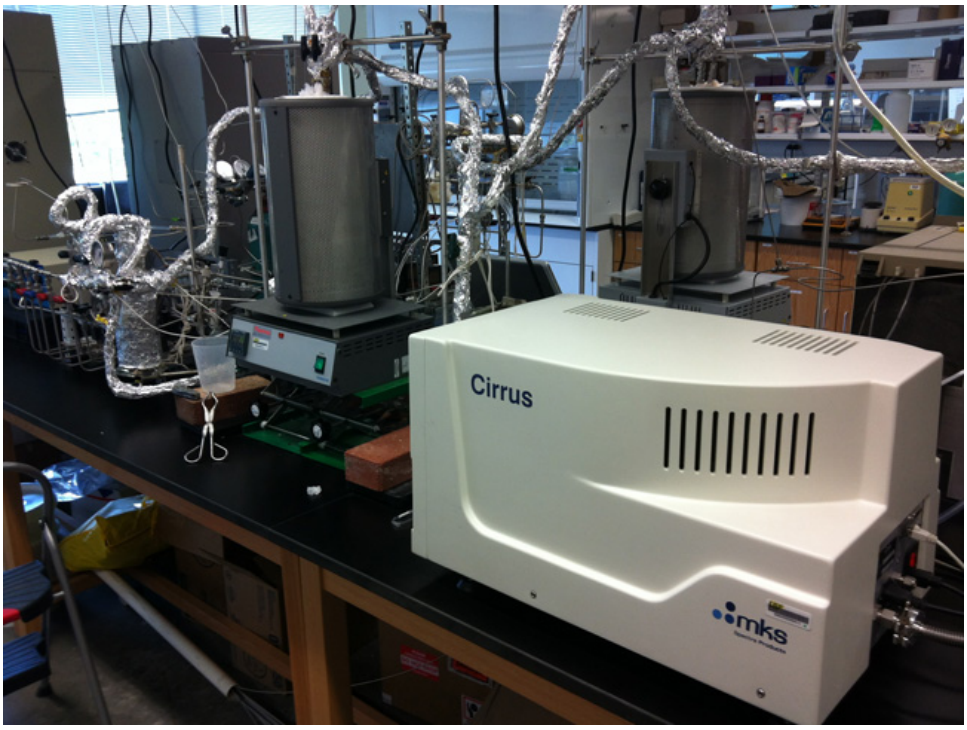

Figure 2.8. MKS Cirrus mass spectrometer in a custom built setup with tube type furnace and mass flow controllers.

Experimental procedure for mass spectrometry experiments is as follows: sample is loaded in a quartz U-tube and sandwiched in between glass wools to secure the sample during the experiments. As mentioned previously, since complex hydrides are air and moisture sensitive all the samples are prepared inside the glove box. The sample loaded to the U-tube is sealed with Parafilm® to prevent air and moisture exposure while transferring the sample to the MS. Sample is exposed to air for less than a minute while attaching the U-tube to the setup. Upon attaching the U-tube to the setup, sample is purged with helium (50 ml/min) at room temperature for at least 30 min or until the background signals of all the species are stabilized. Finally, the sample is heated up under helium flow (50 ml/min) at 5 K/min heating rate and the signals of the gas species (hydrogen m/z = 2, ammonia m/z = 17 and nitrogen m/z = 28) are recorded for further analysis.

2.2.8. Volumetric Gas Sorption

Volumetric gas sorption measurements are at the heart of this dissertation work. Volumetric gas sorption measurements are thoroughly discussed in chapter 5; hence, not repeated in here. Briefly, in a volumetric gas sorption apparatus, the gas uptake of a material is calculated by using an appropriate real gas equation of state from measurements of the pressure drop in a volume calibrated reservoir and sample cell, the temperature of the reservoir and sample cell volumes, and the density of the material which is usually determined by a helium expansion test.

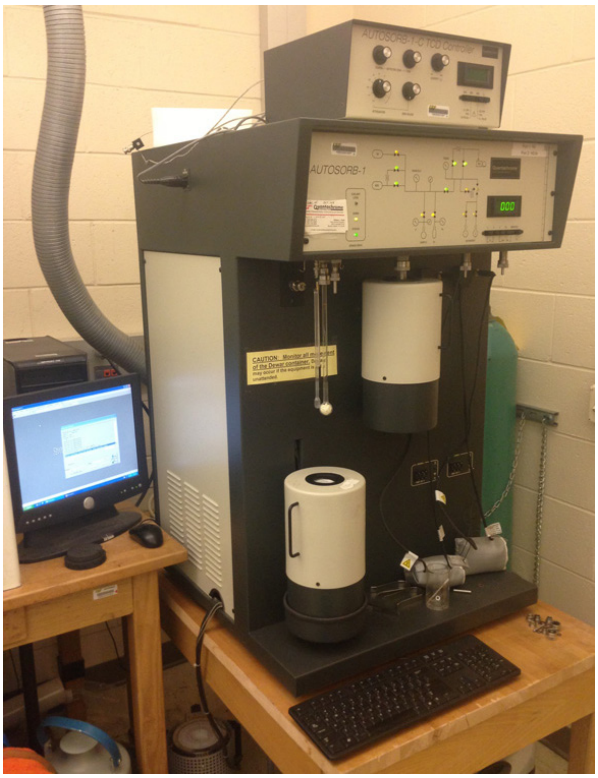

Figure 2.9. Quantachrome AS1C, low pressure volumetric gas sorption tool with chemisorption analysis capability [152]. Quantachrome AS1C is equipped with low pressure transducers (< 2 atm) to collect high accuracy data at the low pressure region.

Considering hypercrosslinked polystyrene, a porous material, hydrogen storage capacity at 77 K / 1 atm and at 298 K / 10 MPa are measured by the Quantachrome

AS1C, as shown in Figure 2.9, and Setaram-HyEnergy PCTPro 2000, as shown in Figure 2.10, respectively.

Figure 2.10. Setaram-HyEnergy PCTPro 2000, high pressure volumetric gas sorption tool [153]. PCTPro 2000 is equipped with a high pressure transducer (up to 200 bar) and a heating mantle for high temperature measurements (up to 400 °C).

The hydrogen adsorption enthalpy of the hypercrosslinked polystyrene is calculated by Clasius-Clapeyron equation [154-156] from the hydrogen adsorption isotherms at 77 K and 87 K. In addition, surface area and pore size distribution of the hypercrosslinked polystyrenes are calculated using the Brunauer-Emmet-Teller (BET) theory and non-local density functional theory (NLDFT) [154-156], respectively, from the nitrogen adsorption isotherms at 77 K using the Quantachrome AS1C. The sample loading for measurements of hydrogen and nitrogen adsorption isotherms at cryogenic

temperatures was around 100 mg. However, due to instrument limitations[5], in ultra low pressure (10^{-5} to 10^{-3} P/Po)[6] nitrogen adsorption measurements, which are required for pore size calculations, sample mass loading was around 10 - 20 mg. The equilibration time for collecting each isotherm point was set to 6 min. All the calculations (i.e., BET and NLDFT) were carried out using a Quantachrome AS1Win (ver. 1.55) software.

The hydrogen storage capacity of a material is usually reported by kinetics measurement and/or PCT (pressure-concentration-temperature) isotherm in the literature. Kinetics measurements, mostly reported for reversible hydrides to show the hydrogen sorption rate of a sample, are performed by charging a sample with hydrogen at a pressure higher than the initial pressure of the sample cell. On the other hand, PCT measurements are simply a collection of the kinetics measurements which are obtained by incrementally increasing the hydrogen pressure until the ultimate set pressure is reached. The difference in between kinetics and PCT measurements can be best explained by referring to Figure 2.11, which is a combination of the Figure 3.12 and Figure 3.13. As shown by the arrows in Figure 2.11, the hydrogen uptake of a sample (initially evacuated) and the pressure inside the sample cell at the end (90 min for Figure 2.11)[7] of the first step of the kinetics measurements form the first isotherm point in the PCT measurement. To obtain the second PCT isotherm data point, the pressure inside the

---

[5] Liquid nitrogen dewar in Quantachrome AS1C has an approximately 2L volume, and the nitrogen inside the dewar boils off in 2 days on average; therefore, data collection should be completed in 2 days. Since collecting adsorption data in the ultra low pressure region (10^{-5} to 10^{-3} P/Po) takes more time than the low pressure region (> 10^{-3} P/Po) and the samples studied are highly microporous, sample mass loading for the ulta low pressure measurements was around 10 - 20 mg to complete the measurements in 2 days time. According to Webb et al. [156], for good precision, sample loaded for testing should have 5 to 10 m^2/g surface area. Since all the samples studied have a high surface area (> 1000 m^2/g), even the sample mass loading of 10 mg satisfies the condition for good precision.

[6] Po represents the saturation pressure of the adsorbate (i.e., nitrogen)

[7] Kinetics data should be collected until the sample reaches its ultimate capacity (i.e., until the kinetics curve levels off) at that pressure.

sample cell is increased to a predefined set pressure (8 bar increments in Figure 2.11) and kinetics data measured, from the pressure and hydrogen uptake values at the end of the second step of the kinetics measurements, the second PCT isotherm data point is obtained. All the remaining PCT isotherm data points are measured the same way until the ultimate set pressure is reached.

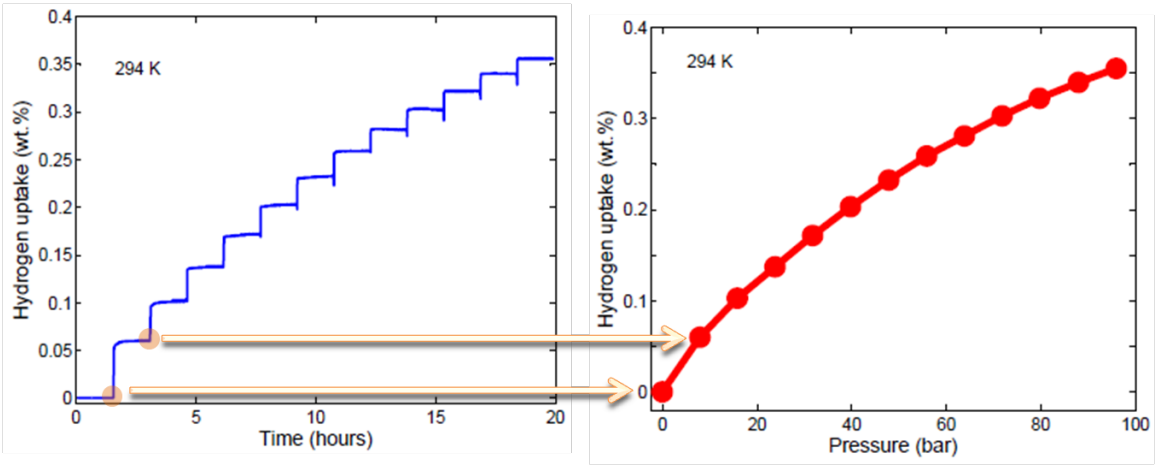

Figure 2.11. Contructing a PCT isotherm from a set of kinetics measurements. The left panel shows a set of kinetics measurements for MN270-bridged. The right panel shows the resulting PCT isotherm created from the kinetics measurements given in the left panel for MN270-bridged.

Chapter 3. Spillover Enhancement for Hydrogen Storage by Pt Doped Hypercrosslinked Polystyrene[8]

3.1. Introduction

Hydrogen storage continues to be the weakest link in the realization of a hydrogen economy despite the intense research efforts within the last decade [109,157]. Among the many goals set by the US Department of Energy (DOE), gravimetric/volumetric density and reversibility near ambient conditions are the most stringent ones [17,158]. Currently, the conventional storage methods of compressed and liquefied hydrogen are the only well-established options; however, their drawbacks have prevented their widespread application as a storage media for mobile applications [24,25]. Thus, ongoing efforts have concentrated on the novel high surface area porous materials that are based on physisorption (i.e., metal organic frameworks (MOFs) [81-83], covalent organic frameworks (COFs) [84], templated carbons [62], porous aromatic frameworks (PAFs) [85], hypercrosslinked polymers [86-88], polymers of intrinsic porosity (PIMs) [89,90], and conjugated microporous polymers (CMPs) [91]).

The high surface area porous materials have drawn a growing interest in the hydrogen storage challenge due to their fast sorption kinetics, reversibility and promising gravimetric capacity. High surface area porous materials can achieve significant

[8] The work presented in this chapter has been previously published (DE Demirocak, MK Ram, SS Srinivasan, A Kumar, DY Goswami, EK Stefanakos, Spillover enhancement for hydrogen storage by Pt doped hypercrosslinked polystyrene, International Journal of Hydrogen Energy, 2012, 37(12), p. 12402-10.). See Appendix C for copyright information.

hydrogen uptake by physisorption at 77 K; however, their uptake at room temperature (RT) is usually less than 1wt. % at moderate pressures (i.e., 100 atm) [32,94,95]. In addition, the adsorption enthalpy of these materials is low (<6 kJ/mol) [93], and needs to be improved (20-40 kJ/mol) [98] for significant hydrogen uptake at RT. The tuning of adsorption enthalpy and/or improving hydrogen uptake at RT can be realized via multiple modification methods, such as optimizing pore size [96], enhancing specific surface area (SSA) and doping with impurity atoms (B, N, alkali/transition metals) [99-103].

Incorporation of transition metals (i.e., Pt, Ru, Pd, Ni) can enhance the hydrogen binding via Kubas type interactions due to the empty d-orbitals [159], and/or by hydrogen spillover [160]. The hydrogen spillover phenomenon has been well-known in catalysis for over three decades and various literature reviews have been published [160-163]. On the other hand, its application to the hydrogen storage materials was just recently investigated [164]. The schematic of the spillover phenomenon is given in Figure 1.3. Briefly, spillover is the dissociation of the hydrogen molecules into atoms by transition metals and subsequent diffusion of these atoms to the host material, in which hydrogen atoms can hydrogenate the unsaturated C-C bonds (i.e., activated carbon, graphite, and single walled carbon nanotubes) [115,165] or the benzene ring (i.e., MOFs, COFs, and polymers) [116,166,167]. Among the various steps of spillover, dissociation of hydrogen molecules and diffusion of hydrogen atoms are considered as instantaneous and barrier-less, respectively; however, hydrogen atoms need to overcome high energy barriers for migration to the host material which makes migration the rate limiting step [165]. Therefore, minimum clustering and fine molecular level dispersion of transition metals within the host material is desirable to make the migration path as short as possible.

The spillover enhancement in high surface area porous materials has been reported by over 40 different groups [168,169] and the proof of spillover and/or C-H bond formation have been studied using X-ray photoelectron spectroscopy [115], inelastic neutron scattering [170-173], electrical conductivity measurements [174-176], infrared spectroscopy [176], and thermal desorption spectrometry [177]. However, the role of hydrogen spillover in hydrogen storage capacity enhancement is still disputable due to lack of understanding of the exact mechanism [117], and the contrary results on the hydrogen uptake characteristics [118,119,178-183].

The hydrogen spillover enhancement in carbon nanostructures [184-189], zeolites [190], MOFs, [102,191,192] and COFs [193] was extensively investigated both theoretically and experimentally. However, spillover studies in polymeric materials are rather scarce [194], and transition metal doping of polymers were studied mostly within the context of catalysis research [195-198]. Additionally, high pressure hydrogen uptake of transition metal doped polymers at RT has never been reported.

In this study, commercially available hypercrosslinked polystyrenes (HPS) were screened to determine the most suitable candidate (i.e., high SSA, narrow pores) to study the effects of Pt doping/hydrogen spillover on the hydrogen uptake enhancement at RT. This has been realized by utilizing two different synthetic methods, the wet impregnation and bridge building technique, to elucidate the effectiveness of these widely applied methods for the spillover enhancement on hydrogen storage.

3.2. Experimental Section

3.2.1. Materials

Hypercrosslinked polystyrenes MN170, MN200, and MN270 were kindly supplied by Purolite. Dowex Lewatit VP-OC-1064 MD PH, Dowex Optipore SD-2, Dowex Optipore L-493, reagent grade chloroplatinic acid hexahydrate, acetone and sucrose were purchased from Sigma Aldrich. Supported catalyst, 5 wt. % Pt/activated carbon, was purchased from Strem Chemicals.

3.2.2. Synthesis

As received MN270 beads had a 0.5-1 mm diameter on average. To facilitate the Pt dispersion within the polymer matrix and sample characterization, MN270 was ball milled with Fritsch Pulverisette 6 for 2 h at 200 revolutions per minute (RPM) before any modification.

A procedure similar to that reported in the literature [184] was followed for the Pt doping of MN270 by the wet impregnation method. Due to larger sample masses (≈ 1.5 g) used in the high pressure hydrogen measurements, the doping procedure was scaled-up to prepare MN270 with a 6 wt. % Pt loading. Typically, 2 g of MN270 was degassed in vacuum at least 12 h at 393 K. The dried sample was dispersed in 150 ml of acetone and stirred for 30 min. A 20 ml acetone solution containing 324 mg (6 wt. %) of $H_2PtCl_6 \cdot 6H_2O$ was added to the MN270 solution over 90 min using a syringe pump. After sonication (100W, 42kHz) for 1 h, the solution was then stirred for another 24 h. The sample was dried in an oven at 323 K overnight and then loaded into a tube type furnace in a quartz boat for activation. The sample was further dried in helium (300 ml/min) for 2 h at 473 K, then activated in hydrogen flow for 5 h at the same

temperature/flow rate and cooled to RT in hydrogen flow. Finally, the sample was passivated in helium for 5 h at RT and stored in an argon-filled glove-box until further analysis. The synthesized sample was named MN270-6wt%Pt.

For the bridge building treatment, a previously reported procedure was followed [192]. A 2 g of dry MN270 was mixed with 5 wt. % Pt/activated carbon (Pt/AC) and D-glucose with a weight ratio of 8:1:1 (MN270 : Pt/AC : D-glucose) and ball milled for 1 h at 200 RPM. This mixture was then loaded in a quartz boat and placed in a tube type furnace. The mixture was heated to 453 K at 5 K/min under 100 ml/min helium flow and kept at 453 K for 3 h and then temperature ramped at 5 K/min to 523 K and maintained for an additional 12 h to ensure carbonization. After cooling to RT in helium flow, the sample was stored in an argon filled glove box until further analysis. This sample was named MN270-bridged.

3.2.3. Characterization

Scanning electron microscopy (SEM), JEOL S800, with energy dispersive X-rays (EDX) and transmission electron microscopy (TEM), Tecnai F20, were utilized to investigate the surface morphology of the samples and the size/dispersion of the Pt particles. The powder X-ray diffraction of the samples was carried out by a Philips X'pert diffractometer with CuKα radiation of λ=1.54060 Å, and diffraction data was analyzed using a PANalytical X'pert Highscore software version 1.0f. The gravimetric weight loss was analyzed by a TA Instrument's SDT Q600. The samples were heated at a rate of 20 K/min under 100 ml/min nitrogen flow and the data was analyzed with a TA Universal Analysis 2000 software. The FTIR spectra were collected using a Perkin Elmer Spectrum One in transmission mode by using the KBr pellet method. The nitrogen and

low pressure (0-1 atm) hydrogen adsorption isotherms were measured by using a Quantachrome AS1C. The measurement accuracy and repeatability of the Quantachrome AS1C were verified with the Quantachrome standard reference material (SARM-2012) before any measurements. The test value was within the reproducibility limit (±5 %) of the expected value. The adsorption enthalpies of the commercial HPS were calculated from the hydrogen adsorption isotherms at 77 K and 87 K using the Clasius-Clapeyron equation in Quantachrome AS1Win software.

The high pressure (up to 100 atm) hydrogen pressure-concentration isotherms and kinetics data were collected with Setaram-HyEnergy PCTPro 2000, Sievert's type apparatus. Each isotherm point was measured at the end of 90 min due to slow diffusion of the spiltover hydrogen over receptor [177,199,200]. To minimize the experimental errors, at least 1.5 g of a sample was loaded for every measurement and the sample was outgassed *in situ* for at least 12 h at 423 K in dynamic vacuum (≈1.3 x 10^{-5} atm) [52]. In addition, a blank run (i.e., empty cell) isotherm was collected and subtracted from the sample isotherms [201].

3.3. Results and Discussion

3.3.1. Screening of the Commercial Hypercrosslinked Polystyrenes

The thermogravimetric analyses (TGA) of the commercial HPS are given in Figure 3.1 which shows that all materials are stable up to 300-350 °C. The initial weight loss at temperatures up to 100 °C is due to water adsorbed within the pores, in accordance with the material safety data sheet of the materials. The reduction temperature of MN270-6wt%Pt (473 K) is also selected based on the TGA analysis. To be on the safe side,

MN270-6wt%Pt is reduced at a temperature slightly lower than the MN270's decomposition temperature (see section 3.2.2 for details).

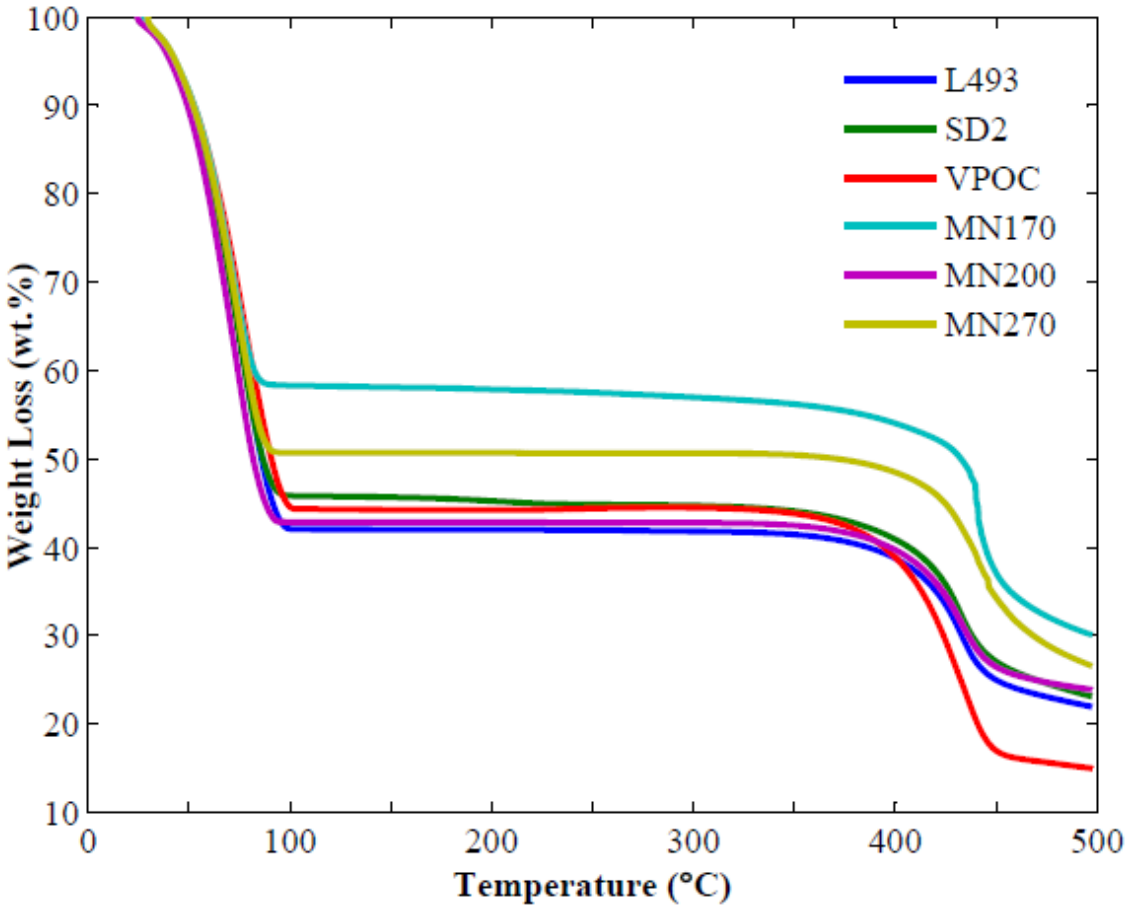

Figure 3.1. TGA of the commerical hypercrosslinked polystyrenes (HPS).

Surface area, pore size distribution and pore volume are among the most important parameters directly affecting the hydrogen uptake of any physisorption material. The morphological characteristics of the HPS studied in this work are summarized in Table 3.1. The pore size distribution was calculated by the non-local density functional theory (NLDFT) using a hybrid slit/cylindrical pore model (i.e., slit pore geometry for pores < 2nm and cylindrical pore geometry for pores > 2nm) since this hybrid model gave better fit to the experimental data than using either one alone.

Table 3.1. Morphological and hydrogen uptake characteristics of commercial HPS.

commercial name	surface area[a] (m^2/g)	avg. pore size[b] (Å)	V_{tot} [c] (cc/g)	V_{micro} [d] (cc/g)	H_2 Uptake[e] (wt%)
Optipore SD2	1337	11	1.3	0.58	1.18
Optipore L493	1124	19	0.81	0.57	1.25
Lewatit VPOC 1064	975	19	1.25	0.41	0.72
Purolite MN170	1153	13	1.09	0.55	1.02
Purolite MN200	1096	12	0.98	0.46	1.31
Purolite MN270	1451	10	1.09	0.63	1.53

[a] Calculated from N_2 adsorption at 77 K using the Branuer-Emmett-Teller (BET) equation in the 0.01 to 0.1 pressure range. [b] Indicating the most dominant pore size given in Figure 3.2. Calculated using NLDFT for N_2 adsorption on carbon with slit/cylindrical pores. [c] Total pore volume calculated using N_2 adsorption at P/P_o=0.99. [d] Total micropore volume calculated using N_2 adsorption at P/P_o=0.25. [e] Hydrogen uptake at 1 atm and 77 K.

The pore size distribution and hydrogen uptake at 77 K of each HPS are given in Figure 3.2 and Figure 3.3, respectively. As seen in Table 3.1, the hydrogen uptake and SSA of the commercial HPS are not directly proportional, contrary to other porous materials (i.e., carbons) [95], and are on par with the previously published results [87]. This relationship might be due to different functionalities within the polymer backbone since most of the HPS have very similar pore size.

The adsorption enthalpies (Q_{st}) of the commercial HPS are given in Figure 3.4. All the materials have Q_{st} lower than 7 kJ/mol which decreases as hydrogen uptake increases. The decrease rate of Q_{st} in MN200 and MN270 is smaller than in MN170, SD2, L493, and VPOC indicating the relatively homogeneous distribution of the adsorption sites in MN200 and MN270. The selection of the appropriate HPS for the RT spillover study was based on two criteria: favorable characteristics for (1) high pressure hydrogen uptake at RT, and (2) Pt doping.

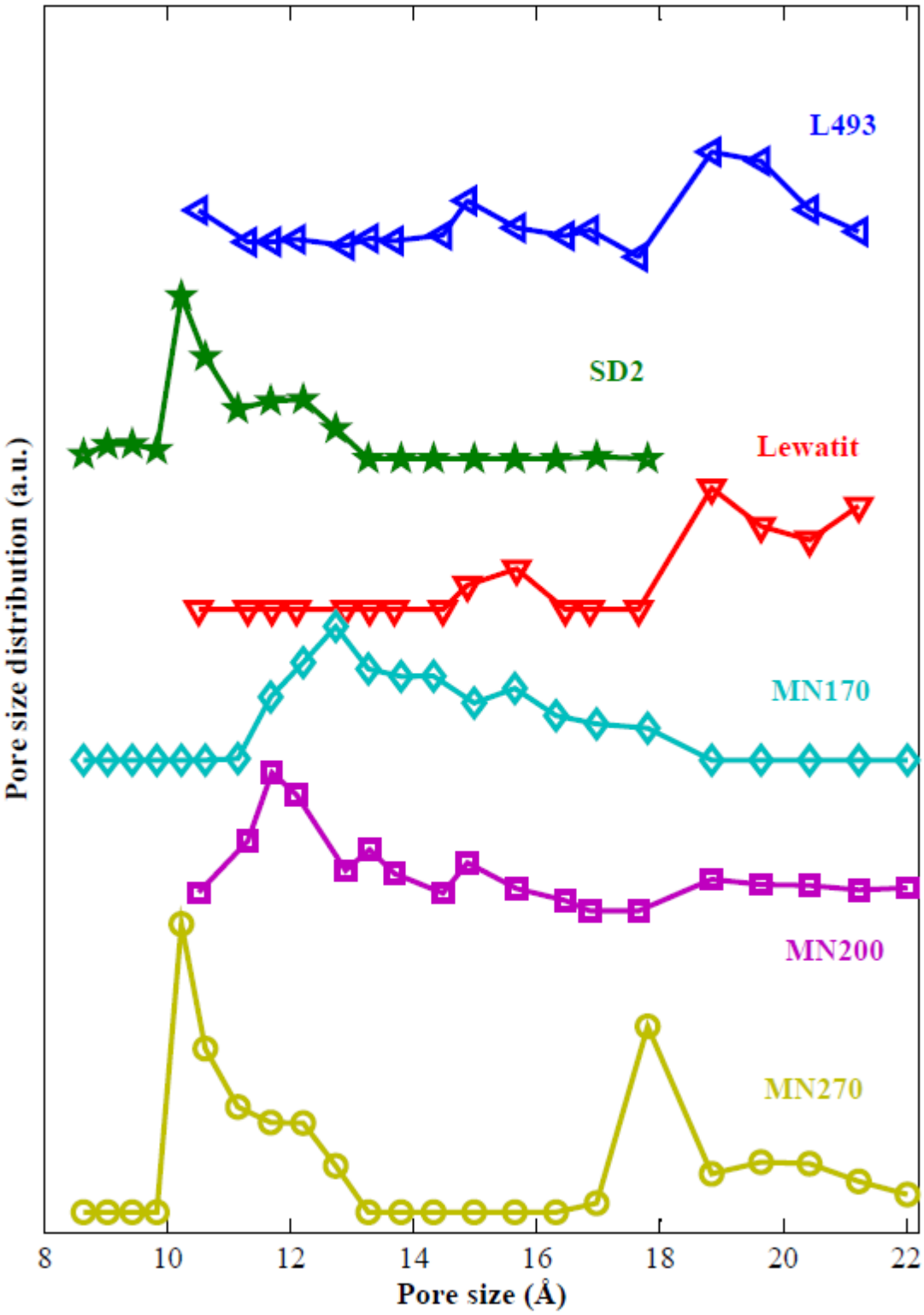

Figure 3.2. Pore size distribution of the commercial HPS.

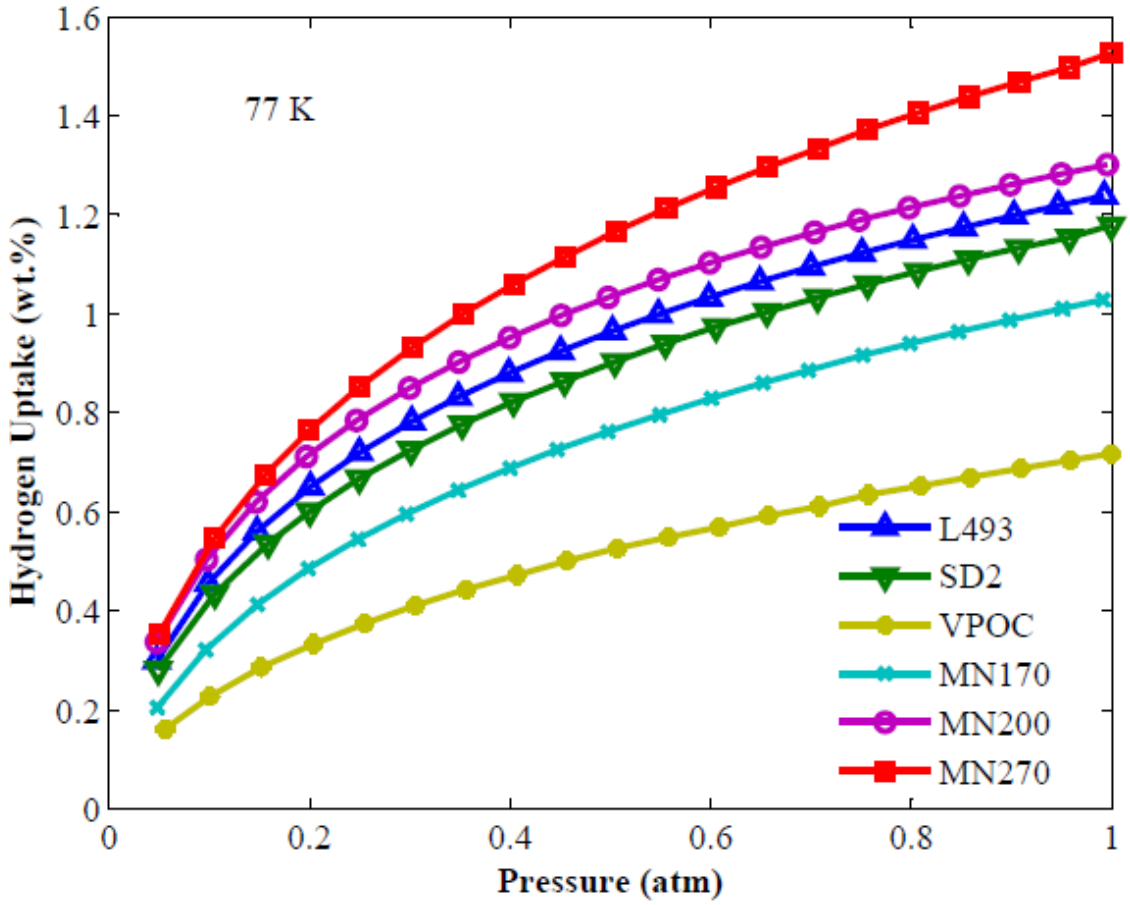

Figure 3.3. Hydrogen uptake of the commercial HPS at 77 K.

High surface area and pore volume are beneficial for high pressure hydrogen uptake; in addition, narrow pores are favorable for stronger adsorbate-adsorbent interaction [96,97]. On the other hand, narrow pores and high surface area can also help inhibiting the Pt particle size growth during the synthetic procedures (i.e., wet impregnation, high temperature hydrogen reduction and carbonization). Therefore, MN270 was selected for the RT spillover study considering its highest SSA, narrow pores and relatively high pore volume/adsorption enthalpy.

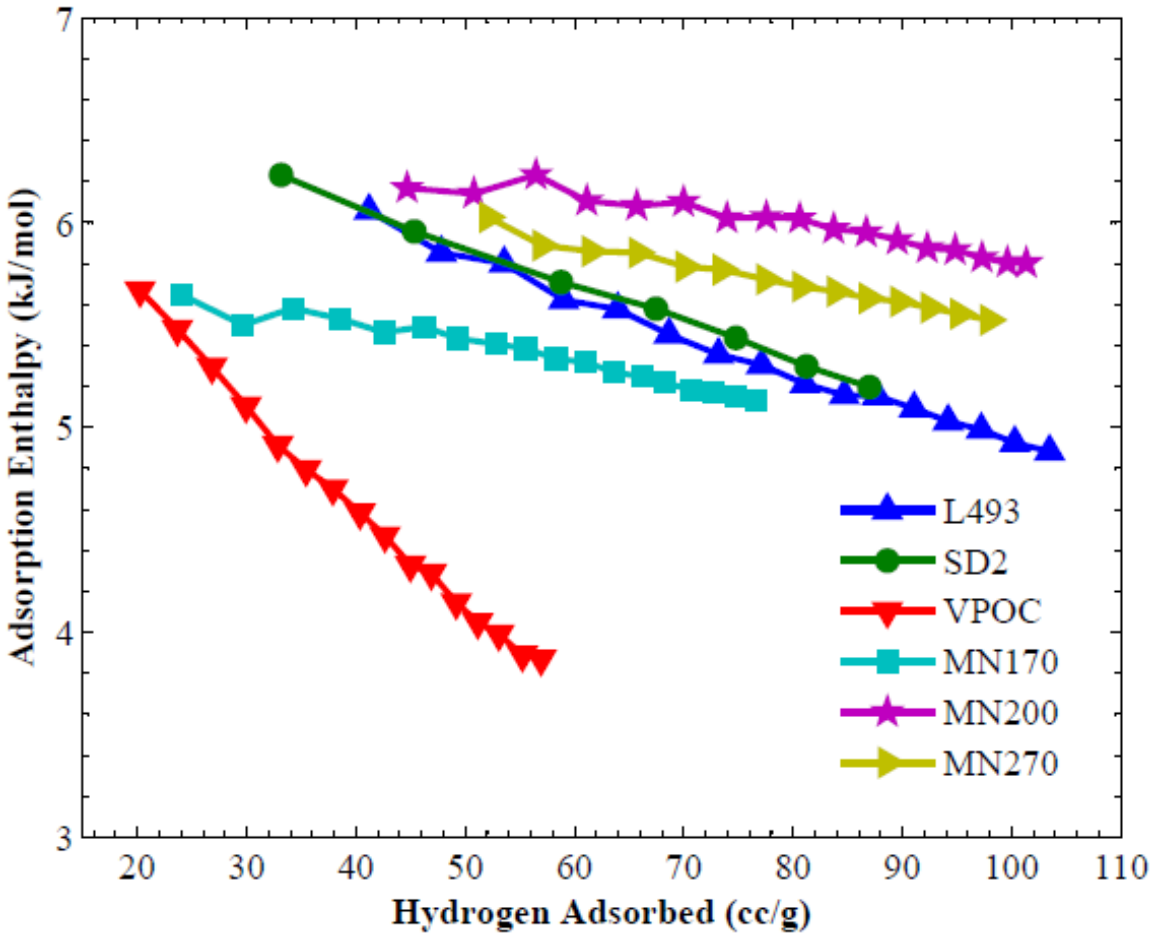

Figure 3.4. Adsorption enthalpy of the commercial HPS.

3.3.2. Spillover Enhancement

The powder X-ray diffraction spectra of MN270, MN270-6wt%Pt and MN270-bridged are given in Figure 3.5. The plain MN270 diffraction pattern does show amorphous behavior with the absence of any sharp crystalline peaks. However, for the wet impregnated and bridged samples, the Pt peaks at 2θ = 39.6° and 46.3° can be attributed to the (111) and (200) plane reflections (ref. code 00-001-1190 from the International Center for Diffraction Data (ICDD) database). As evident from the Pt peak at 39.6 2θ°, MN270-6wt%Pt has a broader and stronger peak compared to MN270-bridged due to its smaller Pt particle size and higher loading. By using the Scherrer's

formula [202], the broadness of the Pt peak can be used to calculate the average Pt particle size of MN270-6wt%Pt and MN270-bridged which are about 3.9nm and 9.9nm, respectively. The relative intensity of the Pt peaks is related to the Pt loading of the samples, which is higher in MN270-6wt%Pt, and is further discussed in relation to the SEM-EDX analysis below. The Pt particle size distribution of MN270-6wt%Pt and MN270-bridged was further examined by TEM.

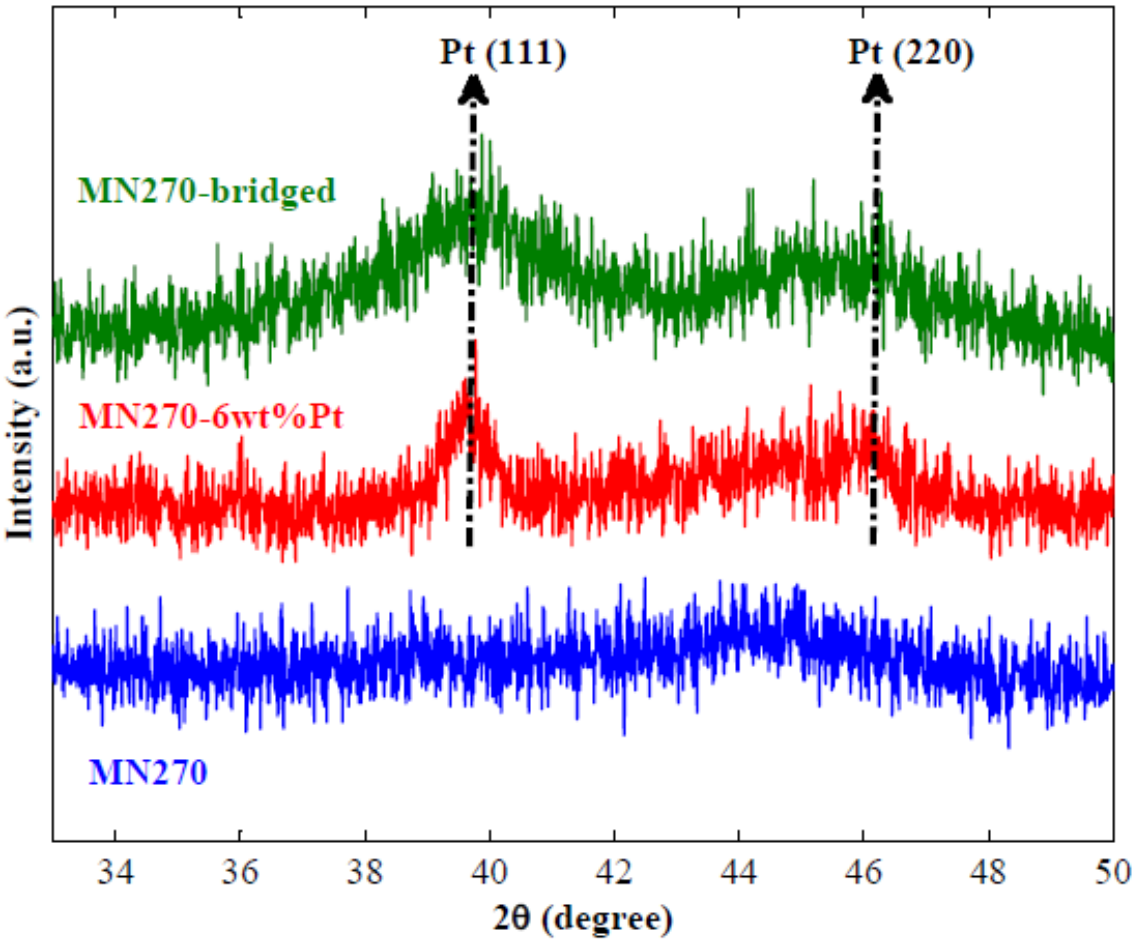

Figure 3.5. XRD spectra of MN270 (blue), MN270-6wt%Pt (green) and MN270-bridged (red). The Miller indices of the diffraction peaks from Pt are also given.

As shown in Figure 3.6, the Pt particle size of MN270-6wt%Pt is around 2-5nm, and in agreement with 3.9nm obtained from the Scherrer's formula. On the other hand,

the Pt particle size of MN270-bridged shows a broad distribution. As seen from Figure 3.6 (B1) and (B3), Pt particles bigger than 10nm (i.e., ≈ 15nm) and as small as 2nm are visible, respectively. The effect of the Pt particle size on spillover enhancement in relation to the bridge building technique is further discussed below.

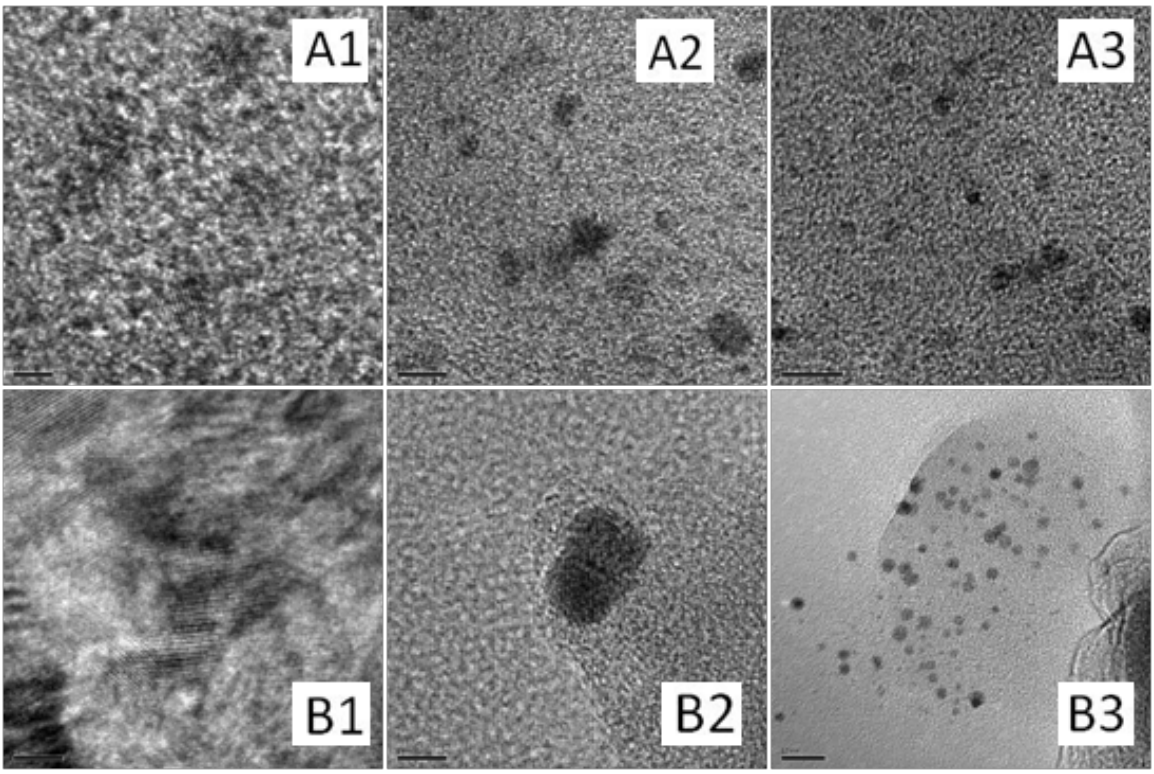

Figure 3.6. (A1-A3): TEM images of MN270-6wt%Pt; scale bar in (A1), (A2) and (A3) corresponds to 2nm, 5nm and 10nm, respectively. (B1-B3): TEM images of MN270-bridged; scale bar in (B1), (B2) and (B3) corresponds to 5nm, 5nm and 10nm, respectively.

The nitrogen uptake of MN270, MN270-6wt%Pt and MN270-bridged at 77 K are given in Figure 3.7. All three isotherms show a combination of type I and IV curves according to the International Union of Pure and Applied Chemistry (IUPAC) classification and a slight hysteresis in the desorption branch (only MN270 shown for clarity) can be attributed to the swelling of the polystyrene matrix [80]. The nitrogen isotherms also give insight to the pore structure of the samples; high uptake at low

pressures ($P/P_o < 0.1$) due to microporosity, gradual increase in the region $0.1 < P/P_o < 0.9$ due to mesoporosity, and the steep increase at high pressures ($P/P_o > 0.9$) attributed to macroporosity [203].

Pt doping decreased the surface area and pore volume for both MN270-6wt%Pt and MN270-bridged due to pore blocking as summarized in Table 3.2. The pore blocking effect is visible from the nitrogen adsorption isotherms since both of the Pt doped samples' nitrogen uptake at low pressure ($P/P_o < 0.1$) is considerably lower than the base material. The pore blocking was further confirmed by using hydrogen as a probe molecule which has a smaller cross sectional area compared to nitrogen.

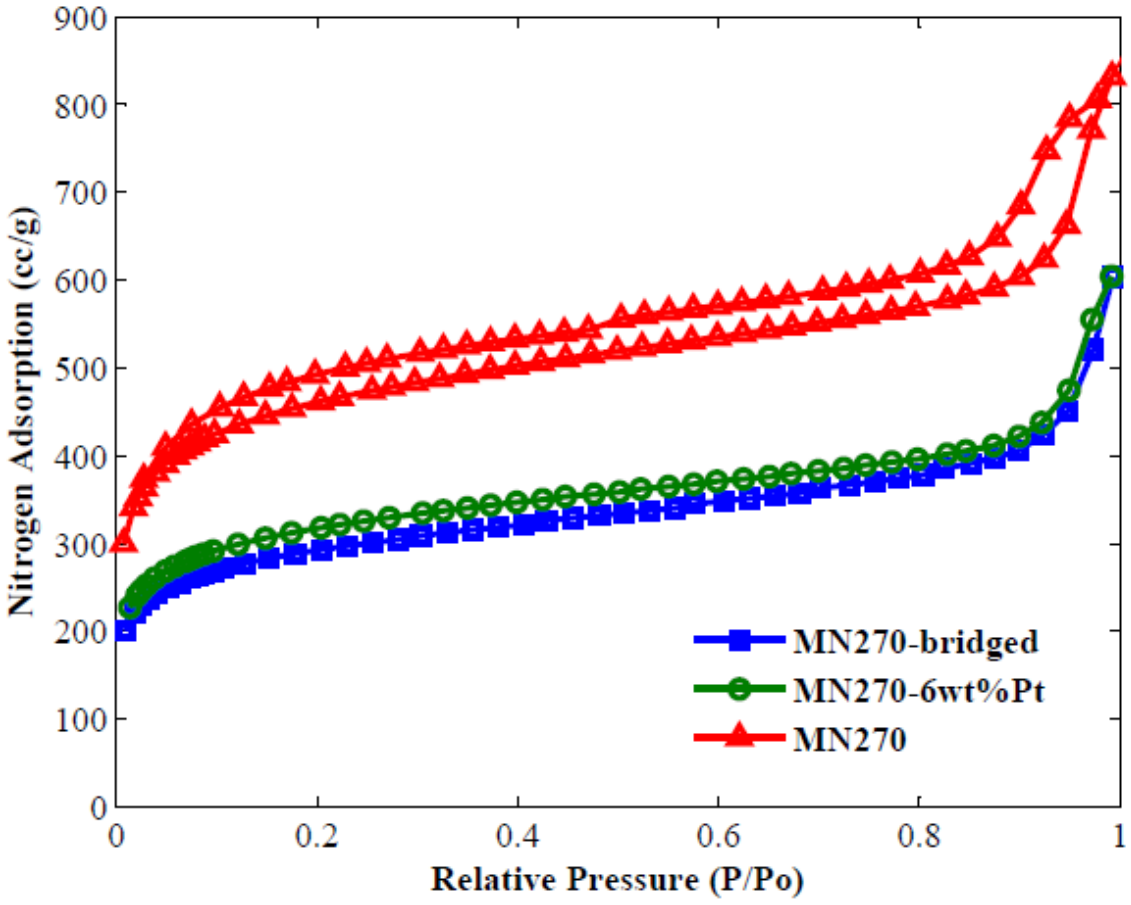

Figure 3.7. Nitrogen uptake of MN270, MN270-6wt%Pt and MN270-bridged at 77 K.

The SEM images of MN270, MN270-6wt%Pt, and MN270-bridged are given in Figure 3.8. Both MN270 and MN270-6wt%Pt have similar morphological characteristics, and are composed of HPS particles ranging from 1 to 20 μm. However, in the MN270-bridged sample, the voids between HPS particles were filled with, Pt/AC catalyst, carbon bridges formed during the bridge building procedure, or both due to their smaller particle size.

The SEM-EDX analysis, as shown in Figure 3.9, was used to reveal the elemental composition of the samples. The EDX quantitative analysis results are given in Table 3.3. Since EDX is not sensitive to hydrogen, considering the molecular structure of the polystyrene (i.e., benzene ring), the hydrogen atomic percentage (at. %) was assumed to be the same as the carbon at. %, and the results were corrected accordingly. Based on the corrected at. % of each element, the calculated wt. % values are given in Table 3.3.

Table 3.2. Structural and hydrogen uptake characteristics of MN270, MN270-6wt%Pt, MN270-bridged and Pt/AC.

compound	**surface area** [a] **(m^2/g)**	**V_{tot}** [b] **(cc/g)**	**V_{micro}** [c] **(cc/g)**	**H_2 Uptake** [d] **77K (wt%)**	**H_2 Uptake** [e] **294K (wt%)**
MN270	1451	1.09	0.63	1.53	0.33 ± 0.01
MN270-6wt%Pt	1162	0.94	0.51	1.20	0.32 ± 0.01
MN270-bridged	1068	0.94	0.47	1.15	0.36 ± 0.01
Pt/AC	866	0.73	0.37	1.26	0.30 ± 0.02

[a] Calculated from N_2 adsorption at 77 K using the BET equation in the 0.01 to 0.1 pressure range. [b] Total pore volume calculated using N_2 adsorption at P/P_o=0.99. [c] Total micropore volume calculated using N_2 adsorption at P/P_o=0.25. [d] Hydrogen uptake at 1 atm and 77 K. [e] Hydrogen uptake at 100 atm and 294 K.

The EDX results cannot be taken unambiguously because, with EDX, only certain regions of the material can be investigated (i.e., 1 mm^2 area in this case). The carbon tape used to attach the powders to the sample holder might also have affected the carbon peak intensity. The EDX spectra were collected from at least three different regions with

similar results. On the other hand, EDX spectra can shed light on the chemical composition of the samples. As expected, MN270-bridged has the highest C ratio compared to the others due to excess carbon in Pt/AC and D-Glucose.

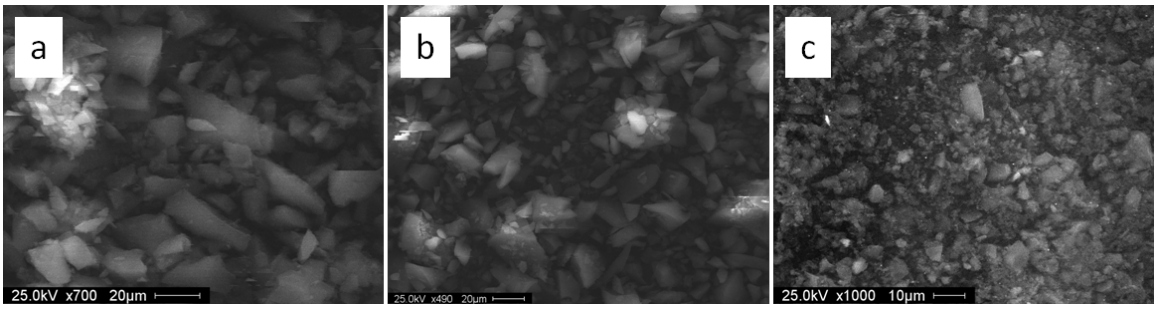

Figure 3.8. SEM images of (a) MN270, (b) MN270-6wt%Pt and (c) MN270-bridged.

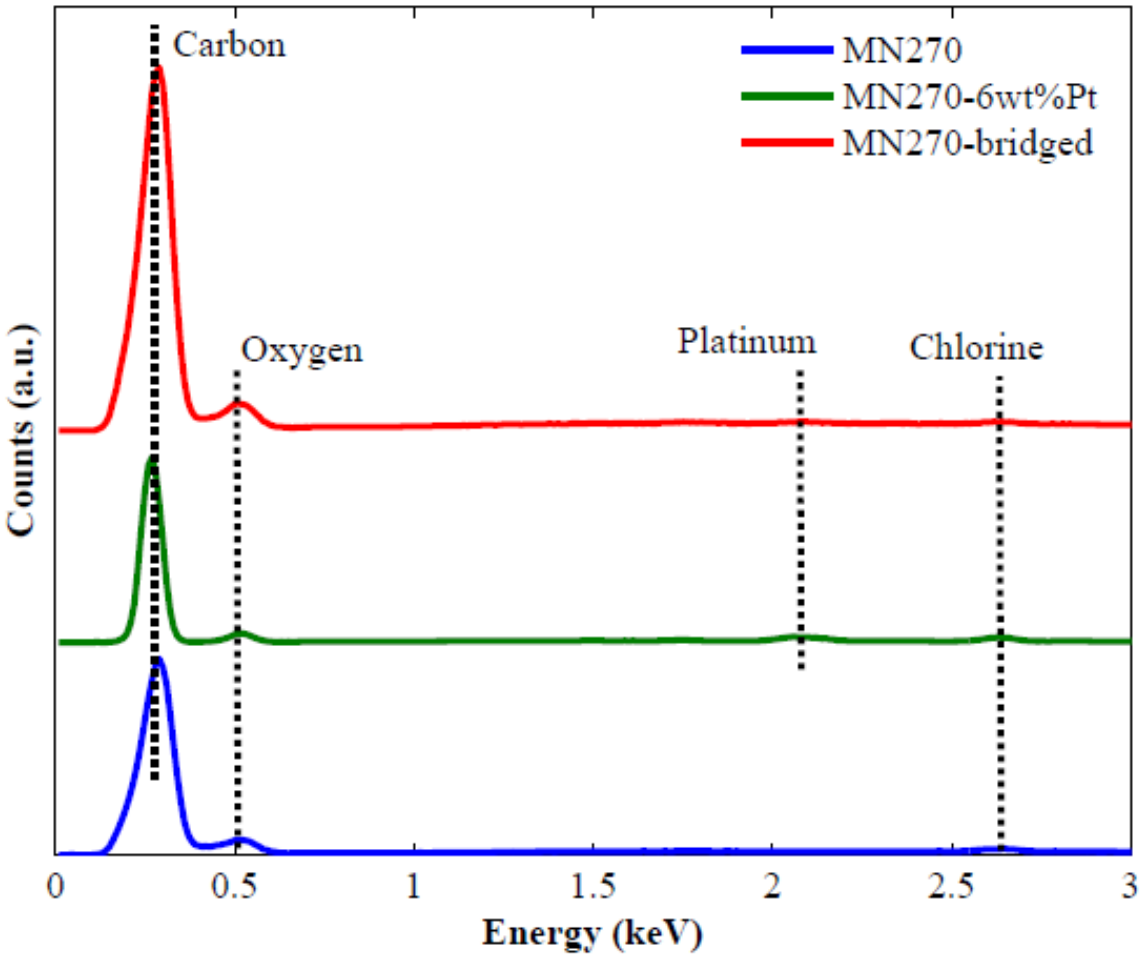

Figure 3.9. SEM-EDX spectra of MN270, MN270-6wt%Pt and MN270-bridged.

The oxygen content is the highest in MN270, which is due to carboxyl/hydroxyl functionalities in MN270 [204,205] as revealed by the FTIR analysis. As shown in Figure 3.10, carbonyl peaks in the 1500-1900 cm^{-1} and hydroxyl peaks in the 3100-3900 cm^{-1} are clearly visible. The decrease of the oxygen content in MN270-6wt%Pt can be attributed to the hydrogen reduction performed at an elevated temperature (200 °C) for 5h. The relatively small increase of the oxygen content in MN270-bridged compared to MN270-6wt%Pt might be related to the incomplete reduction of the D-glucose which has hydroxyl groups.

Table 3.3. SEM-EDX quantitative analysis of MN270, MN270-6wt%Pt, and MN270-bridged.

sample	**weight percentage**				
	carbon	**hydrogen**	**oxygen**	**chlorine**	**platinum**
MN270	77.1	6.4	15.6	0.9	–
MN270-6wt%Pt	78.9	6.5	10.5	0.8	3.3
MN270-bridged	80.6	6.7	12.3	0.1	0.3

The chlorine content in the samples is most likely due to impurities remaining after hypercrosslinking of the polystyrene via the Friedel-Crafts reaction [87]. Another possibility to consider is that the presence of chlorine impurities might be due to incomplete reduction of the $PtCl_6$ ions (for MN270-6wt%Pt). However, this possibility was ruled out because the chlorine content did not increase after the Pt doping of the base material MN270 as seen from Table 3.3. Pt/AC is the source of Pt in MN270-bridged, and from the stoichiometric analysis, (weight ratio of MN270, D-Glucose, and Pt/AC is 8:1:1, respectively) the Pt content of MN270-bridged is 0.5 wt. %. However, the Pt content is 0.3 wt. % from the EDX analysis compared to 0.5 wt. % calculated from the stoichiometric analysis which shows that the EDX analysis underestimates the Pt content in MN270-bridged; if this is so, the Pt content in MN270-6wt%Pt could also be higher

(≈5.6wt. %) than the 3.3 wt. % given by the EDX analysis. In any case, the Pt content given by the EDX analysis can be considered as the minimum level of Pt concentration.

Figure 3.11 represents the hydrogen uptake at 77 K and 1 atm for MN270, MN270-6wt%Pt, MN270-bridged, and Pt/AC. The reduction of the hydrogen uptake in MN270-6wt%Pt and MN270-bridged compared to MN270 is resulting from the lower surface area and pore volume of the Pt doped samples as indicated in Table 3.2. Reduction in the hydrogen uptake occurs because Pt does not play any role in hydrogen uptake at low temperatures (i.e., no spillover at 77 K) [206].

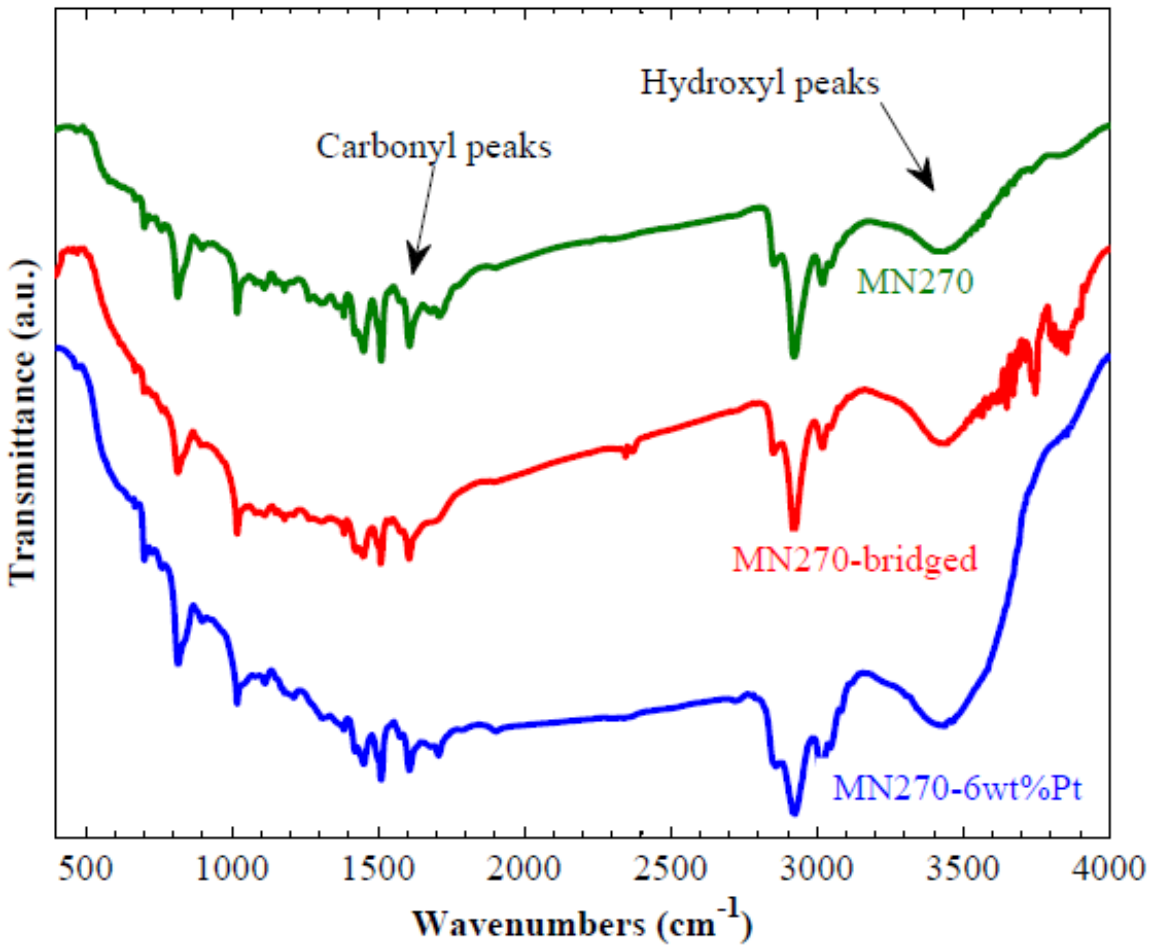

Figure 3.10. FTIR spectra of MN270 (green), MN270-bridged (red), MN270-6wt%Pt (blue).

The RT hydrogen pressure-concentration isotherms of MN270, MN270-bridged, and MN270-6wt%Pt up to 100 atm are shown in Figure 3.12 and summarized in Table 3.2. All the isotherms showed repeatability between successive measurements after evacuation at 150°C for at least 12 h, and error bars based on three measurements are also plotted in Figure 3.12. Typical sorption kinetics data for the best performing material, MN270-bridged, is given in Figure 3.13. The kinetics data shows that equilibrium has been reached for each pressure-concentration data point shown in Figure 3.12. The initial (i.e., 0-10 atm) steep rise in the hydrogen uptake of the Pt doped samples seen in Figure 3.12 can be attributed to the chemisorption of the hydrogen at low pressure.

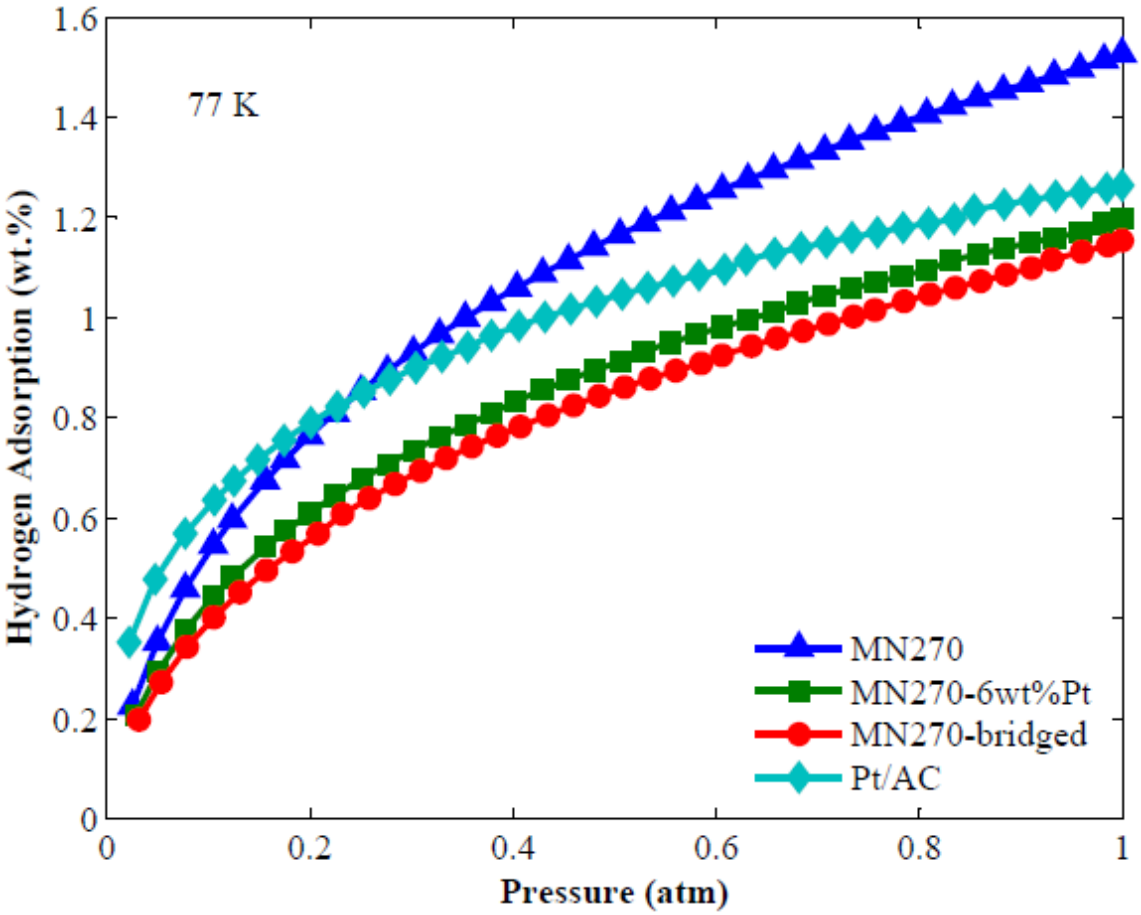

Figure 3.11. Hydrogen uptake of MN270, MN270-bridged, MN270-6wt%Pt, and Pt/AC at 77 K and 1 atm.

As seen in Figure 3.12, MN270-bridged has the highest uptake of 0.36 wt. % at 294 K and 100 atm; however, this is only 10 % higher than the base material MN270 and of insignificant value for the RT hydrogen uptake enhancement.

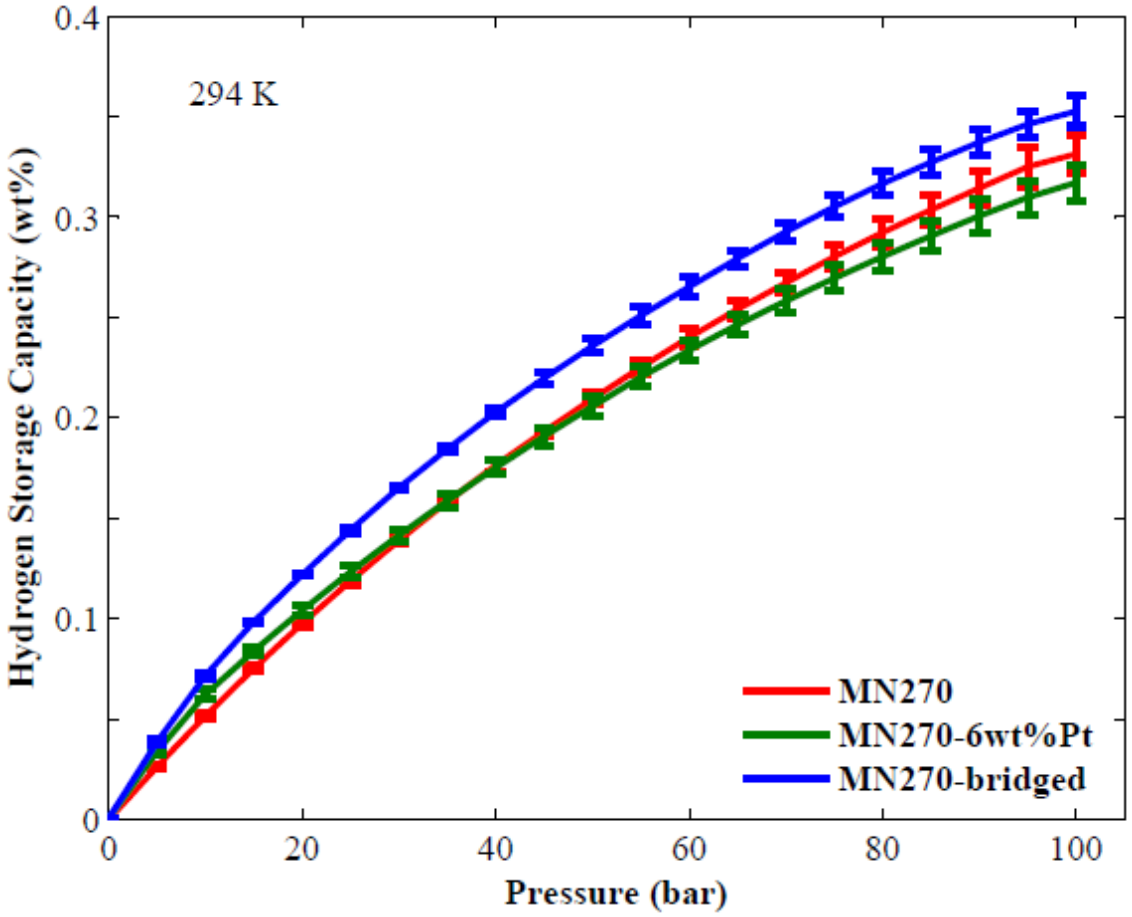

Figure 3.12. Hydrogen uptake of MN270, MN270-bridged and MN270-6wt%Pt.

The sample MN270-6wt%Pt did not show any enhancement in hydrogen uptake compared to MN270 despite its higher Pt content and smaller Pt particle size as compared to MN270-bridged. The Pt content appeared to be of minimal effect but the dispersion and particle size of the Pt was considered important for spillover enhancement [199]. However, this alone cannot explain the better performance of the MN270-bridged over the MN270-6wt%Pt, because MN270-bridged has bigger Pt particles on average.

Moreover, the effectiveness of the bridge building technique can be better understood from the TEM images given in Figure 3.6. The sample MN270-6wt%Pt has a narrow Pt particle size distribution (2-5nm), whereas MN270-bridged has a broad Pt particle size distribution (2-15nm).

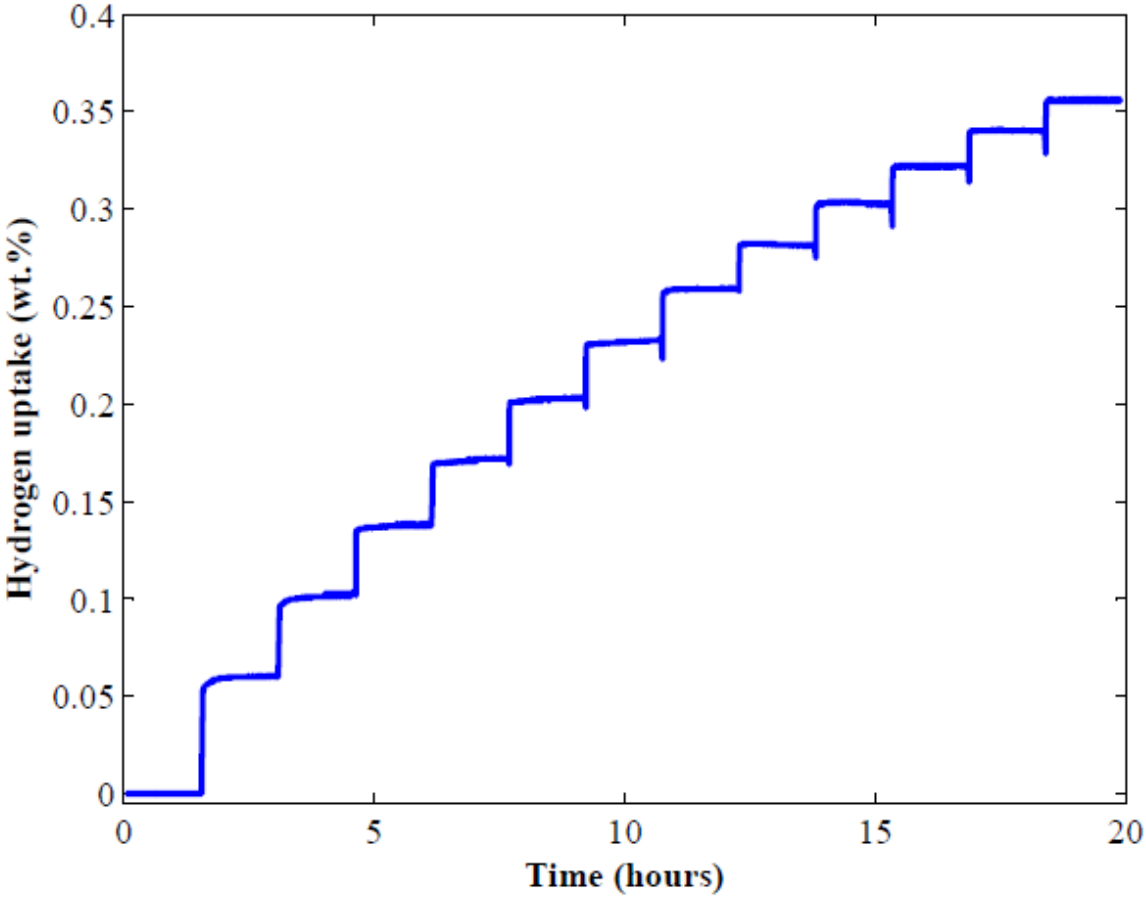

Figure 3.13. Kinetic hydrogen uptake of MN270-bridged.

Although the Pt particles in MN270-6wt%Pt is smaller on average compared to MN270-bridged, MN270-6wt%Pt did not show higher hydrogen uptake at RT. On the contrary, MN270-bridged outperformed MN270-6wt%Pt as seen from Figure 3.12. Therefore, the bridge building technique is more effective than the wet impregnation method on the spillover enhancement by enabling closer contacts between the polymer

matrix and the Pt. However, optimal design of the Pt/AC catalyst needs to be further explored to fully exploit the potential of the bridge building technique.

The role of the surface oxygen groups on the spillover enhancement, studied for activated carbon and graphite oxide, showed enhanced hydrogen uptake compared to the base materials [207]; however, MN270 should be further investigated to establish if oxygen functionalities are favorable or not.

3.4. Conclusions

In this study, six different commercially available hypercrosslinked polystyrenes (HPS) were screened considering the specific surface area, pore size distribution, pore volume, and adsorption enthalpy. MN270 was selected for the RT spillover study mainly due to its high surface area, narrow pores, and relatively high pore volume/adsorption enthalpy. The spillover enhancement by Pt doping was investigated by utilizing two different synthesis methods; wet impregnation (i.e., MN270-6wt%Pt) and the bridge building technique (MN270-bridged). MN270-bridged showed a 10% increase in hydrogen uptake at 294 K and 100 atm compared to the base material MN270, whereas MN270-6wt%Pt did not show any enhancement. The results showed the efficacy of the bridge building technique; however, to take full advantage of this technique an optimal Pt/AC catalyst needs to be designed. Nevertheless, a 10 % enhancement has an insignificant value for practical applications, and is considerably low compared to MOFs and AC [41]. The spillover enhancement for hydrogen storage continues to be a highly disputable topic due to conflicting results for the same materials (i.e., MOFs, AC). Since there is no spillover enhancement study for polymers, it was not possible to compare the results of this study with those of other groups, yet considering the similarity of the

organic building block of the HPS with MOFs and COFs (i.e., benzene ring), the reasons underlying the considerably small spillover enhancement in the hydrogen uptake of the HPS needs to be further investigated.

Chapter 4. Reversible Hydrogen Storage in the Li-Mg-N-H System – The Effects of Ru Doped Single Walled Carbon Nanotubes on NH_3 Emission and Kinetics

4.1. Introduction

Complex hydrides were subject to intensive research efforts as a solid state reversible hydrogen storage material for mobile and stationary applications during the last decade [208,209]. Among the complex hydrides, amide-hydride systems are considered as one of the viable candidates after Chen et al. first reported the promising results for the lithium nitride system in which the reaction steps are given as [52]

$$Li_3N+2H_2 \leftrightarrow Li_2NH+LiH+H_2 \leftrightarrow LiNH_2+2LiH \quad (4.1)$$

The theoretical capacity of the Li_3N system is 10.4 wt. %; however, only the second step of the reaction path, given in Eq. 4.1 (i.e., Li-N-H system hereafter), is practical for reversible hydrogen storage since the first reaction step has a very low equilibrium pressure (i.e., 0.07 bar H_2) [52]. Further investigation of the Li-N-H system, which has a theoretical capacity of 6.5 wt. %, revealed the elementary steps presented in Eqs. 4.2a and 4.2b [210]. The reaction between LiH and NH_3 (i.e., Eq. 4.2b) was found to be ultrafast (i.e., 25 ms) [210] and responsible for the capture of NH_3 which is detrimental to proton exchange membrane (PEM) fuel cells even at trace levels [122].

$$2LiNH_2 \rightarrow Li_2NH+NH_3 \quad (4.2a)$$

$$NH_3+LiH \rightarrow LiNH_2+H_2 \quad (4.2b)$$

The Li-N-H system has a relatively low plateau pressure depending on the operating temperature (i.e., 0.2 bar at 195 °C, 0.5 bar at 230 °C, 1.5 bars at 255 °C and 1.5 – 3 bars at 280-375 °C) [52,211]. Therefore, destabilization of the Li-N-H system could shift the plateau pressure to higher pressures and lower the desorption temperature. One of the ways to destabilize the Li-N-H system is to replace Li with a more electronegative atom such as Mg, since MgH_2 is less stable than LiH [53]. Nakamori et al. achieved 50 K reduction in the desorption temperature by partially replacing Li in $LiNH_2$ with 90 at. % Li and 10 at. % Mg [54]. Later, Luo developed a new hydrogen storage material (i.e., the Li-Mg-N-H system hereafter) by completely replacing LiH with MgH_2 [53]. The Li-Mg-N-H system has a ≈ 4.5 wt. % gravimetric capacity with a plateau pressure of 30 bar at 200 °C [53]. The proposed reaction mechanism for the Li-Mg-N-H system is given in Eq. 4.3 [212,213]. The starting materials, $MgH_2 + 2LiNH_2$, transform to $Mg(NH_2)_2 + 2LiH$ after the first ab/desorption cycle, that is, the second step in Eq. 4.3 is the reversible reaction in the Li-Mg-N-H system.

$$MgH_2 + 2LiNH_2 \leftrightarrow Li_2Mg(NH)_2 + 2H_2 \leftrightarrow Mg(NH_2)_2 + 2LiH \quad (4.3)$$

Two different reaction mechanisms were proposed for the Li-Mg-N-H system [214]. First, the NH_3 mediated reaction mechanism occurs similar to the Li-N-H system (i.e., Eqs. 4.2a & 4.2b) [215]. The other suggested mechanism is the coordinated two molecule or multimolecular reaction mechanism in which close proximity of the reacting species is crucial [121,216,217]. However, recent studies on the mechanistic investigation of the Li-N-H system revealed that the NH_3 mediated reaction mechanism is more likely; in addition, Li ion diffusion is an important parameter in re/dehydrogenation according to the proposed reaction mechanism [218-222]. Therefore, strategies that can enhance the Li

ion mobility in amide-hydride systems are highly desirable to improve the sluggish kinetics of these systems. To achieve this goal, single walled carbon nanotubes (SWCNTs) are considered as a viable catalyst that needs to be investigated since Li ion freely diffuse inside SWCNTs [125,223-225]. However, structural defects (i.e., openings on the wall) on the SWCNTs are required to facilitate the diffusion of the Li ions in and out of the SWCNTs.

Another drawback of the Li-Mg-N-H system is the concomitant NH_3 emission during hydrogen desorption which is more pronounced compared to the Li-N-H system since the reaction rate of NH_3 with MgH_2 is slower than that of LiH [60,226,227]. Besides being detrimental to PEM fuel cells, NH_3 emission also causes loss of gravimetric capacity over a number of cycles [123,228,229]. Ru is one of the most active catalysts for NH_3 decomposition [124], and has been studied extensively for the generation of hydrogen for fuel cells through NH_3 decomposition [230-232]. Moreover, among various supports (i.e., graphite, activated carbon, alumina etc.) for Ru, carbon nanotubes (CNTs) showed high activity towards NH_3 decomposition [233,234]. On the other hand, Ru is also active for NH_3 synthesis which requires high pressures (> 50 bar) whereas NH_3 decomposition requires low pressures (≈ 1 bar) [235,236]. Since under practical operating conditions hydrogen desorption from the Li-Mg-N-H system occurs at low pressures (≈ 1 bar), Ru included as a catalyst, can be more effective for the decomposition rather than synthesis of NH_3.

In the quest for finding an optimal catalyst for the Li-Mg-N-H system, Ru doped CNTs can be used as a suitable catalyst considering the aforementioned drawbacks (i.e., sluggish kinetics and NH_3 emission) of the Li-Mg-N-H system. The studies on the effects

of carbon structures on the amide-hydride systems are scarce [237]. To date, only the effects of SWCNTs [238] and Ru doped graphite [239] in the Li-Mg-N-H system have been studied so far. Both of these works reported improved kinetics, but no NH_3 emission even from the base Li-Mg-N-H sample. However, NH_3 emission from the Li-Mg-N-H system is an important issue and has been studied extensively [60,121,228,229,240].

There are two goals in this study. First, study the hydrogen ab/desorption kinetics and the NH_3 emission characteristics of the Li-Mg-N-H system for a wide range of preparation conditions to elucidate the effects of the ball milling parameters. Second, study the effects of the SWCNTs and the Ru-doped SWCNTs catalysts in the Li-Mg-N-H system with a focus on the kinetics and the NH_3 emission characteristics. The results show that intense ball milling enhances the hydrogen ab/desorption kinetics and limits the NH_3 emission. In addition, by adding Ru-doped SWCNTs to the Li-Mg-N-H system, NH_3 emission can be mitigated as compared to adding just SWCNTs.

4.2. Experimental Details

4.2.1. Materials

Starting materials $LiNH_2$, MgH_2 (hydrogen storage grade), $RuCl_3$ (45-55 % Ru content) and ethylene glycol (reagent plus grade) were purchased from Sigma-Aldrich and used without further purification. SWCNTs were purchased from Cheap Tubes with ≈ 99% purity. Impurities in SWCNTs were Fe particles, and confirmed by thermogravimetric analysis (TGA) and energy dispersive X-rays (EDX).

4.2.2. Synthesis

All materials were handled in an argon filled glove box in which oxygen and water levels were below 0.1 ppm. The base materials were prepared by a planetary ball

mill, Fritsch Pulverisette P6, using a stainless steel bowl (80 ml) and stainless steel balls (Ø 10 mm) by mixing $LiNH_2$ and MgH_2 in 2 to 1.1 molar ratios. Excess MgH_2 was added to limit the NH_3 emission [53,227,241]. The milling duration, milling speed and ball to powder ratios of all the samples are given in Table 4.1. The ball milling parameters were chosen to cover the most common values reported in the literature [60,121,228,239,240,242-245] for planetary type ball mills. To limit the temperature increase during ball milling, the ball milling process was stopped for 5 min after every 10 min of milling for all the samples. After adding the SWCNTs and Ru doped SWCNTs catalysts (5 wt. %) to the base material, samples were further ball milled for 60 min at 300 revolutions per minute (RPM) and 60:1 ball to powder ratio.

Table 4.1. Sample preparation details.

Milling Speed (RPM)		**200**	**300**				**400**
Ball to Powder Ratio		**60/1**	**20/1**	**40/1**	**60/1**	**120/1**	**60/1**
Milling Duration	**10 h**				S#7		
	20 h	S#5	S#6	S#4	S#2	S#8	S#3
	40 h				S#1		

The as-milled samples were activated under a 100 bar hydrogen pressure at 220 °C for 24 h by a metathesis reaction given in Eq. 4.4 [246]. The as-milled and activated samples are denoted by suffixes “A” and “B”, respectively, throughout the text. For instance, the as- milled sample 3 (S#3) is named S#3A, and the activated S#3 is named S#3B.

$$MgH_2 + 2LiNH_2 \rightarrow Mg(NH_2)_2 + 2LiH \quad (4.4)$$

Ru doped SWCNTs (SWCNT-20Ru hereafter) were prepared by using a method slightly different than that that presented in literature [247]. Since 99% pure SWCNTs were used in this study, the initial purification step (i.e., refluxing in a concentrated nitric acid for 8 h) was skipped. Briefly, a 200 mg of SWCNTs in a 100 ml 2.6 M nitric acid was first sonicated (100 W, 42 kHz) for 2 min to break-up the SWCNT bundles. Then, the SWCNTs were refluxed in 2.6 M nitric acid for 8 h to create anchoring points for Ru nanoparticles. After cooling to room temperature, the oxidized SWCNTs (SWCNT-Ox hereafter) were centrifuged at 5000 RPM for 15 min, twice washed with deionized (DI), centrifuged and decanted. The SWCNT-Ox were dried overnight in an oven at 60 °C. For Ru doping, a 100 mg of SWCNT-Ox and a 40 mg of $RuCl_3$ (20 wt. % nominal Ru loading) were dispersed in a 200 ml ethylene glycol-DI water solution (3:2 by volume) by sonicating for 2 min. Then, the mixture was refluxed at 120-130 °C for 8 h. After cooling to room temperature, the mixture was centrifuged, decanted, washed with a slightly acidic (by adding few drops of concentrated hydrochloric acid) DI water, centrifuged again, and then dried in an oven overnight at 60 °C. This sample is named SWCNT-20Ru.

4.2.3. Characterization

The powder X-ray diffraction (XRD) of the samples was carried out by a custom-built air tight stainless steel sample holder [143] or a zero diffraction sample holder using a Philips X'pert diffractometer with CuKα radiation of λ=1.54060 Å. The samples were prepared inside the glove box and sealed with a Mylar® or a Kapton® film depending on the peak positions of interest. Diffraction data was analyzed using PANalytical X'pert Highscore software version 1.0f. Scanning electron microscopy (SEM), JEOL S800, with

EDX and transmission electron microscopy (TEM), Tecnai F20, were utilized to investigate the surface morphology, chemical composition of the elements and the size/dispersion of the Ru particles. The gravimetric weight loss was analyzed by a TA Instrument's SDT-Q600, and the data was analyzed with a TA Universal Analysis 2000 software. The nitrogen adsorption isotherms were measured at 77 K by a Quantachrome AS1C. The measurement accuracy and repeatability of the Quantachrome AS1C were verified with the Quantachrome standard reference material (SARM-2012) before the measurements. The test value was within the reproducibility limit (± 5 %) of the expected value. The adsorption data was analyzed by a Quantachrome AS1Win software. The specific surface area (SSA) of the samples was calculated from nitrogen adsorption at 77 K using the Brunauer-Emmett-Teller (BET) equation in the 0.05 to 0.3 P/P_o relative pressure range. The pore size distribution (PSD) of the samples was calculated by the non-local density functional theory (NLDFT) using a cylindrical or a hybrid slit/cylindrical pore model (i.e., slit pore geometry for pores < 2nm and cylindrical pore geometry for pores > 2nm) based on whichever of the models resulted in a better fit to the experimental data. The high pressure hydrogen pressure-concentration-temperature (PCT) isotherms and kinetics data were collected with Setaram-HyEnergy PCTPro 2000, Sievert's type apparatus. The sample loading was ≈ 500 mg or greater for each sample. The uncertainties associated with the hydrogen storage measurements are thoroughly discussed in the previous work [248]. The Hydrogen and NH_3 release characteristics of the samples were determined unambiguously by an MKS Cirrus mass spectrometer (under 50 ml He flow and 5 K/min heating rate) in a custom built setup, and details are given elsewhere [249]. Ammonia, hydrogen and nitrogen were tracked by m/z = 17, m/z

= 2 and m/z = 28, respectively. Raman experiments were carried out using a Confocal Raman Microscope (Olympus, IX71) purchased from Horiba Jovin Yvon. For all experiments, an excitation wavelength at 647 nm from an Argon and Krypton laser (Coherent, Innova 70C series) has been used with 5 mW of power, 10 s of exposure time and 3-5 accumulations. The spectrograph grating was 600 grooves/mm and the 20X objective was used throughout the experiments. Raman measurements were taken at various locations on the samples to account for the heterogeneity of the solid samples.

4.3. Results and Discussion

4.3.1. Effects of Ball Milling Parameters on the Kinetics and NH_3 Emission Characteristics of the Li-Mg-N-H System

The XRD patterns of the as-milled and the activated samples prepared by different ball milling parameters (see Table 4.1) are given in Figure 4.1 and Figure 4.2, respectively. Selecting a more aggressive processing condition by increasing the milling duration (S#1A) or milling speed (S#3A) or ball to powder ratio (S#8A) resulted in very small crystallite sizes with none of the diffraction peaks being discernible in Figure 4.1 for S#1A, S#3A and S#8A. The Scherrer crystallite size and the SSA of the as-milled and activated samples are given in Table 4.2. Upon activation, crystallite sizes of all the samples were increased to 20-30 nm range. On the other hand, the SSA of all the samples but S#4 and S#7 were decreased.

In general, the SSA of the as-milled samples decreased by selecting more aggressive ball milling parameters (i.e., S#5A and S#6A have the highest SSA as opposed to S#3A and S#8A which have the smallest SSA) because the samples start to agglomerate by prolonged and intense ball milling [250].

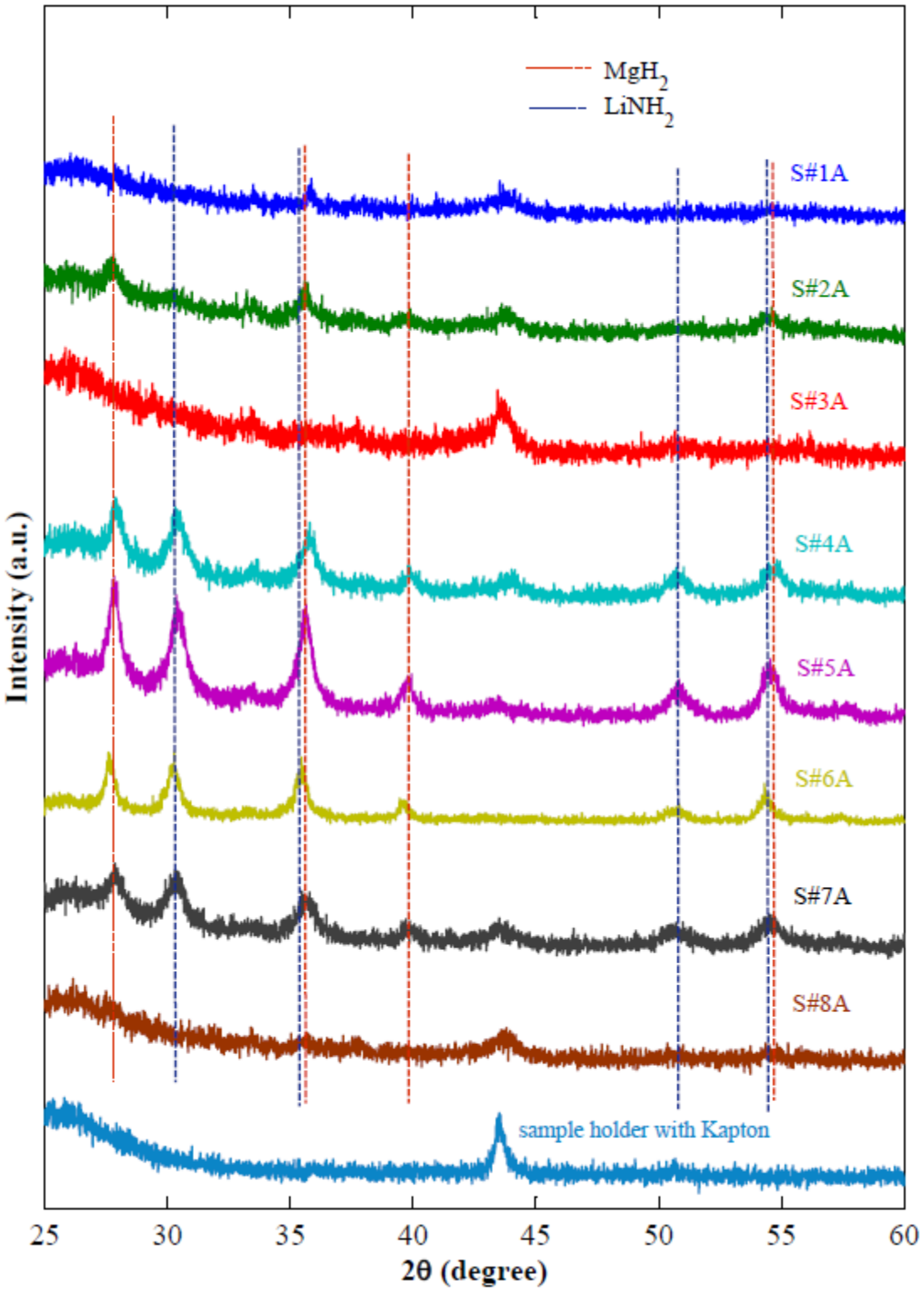

Figure 4.1. XRD patterns of the as-milled Li-Mg-N-H samples with different processing conditions.

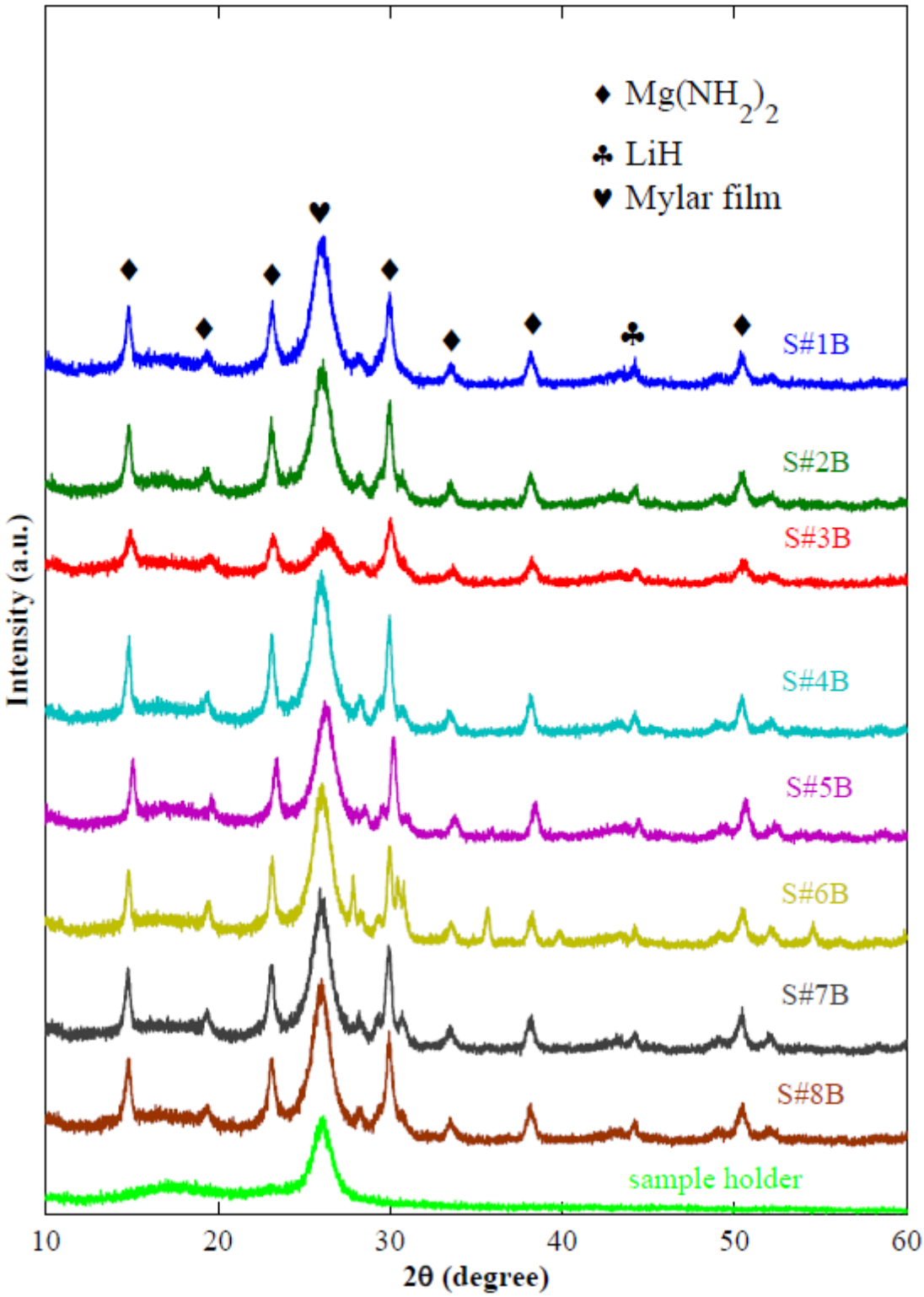

Figure 4.2. XRD patterns of the activated Li-Mg-N-H samples with different processing conditions.

None of the activated samples can be considered as a high surface area material (S#7B, 20 m^2/g being the highest). Therefore, ball milling is an effective way of creating small crystallite size samples but it is not that effective in creating high surface area samples. The absorption and desorption kinetics of all the samples are given in Figure 4.3. Intense ball milling (i.e., smaller crystallite size) resulted in faster ab/desorption kinetics, desorption being always faster than the absorption.

Table 4.2. Specific surface area, crystallite size and NH_3 to hydrogen signal ratio of the as-ball milled and activated samples.

Sample		SSA (m^2/g)	Crystallite size (nm)	Area Under Curve § NH_3/H_2 (%)
S#1	A	19	–*	0.39
	B	6	24	
S#2	A	12	10	0.66
	B	10	23	
S#3	A	12	–*	0.46
	B	5	19	
S#4	A	13	16	0.56
	B	19	28	
S#5	A	41	15	0.85
	B	19	29	
S#6	A	40	20	13.4
	B	16	30	
S#7	A	15	13	1.08
	B	20	23	
S#8	A	10	–*	0.38
	B	8	22	
MgH_2†		1	> 100	–
$LiNH_2$†		3	> 100	–

* No peaks are discernible in the XRD pattern (see Figure 4.1) to determine the Scherrer crystallite size reliably. † As-received starting materials for the synthesis of S#1-8. § Area under curve was calculated by trapezoidal integration using the mass spectrometry raw data up to 250 °C for the activated samples after the 1st cycle. The base line is subtracted from the hydrogen and NH_3 signals for each sample.

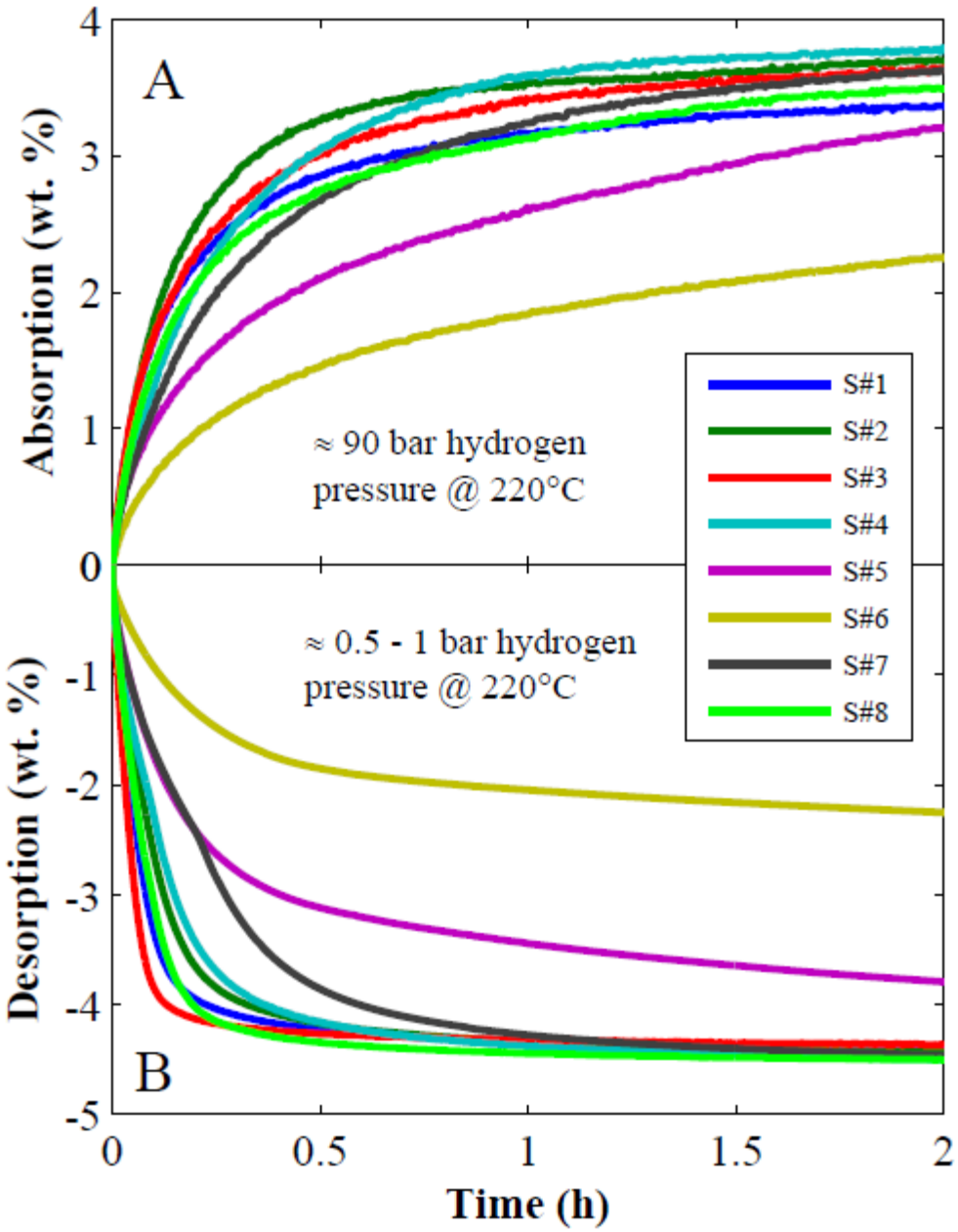

Figure 4.3. Absorption and desorption kinetics of the activated samples S#1-8.

The samples S#5, S#6 and S#7 performed the worst in terms of ab/desorption kinetics due to their relatively bigger crystallite sizes. On the other hand, the samples S#2 and S#3 showed the fastest absorption and desorption kinetics, due to their smaller crystallite sizes. The cyclic absorption and desorption kinetics performances of S#3 are

given in Figure 4.4 and Figure 4.5, respectively. The absorption kinetics showed similar performance over 77 cycles; however, the desorption kinetics degraded considerably, though being still faster than the absorption kinetics.

There are a couple of studies in the literature reporting no NH_3 emission from the Li-Mg-N-H system [238,239,251]. However, as mentioned in the introduction, NH_3 emission is a known issue in the Li-Mg-N-H system. Therefore, the NH_3 emission characteristics of all the activated samples were investigated to clarify whether the NH_3 emission is related to the preparation conditions.

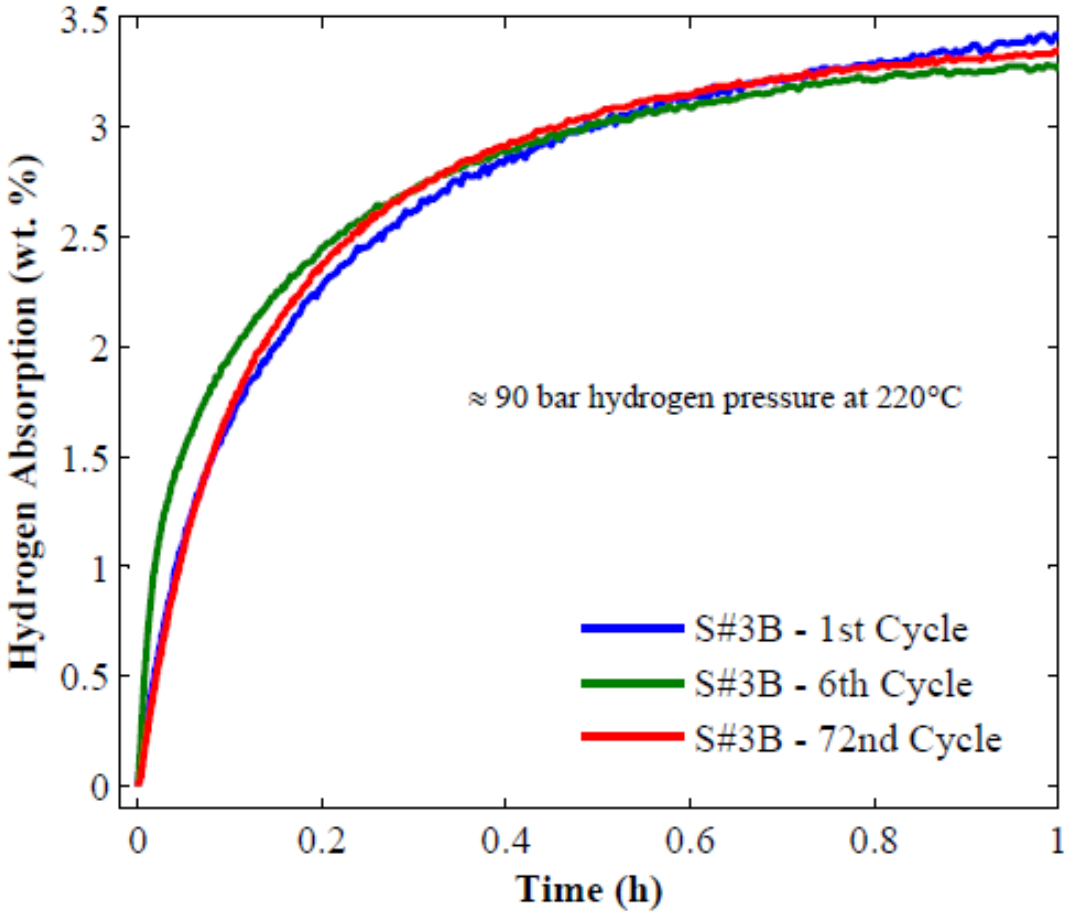

Figure 4.4. Absorption kinetics cycle comparison of S#3.

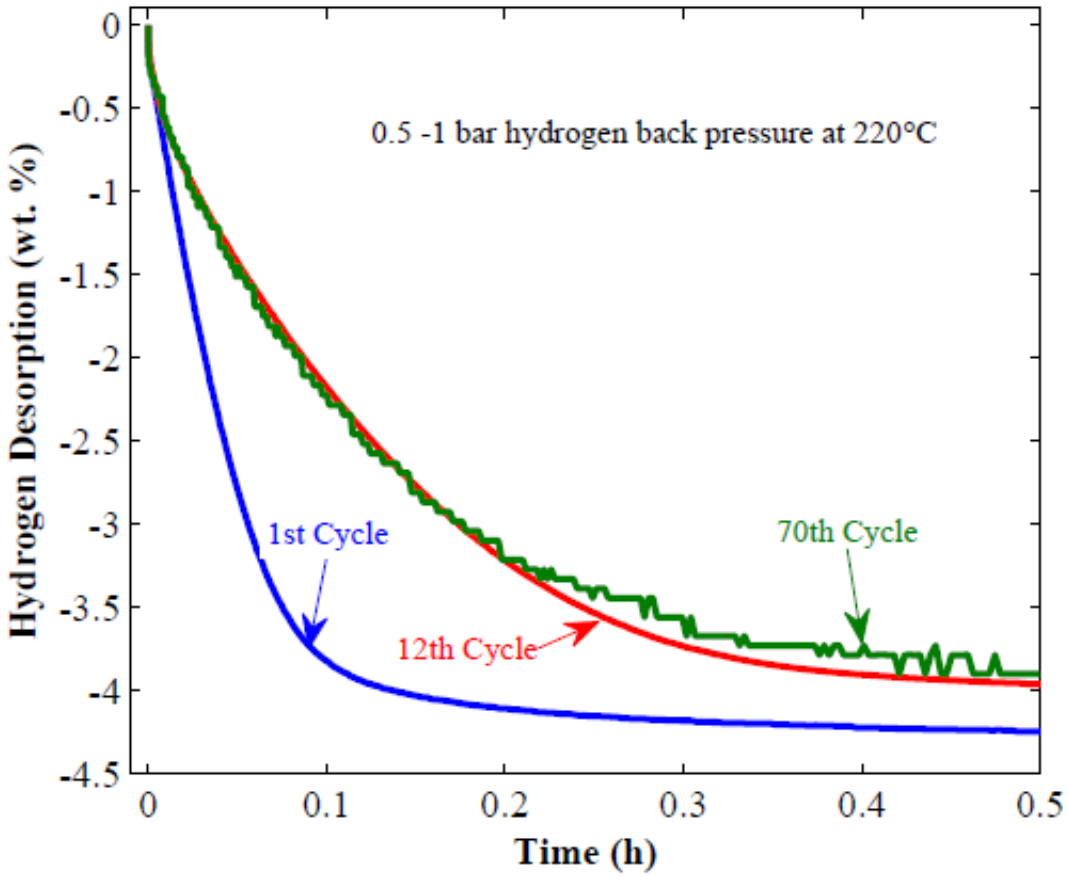

Figure 4.5. Desorption kinetics cycle comparison of S#3. The fluctuations in 70th cycle (green curve) are due to using high pressure transducer in data collection as compared to 1st and 12th cycles where low pressure transducer was used.

The results presented in Figure 4.6 indicate that Li-Mg-N-H system always releases small amounts of NH_3 for a wide range of preparation conditions (see Table 4.1). The ratio of NH_3 to H_2 is further qualitatively determined from the areas under the curves of the NH_3 and H_2 mass spectrometry signals (see Table 4.2). The samples with the slowest kinetics (i.e., S#5, S#6 and S#7) have the highest NH_3 emission as well, showing the importance of selecting proper ball milling parameters to limit the NH_3 emission in the Li-Mg-N-H system. Furthermore, the sample S#6 showed a significant NH_3 emission indicating that the ball to powder ratio of 20:1 is not effective in making intimate contacts between the starting materials.

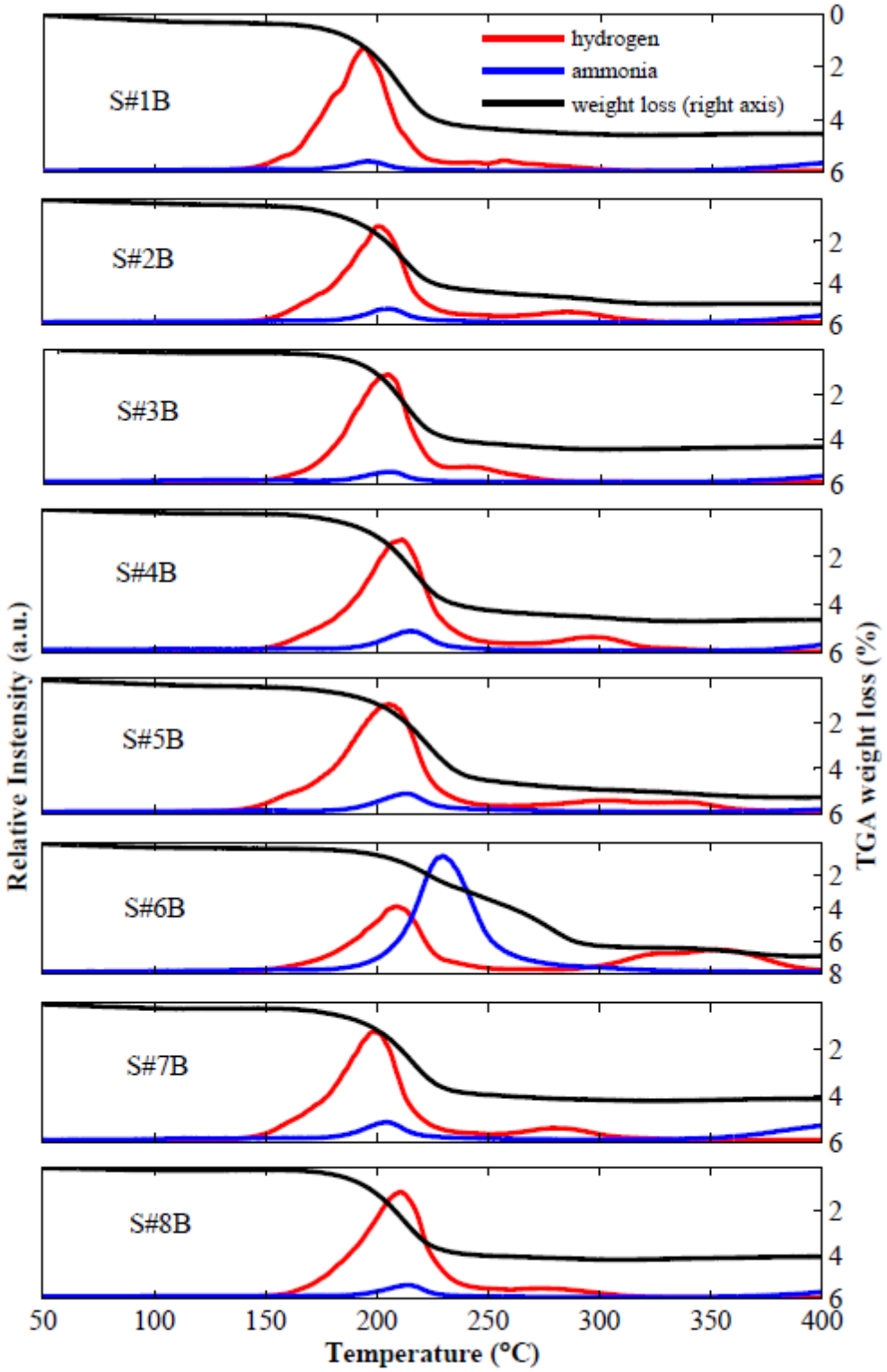

Figure 4.6. Hydrogen and NH_3 signals from the mass spectrometry, and the associated thermogravimetric (under 100 ml nitrogen and 5 K/min heating rate) weight loss of S#1B-8B. NH_3 signal is multiplied by 10 for visibility.

The reason underlying the high level of NH_3 emission from the sample S#6 is the decomposition of $LiNH_2$ (i.e., $2LiNH_2 \rightarrow Li_2NH + NH_3$) during desorption [246]. In other words, the insufficient ball milling of S#6 led to incomplete metathesis conversion (Eq. 4.4), and thus the decomposition of $LiNH_2$ during desorption. In fact, the XRD peaks of Li_2NH compound at 30.6 and 35.6 2θ degrees are clearly visible from the XRD spectrum of S#6 given in Figure 4.2. One of the best performing samples, S#3, is selected to further investigate the effects of SWCNT and SWCNT-20Ru doping on the kinetics and NH_3 emission characteristics of the Li-Mg-N-H system.

4.3.2. SWCNT and SWCNT-20Ru Doped Li-Mg-N-H System

SWCNT and SWCNT-20Ru were extensively characterized to better understand their effects as a catalyst in the Li-Mg-N-H system. Nitrogen ad/desorption isotherms and the pore size distributions of the SWCNT, SWCNT-Ox and SWCNT-20Ru are given in Figure 4.7 (A) and (B), respectively. All isotherms are of type IV according to the International Union of Pure and Applied Chemistry (IUPAC) classification [80] which is a characteristic of a mesoporous material. However, according to the manufacturer's data sheet, TEM measurements and the pore size distribution, SWCNTs are microporous with a diameter of 1 – 2 nm. The hysteresis in the high relative pressure (i.e., 0.5 – 1 P/P_o) is associated with the intertubular space [252] which is an indication of the SWCNT bundles. Therefore, mesoporosity of the SWCNTs is related to the bundles, not the pore sizes of SWCNTs. In addition, as-received SWCNTs have a surface area of 816 m^2/g which is close to the theoretical upper limit of 1315 m^2/g, and the difference between the theoretical upper limit and the actual surface area values is an additional indication of the SWCNT bundles [253]. Upon 2.6 M nitric acid oxidation treatment and Ru doping, the

surface area of the SWCNTs was gradually decreased and the hysteresis loop attenuated. Attenuation of the hysteresis loop is due to the disintegration of the SWCNTs bundles. Indeed, the pore size distribution of the SWCNT-Ox and SWCNT-20Ru became narrower (i.e, 1 – 6 nm) as compared to the as-received SWCNTs (i.e., 1 – 18 nm).

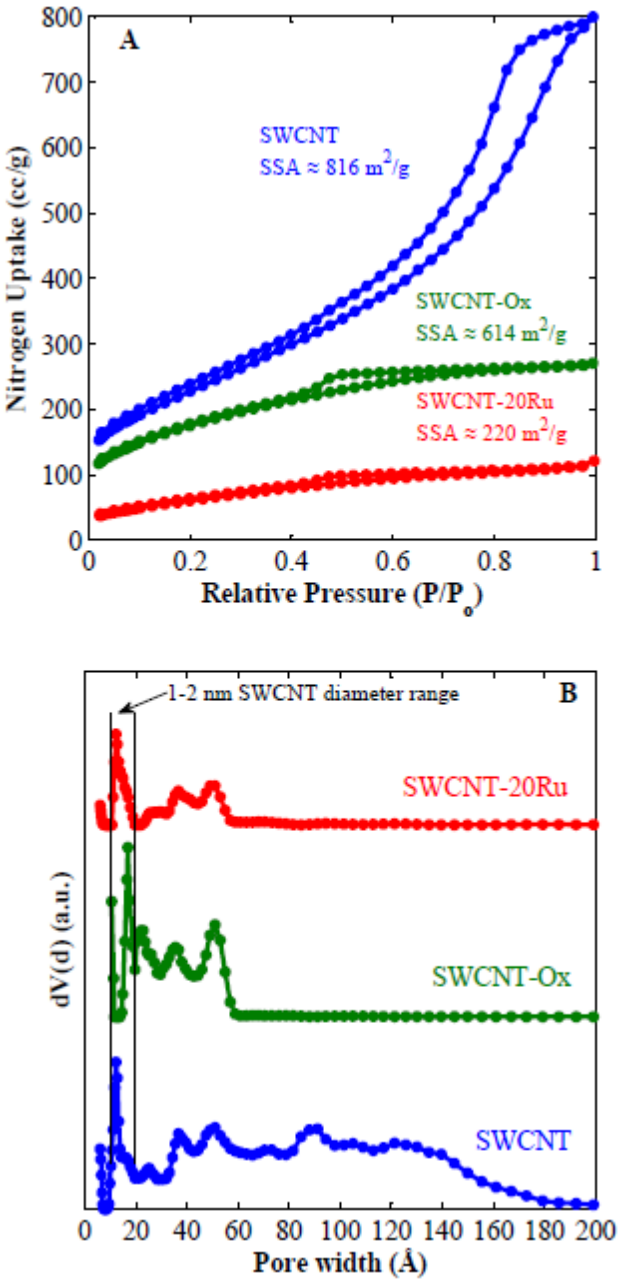

Figure 4.7. (A) Nitrogen adsorption isotherms and (B) the pore size distributions of SWCNT, SWCNT-Ox and SWCNT-20Ru.

Moreover, the SEM images given in Figure 4.8 show reduced bundling after the oxidation treatment and Ru doping. On the other hand, the surface area decrease in the SWCNT-Ox and SWCNT-20Ru must be related to the oxygen functionalities attached to the SWCNTs and the pore blocking due to Ru doping, respectively [203].

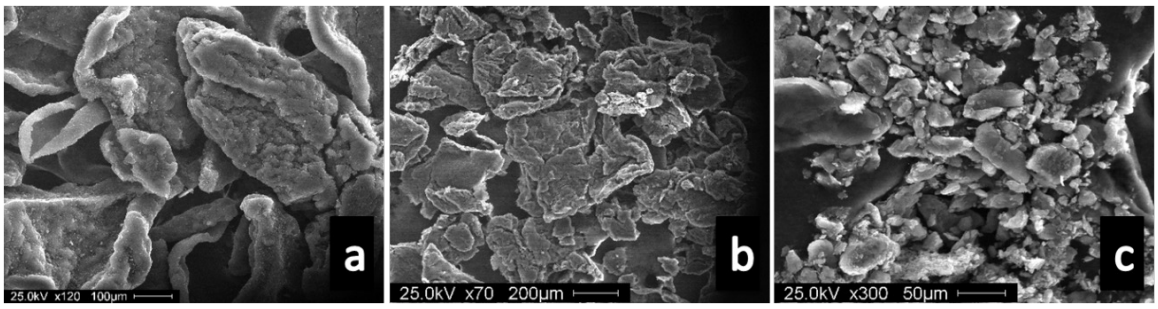

Figure 4.8. SEM images of (a) SWCNT, (b) SWCNT-Ox and (c) SWCNT-20Ru.

Chemical composition and the Ru loading were determined by incorporating EDX and TGA as given in Figure 4.9 and Figure 4.10, respectively. The oxygen content in the as-received SWCNTs is 5 wt. %. After the oxidation treatment in 2.6 M nitric acid, the oxygen content increased to 15 wt. % and did not change considerably upon Ru doping. The nominal Ru loading in the SWCNT-20 is 20 wt. %. However, the EDX analysis showed ≈ 17 wt. % of Ru loading on average. On the other hand, TGA showed ≈ 20 wt. % of Ru loading. The difference between the TGA and EDX analyses might be related to Ru oxidation or oxygen dissolution in the Ru matrix at high temperatures [254,255]. In any case, it is clear that one can safely assume that the actual Ru loading is very close to the nominal loading of 20 wt. %, and is in the range of 17 – 20 wt. %. Furthermore, the source and the content of the impurities in the SWCNTs were determined by EDX and TGA. According to the EDX and TGA measurements, the only impurity is 1 – 2 wt. % Fe (the Fe peak is not shown in EDX spectra for brevity).

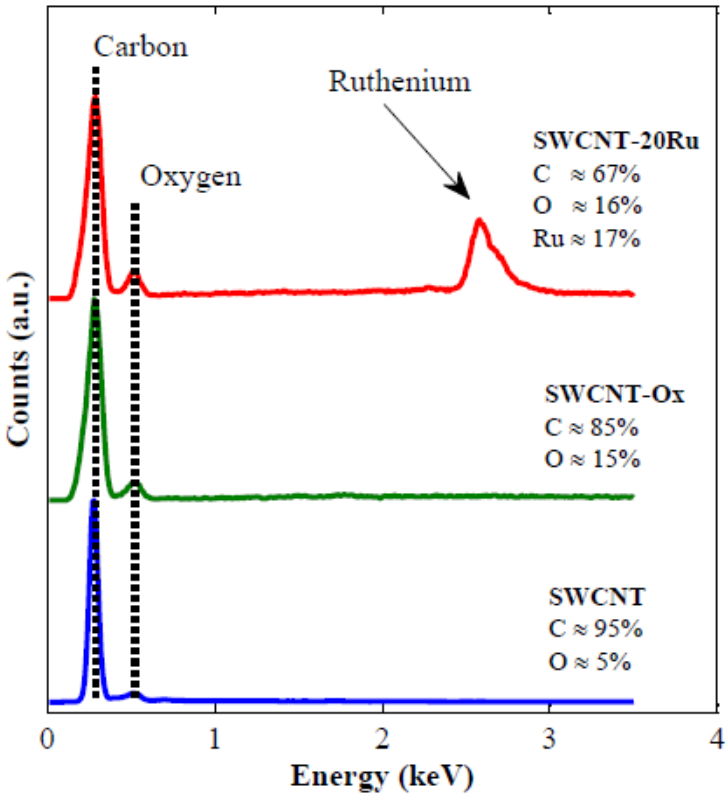

Figure 4.9. EDX spectra of SWCNT, SWCNT-Ox and SWCNT-20Ru. Composition of the elements are given in weight percentage.

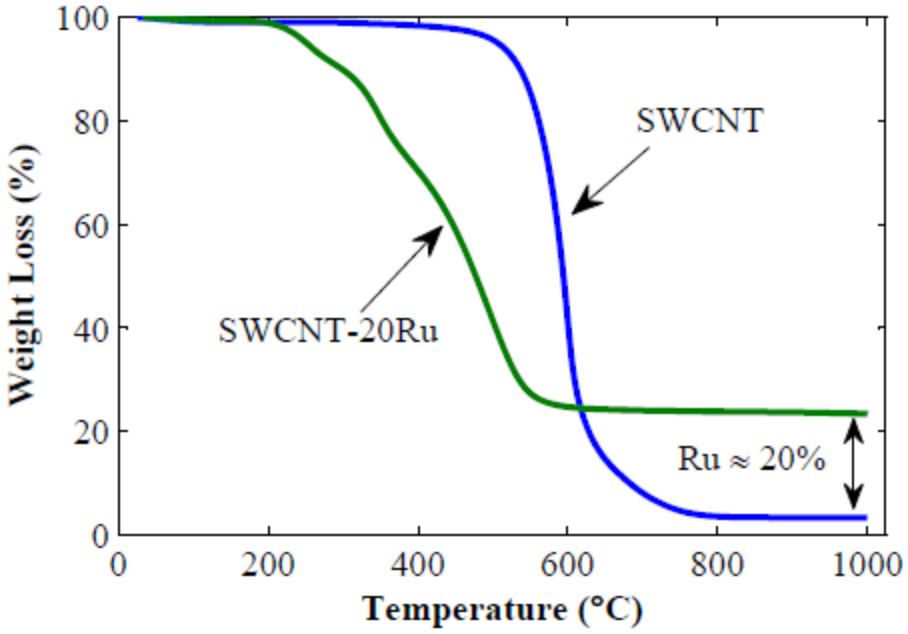

Figure 4.10. TGA weight losses of SWCNT and SWCNT-20Ru. TGA data collected under 100 ml/min air flow at 10 K/min heating rate.

Ru particle size is known to be an important factor in the NH_3 decomposition [256]; however, to date, it has not been studied for Ru doped SWCNTs. Ru particle size can be determined by using the Scherrer's equation from the XRD patterns given in Figure 4.11. However, as-received SWCNTs showed graphite peaks at 24.4 (d_{002}) and 44.6 (d_{101}) 2θ degrees due to bundling of SWCNTs [257]. Since the most intense Ru peak at 44.1 (d_{101}) 2θ degrees overlaps with the graphite peak at 44.6 2θ degrees, it was not possible to determine the particle size reliably using XRD.

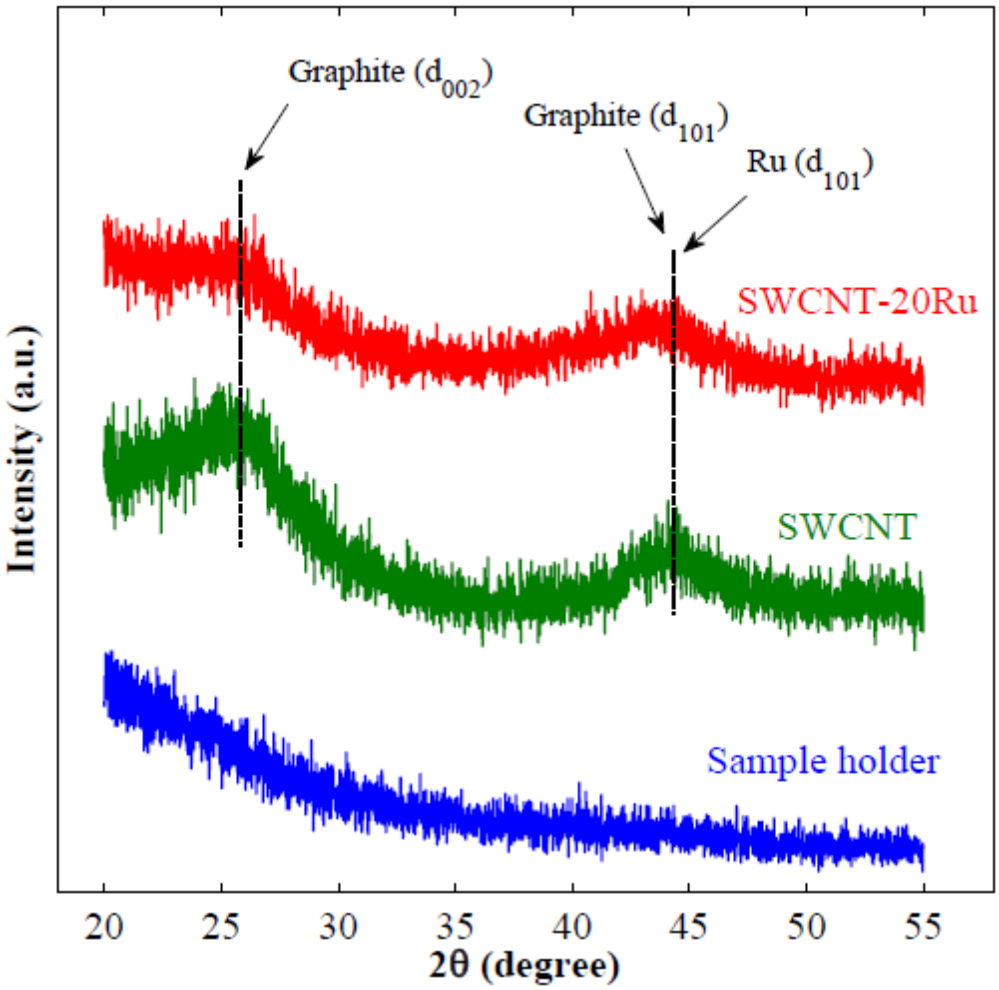

Figure 4.11. XRD patterns of SWCNT and SWCNT-20Ru.

Therefore, Ru particle size was measured by TEM as shown in Figure 4.12. From the TEM images, several different Ru particles were measured, and the average Ru particle size was found to be ≈ 2 nm.

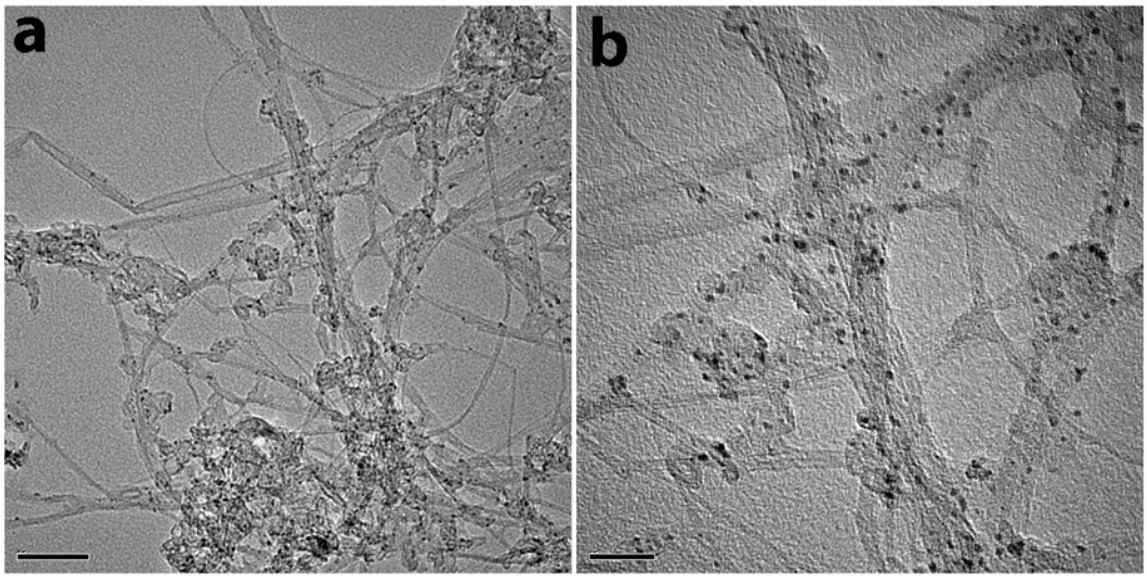

Figure 4.12. TEM images of SWCNT-20Ru. Scale bars correspond to (a) 50 nm and (b) 20 nm.

In addition, TEM images unambiguously showed SWCNT bundles and a small amount of amorphous carbon. More importantly, Ru particles mostly deposited on the exterior and not the interior walls of the SWCNTs. Nevertheless, it was not possible to determine the structural defects on the walls of the SWCNTs due the low contrast at high magnifications.

An important parameter that needs to be tailored is the structural defects introduced in the SWCNTs to make them effective as a catalyst in the Li-Mg-N-H system. As mentioned in the Introduction, structural defects are required to facilitate the diffusion of Li ions into and out of the SWCNTs. Since SWCNT and SWCNT-20Ru were mixed with the S#3 sample via ball milling, the surface area change due to ball

milling duration was investigated first to decide the optimum ball milling duration for introducing the catalysts. Significant number of studies available in the literature discuss the effects of ball milling on SWCNTs alone [257-259]; however, it was shown that CNTs ball milled within the presence of another powder can dramatically change its structure, as compared to ball milling CNTs alone for the same duration, since the presence of another powder can act as a very small size milling balls [260]. It is reasonable to assume that the surface area change is directly related to the SWCNT structure. In other words, if SWCNTs survive the ball milling process, the surface area of the catalyst mixed base material should be higher than the base material since the SWCNT-20Ru has 20 fold more surface area than the base material S#3. Figure 4.13 shows the change in the surface area of the S#3-5SWCNT (i.e., 5 wt. % as-received SWCNTs doped S#3) as a function of the ball milling duration. At the start of the ball milling, S#3-5SWCNT has a surface area of 52.2 m^2/g (see Figure 4.13 for details). After ball milling S#3-5SWCNT for 15 min, the surface area decreased to 40 m^2/g, and the extended ball milling gradually resulted in a lower surface area. At the end of 300 min of ball milling, the surface area of the S#3-5SWCNT returned to the original surface area of the starting material which shows that the majority of the SWCNT did not survive such a long ball milling process.

The optimal ball milling duration should be long enough to ensure homogenous dispersion of the SWCNTs and to introduce structural defects, but should not be very long to make sure that the majority of the SWCNTs are still present (i.e., not converted to amorphous carbon or graphite) after ball milling. Therefore, ball milling duration of 60 min was selected due to S#3-5SWCNT's moderate surface area. This decision was

further validated via Raman spectroscopy which is a powerful tool for studying the structural characteristics of CNTs [261].

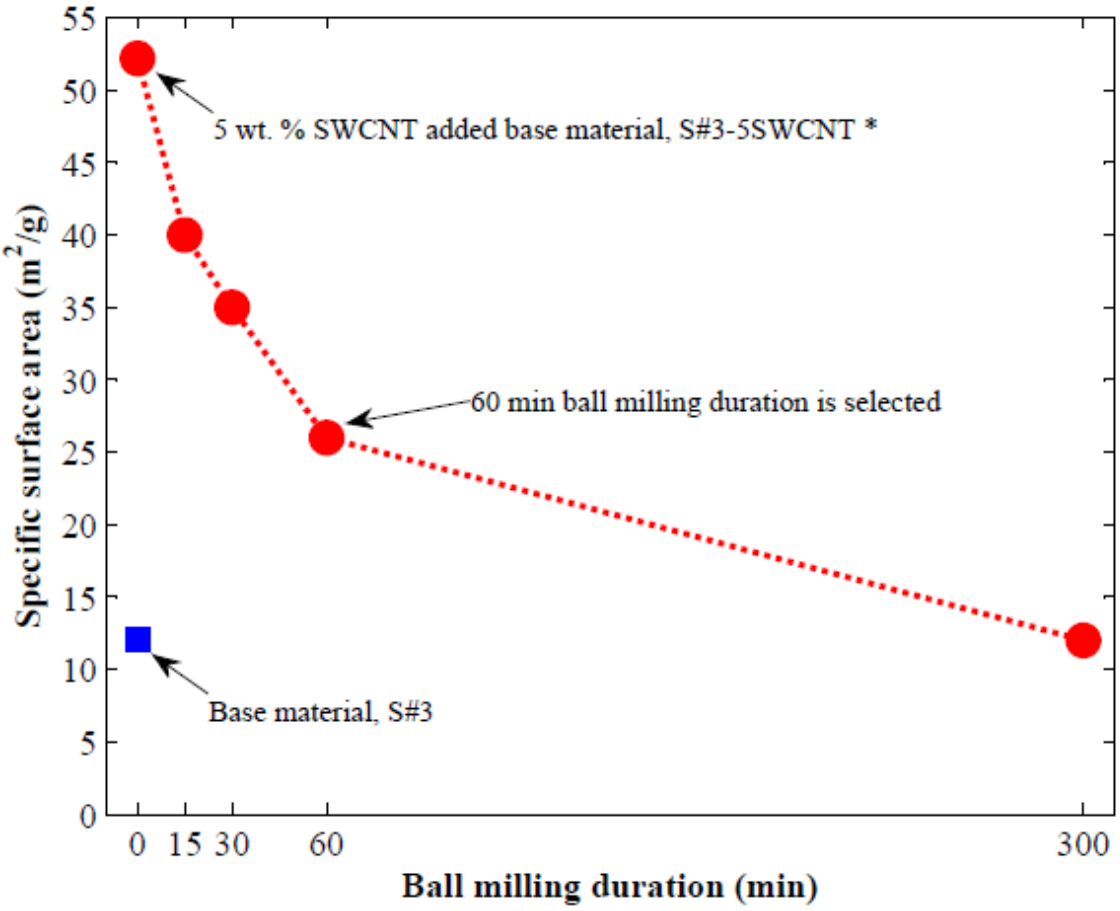

Figure 4.13. The change in surface area of the S#3-5SWCNT as a function of ball milling duration. * The specific surface area of S#3-5SWCNT at the start of the ball milling is estimated by weighted average method. The weight ratio of the base material to SWCNTs in S#3-5SWCNT is 19 (i.e. 95% S#3 and 5% SWCNTs by weight). The specific surface areas of S#3 and SWCNTs are 12 m^2/g and 816 m^2/g, respectively. Therefore, $SSA_{S\#3\text{-}5SWCNT} = 0.95 \times 12\ m^2/g + 0.05 \times 816\ m^2/g = 52.2\ m^2/g$.

Figure 4.14 shows the Raman spectra of the as-received SWCNTs, S#3-5SWCNT and S#3-5SWCNT-20Ru (i.e., 5 wt. % SWCNT-20Ru doped S#3). The peaks at 1317 cm^{-1} and 1585 cm^{-1} are the characteristic D (disorder mode) and G (tangential mode) bands of the SWCNTs, respectively. The full width at half maximum (FWHM) value of D band can be used to indicate the presence of non-SWCNT carbonaceous impurities; in

addition, the intensity ratio of D band to G band (I_D/I_G) is related to the defects introduced into the SWCNTs [148]. Table 4.3 shows the mean values of I_D/I_G and the FWHM of the D band.

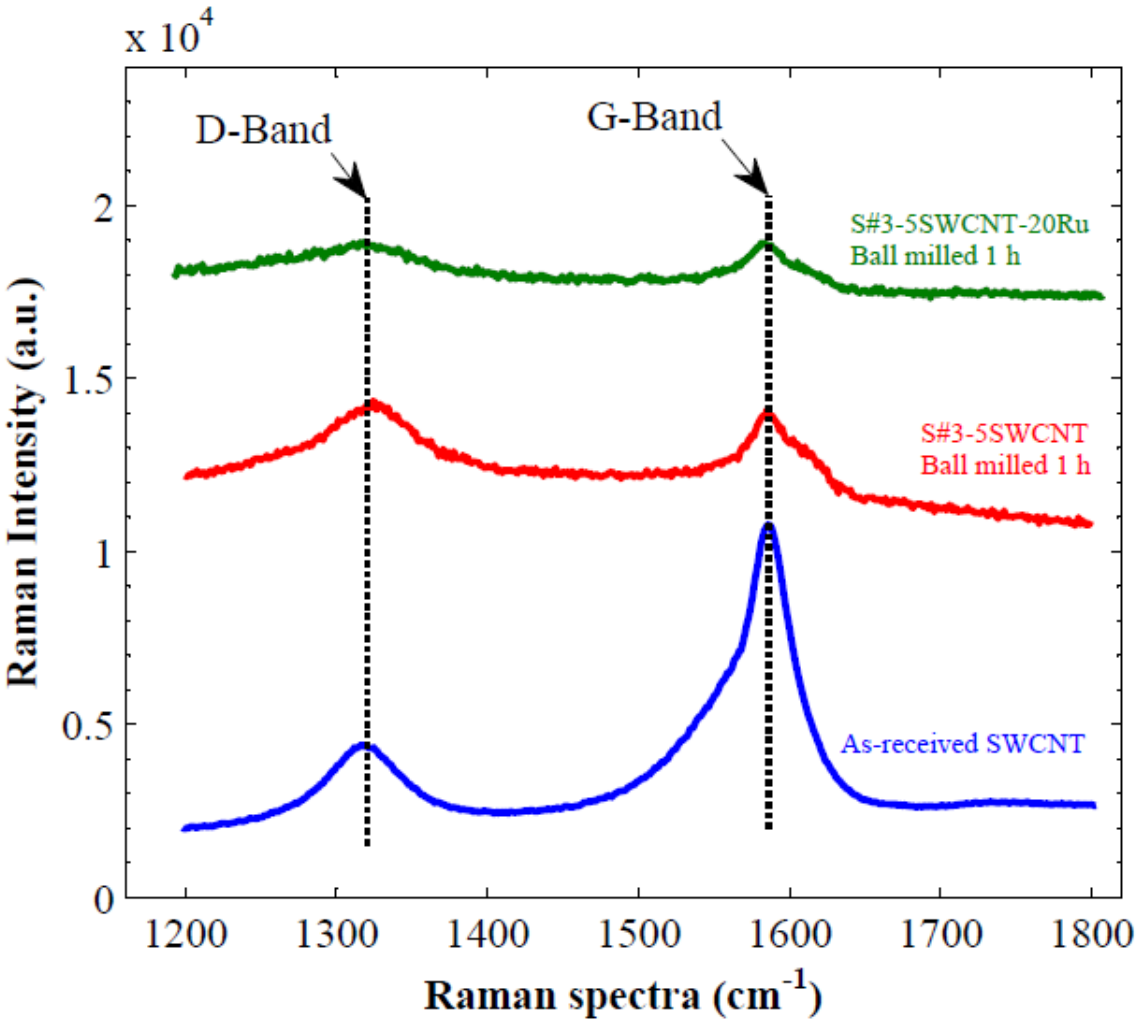

Figure 4.14. Raman spectra of as-received SWCNT, S#3-5SWCNT and S#3-5SWCNT-20Ru.

Upon ball milling of SWCNTs and SWCNT-20Ru with S#3, the value of I_D/I_G increased more than three times from 0.26 for the as-received SWCNTs to 0.87 and 0.81 for S#3-5SWCNT and S#3-5SWCNT-20Ru, respectively, which indicates that structural defects were successfully introduced after 60 min of ball milling. Moreover, the D band

is narrower in the starting material (FWHM ≈ 52cm^{-1}) as compared to S#3-5SWCNT (FWHM ≈ 65cm^{-1}) and S#3-5SWCNT-20Ru (FWHM ≈ 127 cm^{-1}). This further supports the previous conclusion that amorphous and nano-crystalline carbon were introduced during the ball milling process due to the decomposition of the SWCNTs, which were also observed in the TEM images given in Figure 4.12.

Table 4.3. FWHM values and the intensity ratios of the D to G band of the as-received SWCNTs, S#3-5SWCNT and S#3-5SWCNT-20Ru.

	As-received SWCNTs	**S#3-5SWCNT**	**S#3-5SWCNT-20Ru**
FWHM (cm^{-1})	52	65	127
I_D / I_G	0.26	0.87	0.81

One interesting observation is that the FWHM of the D band for the S#3-5SWCNT-20Ru is almost double that of S#3-5SWCNT. This broadness most likely originates from the Ru doping steps in preparation of the SWCNT-20Ru catalyst. In addition, a closer look into the G band, given in Figure 4.14, shows that the frequency of G band downshifts by 3 cm^{-1} after Ru doping into the SWCNTs. It has been reported that doping with either electron donors or acceptors can change the shape and energy of some of the vibrational modes of SWCNTs [262]. The red shift of G band suggests that there is charge transfer from Ru to the SWCNTs. The higher electron density in the reduced SWCNTs results in weaker net bonding thus lowering the G band frequency.

The ab/desorption kinetics of the samples S#3, S#3-5SWCNT and S#3-5SWCNT-20Ru at 200°C and 220°C are given in Figure 4.15. Contrary to the previous study [238], no enhancements in the ab/desorption kinetics were observed for the S#3-5SWCNT as compared to the base sample S#3. On the other hand, the S#3-5SWCNT-20Ru performed similarly to the S#3 in ab/desorption kinetics. The ultimate ab/desorption capacity of the

S#3-5SWCNT-20Ru is slightly lower than the S#3 because of the dead weight of the SWCNT-20Ru catalyst.

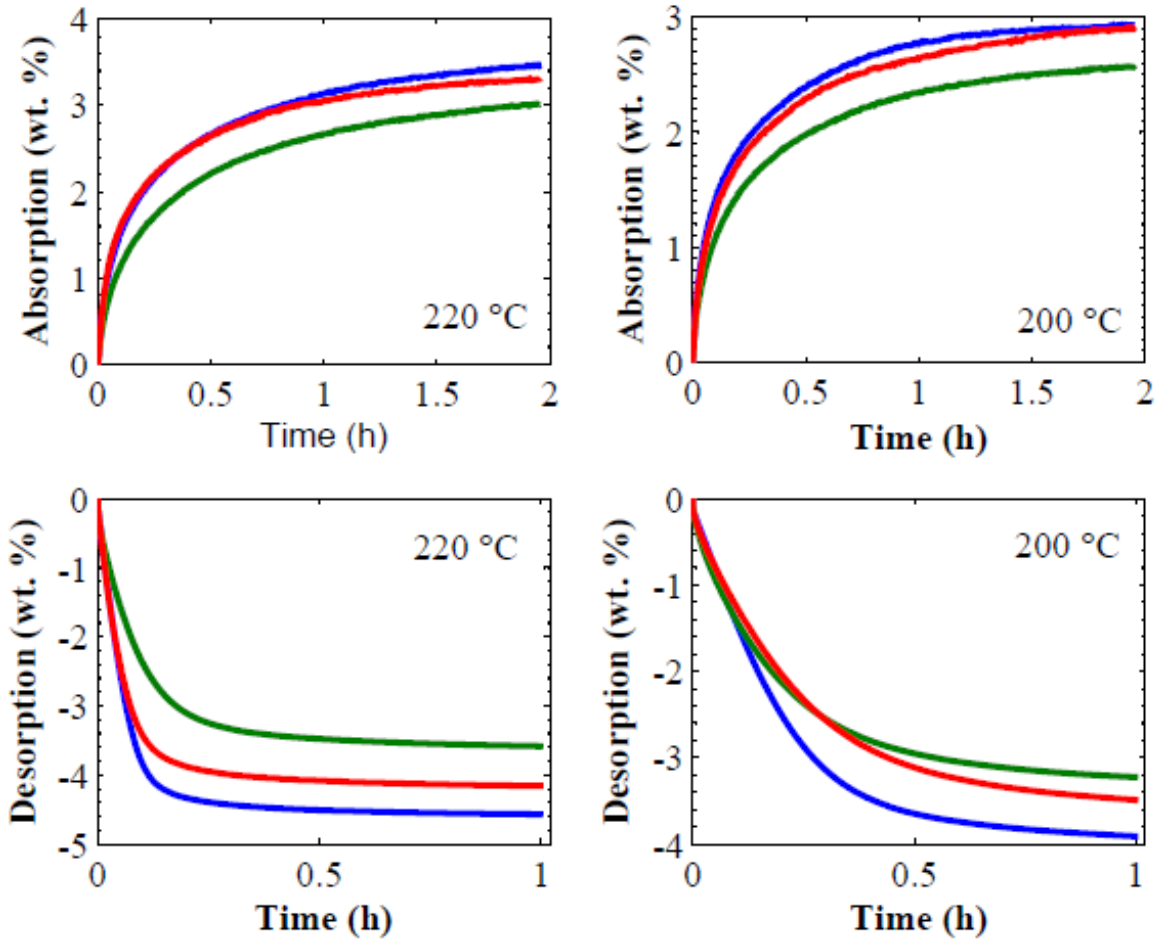

Figure 4.15. Absorption and desorption kinetics of S#3 (blue), S#3-5SWCNT (green) and S#3-5SWCNT-20Ru (red) at 200°C and 220°C. Absorption and desorption kinetics data collected at ≈ 90 bar and ≈ 0.5 – 1 bar, respectively.

One of the reasons behind the degraded kinetics performance of S#3-5SWCNT as compared to S#3-5SWCNT-20Ru might be related to the lower defect density of the S#3-5SWCNT (see Table 4.3). Although both S#3-5SWCNT and S#3-5SWCNT-20Ru samples are subjected to the same ball milling procedure to disperse the catalysts, SWCNT-20Ru catalyst includes more structural defects (i.e., due to additional steps involved in Ru doping of SWCNTs) than the SWCNTs catalyst as discussed previously.

In other words, selecting a ball milling duration longer than 1 h can enhance the kinetics performance of S#3-5SWCNT and S#3-5SWCNT-20Ru by introducing more defects. However, further work is required to reveal the role of structural defects in SWCNTs on kinetics enhancement in the Li-Mg-N-H system.

One of the main goals of this work is to study the effects of Ru doped SWCNTs in suppressing the NH_3 emission. The NH_3, hydrogen and nitrogen mass spectrometry signals for the S#3, S#3-5SWCNT and S#3-5SWCNT-20Ru are given in Figure 4.16. The NH_3 concentration was determined qualitatively, and the results are given in Table 4.4. Both S#3-5SWCNT and S#3-5SWCNT-20Ru resulted in higher NH_3 release as compared to the base sample S#3. The primary role of CNTs in hydride systems is claimed to be that of providing diffusion channels for hydrogen [237]. If this is correct, the reason responsible for the increased NH_3 emission for the SWCNTs and SWCNT-20Ru doped samples can be explained in a similar way since SWCNTs can also act as diffusion channels for NH_3 as well. More importantly, SWCNT-20Ru is shown to be an effective catalyst in the NH_3 decomposition for the Li-Mg-N-H system.

Table 4.4. NH_3 to hydrogen signal ratios of S#3, S#3-5SWCNT and S#3-5SWCNT-20Ru.

	S#3	**S#3-5SWCNT**	**S#3-5SWCNT-20Ru**
Area Under Curve § NH_3 / H_2 (%)	0.46	1.82	0.82

§ Refer to Table 4.2 for the calculation details.

The rectangular region two, shown in Figure 4.16, clearly demonstrates the difference between S#3, S#3-5SWCNT and S#3-5SWCNT-20Ru. For S#3 and S#3-5SWCNT, NH_3 signals start to increase after 350°C, whereas for S#3-5SWCNT-20Ru

the NH_3 signal continues to be at the background level, and the hydrogen and nitrogen signals start to increase due to the NH_3 decomposition.

As seen in Figure 4.16, no sign of NH_3 decomposition is evident around the main peak of interest at 220°C from the hydrogen signal since the hydrogen signal is very high in intensity compared to the NH_3 signal; hence, NH_3 decomposition is not noticeable from the change in hydrogen intensity around 220°C. Therefore, the nitrogen signal was investigated to determine if any NH_3 decomposition occurs around 220°C.

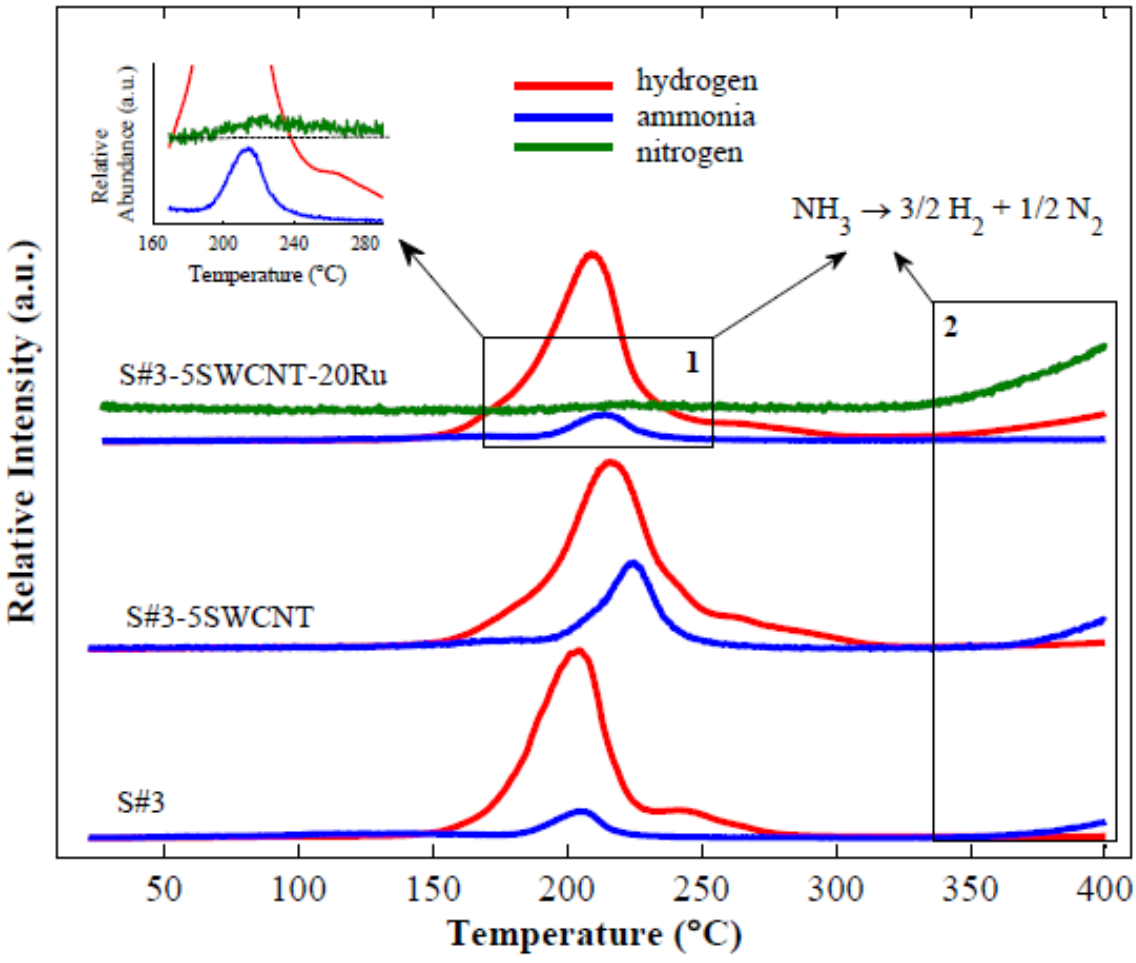

Figure 4.16. Hydrogen, NH_3 and nitrogen mass spectrometry signals of S#3, S#3-5SWCNT and S#3-5SWCNT-20Ru. NH_3 and nitrogen signals are multiplied by 15 for visibility. Nitrogen signal from S#3-5SWCNT-20Ru shifted upwards to make comparison with the NH_3 and hydrogen signals easier. The dashed line in the inset figure shows the background nitrogen level.

Since the nitrogen signal is at the background level from the beginning of the experiment, any NH_3 decomposition should be noticeable immediately in the nitrogen signal. Indeed, a closer look into the nitrogen signal around the main NH_3 peak of interest (i.e., region one and the inset in Figure 4.16) which is around 220°C shows a slight increase in the nitrogen intensity in phase with the NH_3 signal increase. However, the SWCNT-20Ru is not that effective at 220°C as compared to its activity beyond 350°C; therefore, one can conclude, the NH_3 signal did not drop to the background level at 220°C.

4.4. Conclusions

The $LiNH_2 – MgH_2$ (2:1.1) complex hydride system was investigated in terms of its kinetics and NH_3 emission characteristics. The Li-Mg-N-H system prepared with different ball milling parameters showed that NH_3 emission and kinetics are closely related to the crystallite size. Samples with a smaller average crystallite size performed better in terms of both kinetics and NH_3 emission. However, it is not possible to eliminate NH_3 emission just by optimizing the ball milling parameters. To suppress the NH_3 and to enhance the kinetics, SWCNT and Ru doped SWCNT (i.e., SWCNT-20Ru) catalysts were investigated. The SWCNT doped base sample showed a degraded performance in terms absorption kinetics; however, the SWCNT-20Ru doped sample performed similarly to the base sample. Results indicate that structural defects in SWCNTs play an important role in kinetics enhancement. More importantly, it was shown that the SWCNT doping results in higher NH_3 emission in the Li-Mg-N-H system. On the other hand, the SWCNT-20Ru doped sample effectively suppressed the NH_3 emission by decomposition compared to the SWCNT doped sample. Further work is necessary to design the optimal

catalyst for the Li-Mg-N-H system. For instance, the effects of Ru particle size in SWCNTs need to be studied in detail to elucidate how the Ru particle size affects the NH_3 decomposition reaction. In this study, Ru particles in the SWCNT-20Ru catalyst were mostly deposited on the exterior walls of the SWCNTs. Ru particles inside the SWCNTs may enhance the NH_3 decomposition reaction. Finally, better ways of introducing structural defects in SWCNTs and to homogeneously disperse the SWCNTs in the base sample, other than the ball milling process, need to be explored.

Chapter 5. Volumetric Hydrogen Sorption Measurements – Uncertainty Error Analysis and the Importance of Thermal Equilibration Time[9,10]

5.1. Introduction

The errors in hydrogen sorption measurements are of major concern in the hydrogen storage community which impede the down selection process of candidate materials and set back progress in the field. Hydrogen storage measurements are prone to various sources of errors since there are only a few methods available to detect the hydrogen absorption and desorption directly[11] (i.e., thermal desorption mass spectroscopy [177,263] and neutron scattering [172]), and these methods either require sophisticated and expensive tools or can only be utilized for specific types of materials under certain conditions (i.e., cryogenic temperatures, ultra high vacuum, etc.). Therefore, the vast majority of the hydrogen storage measurements reported in the literature make use of indirect methods by utilizing volumetric (Sievert's type) and/or gravimetric apparatuses since these techniques are much more affordable, easier to fabricate and operate, and better suited to the rapid screening of samples.

---

[9] The work presented in this chapter has been previously published (DE Demirocak, SS Srinivasan, MK Ram, DY Goswami, EK Stefanakos, Volumetric Hydrogen Sorption Measurements − Uncertainty Error Analysis and the Importance of Thermal Equilibration Time, International Journal of Hydrogen Energy, 2012, 38(3), p. 1469–77). See Appendix C for copyright information.

[10] Refer to the nomenclature (section 5.5) for all the symbols used throughout the chapter 5.

[11] "Directly" refers to the determination of the gas species unambiguously using spectroscopic tools as opposed to "indirectly" where the quantity of the absorbed or desorbed hydrogen is calculated from pressure and temperature measurements using a real gas equation of state (i.e., volumetric apparatus) or weight change using a high sensitivity balance (i.e., gravimetric apparatus) assuming all the absorbed or desorbed species are hydrogen.

The measurement errors are especially problematic and harder to realize for the materials that are based on physisorption, since the theoretical upper limit is not known unambiguously as compared to complex metal hydrides. In addition, for such materials, the storage capacity is typically low (i.e., less than 1 wt. %, which is about an order of magnitude less than that of well known hydrides such as MgH_2 and $LiNH_2$–MgH_2) at room temperature and high pressure (i.e., 298 K and 10 MPa). Physisorption based materials can adsorb significant amount of hydrogen at 77 K and high pressure [264]; however, the most erroneous measurements reported in the literature are performed at room temperature and high pressure where their capacity is typically less than 1 wt. %. In other words, for any material, the hydrogen sorption measurements are most cumbersome at a point (i.e., at a specific P and T) where the sample's hydrogen storage capacity is the lowest.

The repeatability of the unusually promising results (i.e., carbon structures [265], polyaniline [266,267] and spillover enhancement [102,178]) has been a major issue in the hydrogen storage literature. Most of the time, it is not possible to determine if the non-repeatability of the results is associated with the materials' preparation or purely a measurement error or both. On the other hand, the Round Robin test conducted by 14 different laboratories to evaluate the hydrogen storage capacity of a commercial activated carbon clearly demonstrated the significance of the measurement errors even though the same sample (i.e., supplied from the same source) was tested in all the laboratories [127].

Fortunately, significant experience on the sources of the measurement errors has been accumulated during the last decade [126,268,269]. The sample cell physisorption and small sample loadings [201,270], uncertainty in the sample's density [271], the

optimum sample loading depending on the sample's intrinsic storage capacity [272], comparison of the gravimetric and volumetric techniques [273] and the uncertainty in the measurements [272-274] were investigated thoroughly. However, there is still a lack of quantitative data on some aspects of the measurement errors and the uncertainty in the measurements in relation to the design of a volumetric apparatus.

There are two goals in this work. First, the design of a volumetric apparatus is investigated by an uncertainty analysis [275] to determine the uncertainties in the high pressure hydrogen sorption measurements. Guidelines are presented on the selection of the reservoir and sample cell volumes to minimize the uncertainty in the measurements. In addition, the effect of the sample mass loading on the measurement uncertainty is studied based on the sample's estimated hydrogen storage capacity and the design of a volumetric apparatus. Secondly, the effect of the thermal equilibration time (i.e., the time required for thermal equilibrium when hydrogen gas is admitted into a reservoir volume at a temperature different than that of the instrument enclosure temperature, and when there is a temperature gradient within the instrument enclosure) on the accuracy of the measurements is investigated.

5.2. Methods

5.2.1. Operating Principle of a Volumetric Apparatus

In a volumetric apparatus, the hydrogen uptake of a material is calculated by using an appropriate real gas equation of state from measurements of the pressure drop in a volume calibrated reservoir and sample cell, the temperature of the reservoir and sample cell volumes, and the density of the material which is usually determined by a helium expansion test. The schematic of a volumetric apparatus is shown in Figure 5.1.

The operation of a volumetric apparatus is as follows: initially the isolation valve is closed and hydrogen is fed into the reservoir volume. After the system reaches thermal equilibrium, the pressure and temperature of the hydrogen are recorded, and then the isolation valve is opened. After the pressure change in the system levels off, the pressure and temperature of the hydrogen in the system are recorded again.

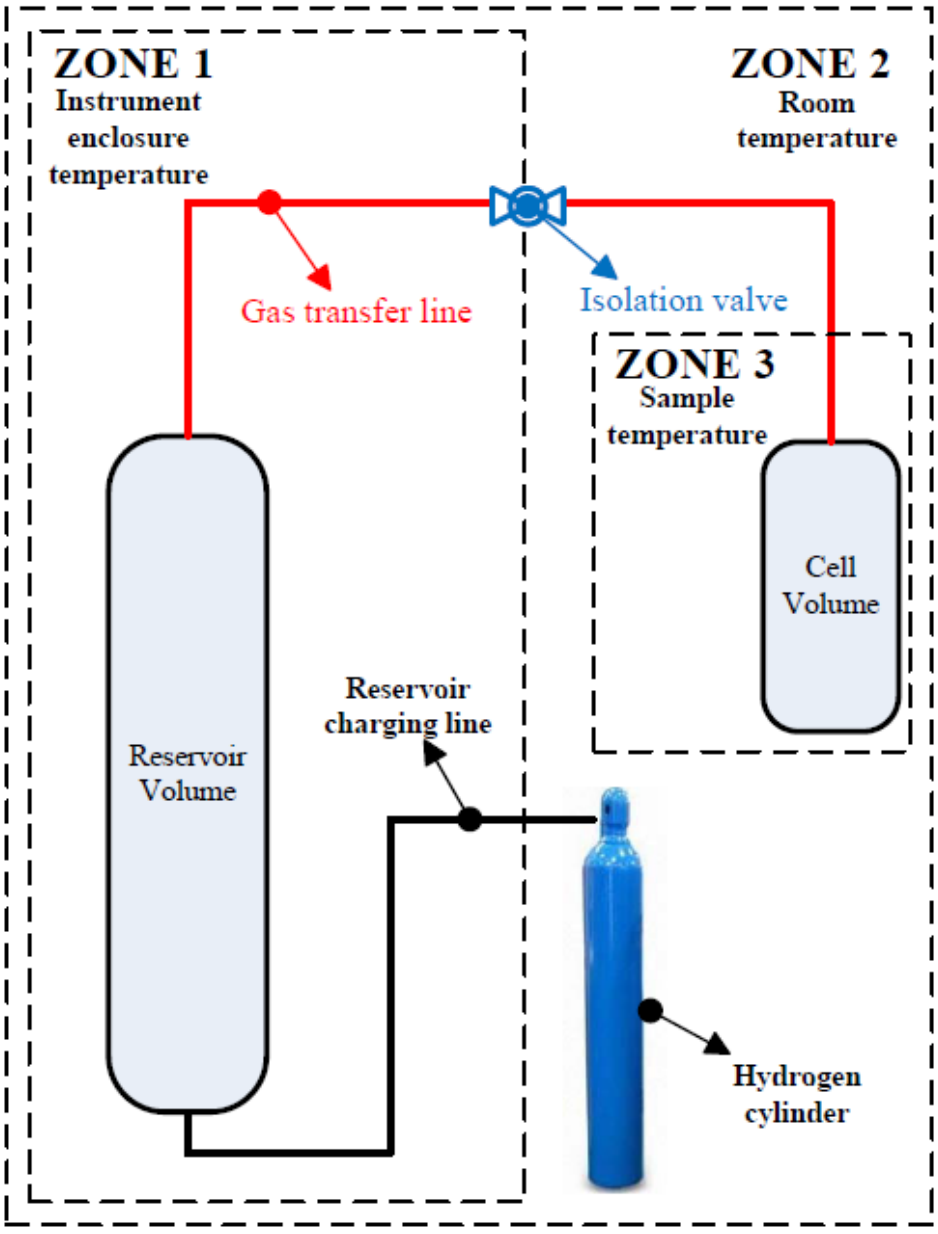

Figure 5.1. Schematic of a volumetric apparatus.

Then the sample's hydrogen uptake can be calculated by subtracting the initial hydrogen content in the reservoir from the final hydrogen content in the system. Therefore, the hydrogen uptake of a sample can be expressed as,

$$\Delta n_{H_2} = n_i - n_f \tag{5.1}$$

By using a real gas equation of state, the quantity of hydrogen at the start and the end of the measurements can be determined as follows,

$$n = \frac{P \cdot V}{Z \cdot R \cdot T} \tag{5.2}$$

By substituting Eq. (5.2) into Eq. (5.1), and by assuming $T_{Zone1} = T_{Zone2} = T_{Zone3} = T$ in Figure 5.1, the total hydrogen uptake of a sample can be calculated as given in Eq. (5.3).

$$\Delta n_{H_2} = \frac{P_{res} \cdot V_{res}}{Z(P_{res}, T) \cdot R \cdot T} - \frac{P_{sys} \cdot V_{sys}}{Z(P_{sys}, T) \cdot R \cdot T} \tag{5.3}$$

where V_{res} represents the combined reservoir volume and tubing volume (i.e., the volume in between the reservoir volume and the isolation valve) in Zone 1 (see Figure 5.1). V_{sys} is the total system volume (i.e., the combined reservoir, cell and tubing volumes shown in Figure 5.1) minus the volume occupied by a sample. Therefore, the system volume can be expressed by Eq. (5.4), as

$$V_{sys} = V_{res} + V_{dead} \tag{5.4}$$

where the dead volume (V_{dead}) is the cell volume plus the tubing volume in Zones 2 and 3 combined minus the volume occupied by a sample. The dead volume can be determined directly using helium expansion from the reservoir volume (i.e., the reservoir volume is charged with helium initially, and the temperature and pressure readings are recorded. After opening the isolation valve, the temperature and pressure readings are recorded again. Finally, assuming there is no helium adsorption in the sample, the dead volume

can be calculated using a helium real gas equation of state) or by determining the sample's density from the helium pycnometry and use of Eq. (5.5) (i.e., cell and tubing volume in Zone 2 should be known in advance).

$$V_{dead}=V_{tubing@Zone2}+\left(V_{cell}-\frac{m_{sample}}{\rho_{sample}}\right) \tag{5.5}$$

Since the direct helium expansion method is more practical, the uncertainty analysis in this work is based on this method. On the other hand, the uncertainty associated with the density determination is thoroughly discussed elsewhere [271]. Furthermore, the uncertainty related to the adsorption of helium in the sample is not taken into account here (i.e., helium adsorption is a function of pressure and temperature, and changes from sample to sample, therefore, it is not possible to incorporate into the general uncertainty analysis presented in this work) which is known to be an important source of error in the high pressure sorption isotherm and density measurements [276-278]. Therefore, in reality, the uncertainty in high pressure hydrogen sorption measurements will be more pronounced due to helium adsorption in a sample and needs to be studied for each sample separately.

5.2.2. Computational Analysis Using COMSOL

COMSOL Multiphysics was utilized to calculate the thermal equilibration time (see section 5.3.4) in different sizes of calibrated volumes based on the design of a commercial volumetric apparatus Setaram-HyEnergy PCTPro 2000 [153]. The PCTPro 2000 has three different calibrated volumes (i.e., manifold volume ≈ 12 cc, small reservoir volume ≈ 160 cc and large reservoir volume ≈ (2 x 585 cc) = 1170 cc) which gives the user the flexibility to choose the appropriate reservoir volume depending on the type of measurements (i.e., kinetics or pressure-composition-temperature (PCT)

measurements) and the quantity of a material. In other words, using a smaller volume would be favorable for a smaller sample size because the pressure decrease due to sample sorption can be better resolved by the pressure transducer. The sizes and dimensions of the calibrated volumes in PCTPro 2000 are given in Table 5.1.

Table 5.1. Dimensions of the three different calibrated volumes.

Feature (mm)	Manifold volume (12 cc)	Small reservoir (160 cc)	Large reservoir (1170 cc)
Diameter	3.2	44	38
Length	250	130	450
Wall thickness	0.7	1	1

All volumes are modeled for a stainless steel cylinder with a wall thickness as given in Table 5.1. In the COMSOL analysis, a transient non-isothermal flow module with a volume force was utilized.

5.3. Results and Discussion

5.3.1. Uncertainty Analysis

The uncertainty in the hydrogen uptake of a sample can be calculated once the uncertainty of the measurements (i.e., P, T, V_{dead}, V_{res}, Z(P,T) and R) in Eq. (5.3) is known. The uncertainty in pressure, temperature and reservoir volume is usually available from a manufacturer's datasheet. The uncertainty in R can be determined from the literature as will be discussed in section 5.3.3. On the other hand, the uncertainty in the dead volume and compressibility factor Z(P,T) can be calculated as detailed in section 5.3.2 and Appendices.

5.3.2. Uncertainty in Dead Volume (V_{dead})

Since the dead volume is assumed to be determined by helium expansion from the reservoir volume, the uncertainty in the dead volume is always higher than the

uncertainty in the reservoir volume due to propagation of errors. By assuming there is no helium adsorption in the sample (i.e., $\Delta n_{He}=0$), and by assuming $T_{Zone1} = T_{Zone2} = T_{Zone3}=T$ in Figure 5.1, the dead volume can be determined using a real gas law as follows,

$$\Delta n_{He}=0=\frac{P_{res}\cdot V_{res}}{Z^{He}(P_{res},T)\cdot R\cdot T}-\frac{P_{sys}\cdot V_{sys}}{Z^{He}(P_{sys},T)\cdot R\cdot T} \tag{5.6}$$

By inserting Eq. (5.4) into Eq. (5.6), one can obtain Eq. (5.7) for the dead volume calculation, as

$$V_{dead}=V_{res}\left[\frac{P_{res}}{P_{sys}}-1\right]\cdot\frac{Z^{He}(P_{sys},T)}{Z^{He}(P_{res},T)} \tag{5.7}$$

The uncertainty in the dead volume can be calculated [279] using Eq. (5.8).

$$\frac{U_{V_{dead}}}{V_{dead}}=\sqrt{\begin{array}{c}\left(\frac{V_{res}}{V_{dead}}\cdot\frac{\partial V_{dead}}{\partial V_{res}}\right)^2\cdot\left(\frac{U_{V_{res}}}{V_{res}}\right)^2+\left(\frac{P_{res}}{V_{dead}}\cdot\frac{\partial V_{dead}}{\partial P_{res}}\right)^2\cdot\left(\frac{U_{P_{res}}}{P_{res}}\right)^2+\\ \left(\frac{P_{sys}}{V_{dead}}\cdot\frac{\partial V_{dead}}{\partial P_{sys}}\right)^2\cdot\left(\frac{U_{P_{sys}}}{P_{sys}}\right)^2+\\ \left(\frac{Z^{He}(P_{sys,}T)}{V_{dead}}\cdot\frac{\partial V_{dead}}{\partial Z^{He}(P_{sys,}T)}\right)^2\cdot\left(\frac{U_{Z^{He}(P_{sys,}T)}}{Z^{He}(P_{sys,}T)}\right)^2+\\ \left(\frac{Z^{He}(P_{res,}T)}{V_{dead}}\cdot\frac{\partial V_{dead}}{\partial Z^{He}(P_{res,}T)}\right)^2\cdot\left(\frac{U_{Z^{He}(P_{res,}T)}}{Z^{He}(P_{res,}T)}\right)^2\end{array}} \tag{5.8}$$

After substituting partial derivatives into Eq. (5.8), the final form of the uncertainty in the dead volume is given by Eq. (5.9),

$$\frac{U_{V_{dead}}}{V_{dead}}=\sqrt{\begin{array}{c}\left(\frac{U_{V_{res}}}{V_{res}}\right)^2+\left(\frac{P_{res}}{P_{res}-P_{sys}}\right)^2\cdot\left(\frac{U_{P_{res}}}{P_{res}}\right)^2+\left(\frac{P_{res}}{P_{res}-P_{sys}}\right)^2\cdot\left(\frac{U_{P_{sys}}}{P_{sys}}\right)^2+\\ \left(\frac{Z^{He}(P_{sys},T)}{V_{dead}}\cdot\frac{V_{res}}{Z^{He}(P_{res},T)}\cdot\left(\frac{P_{res}}{P_{sys}}-1\right)\right)^2\cdot\left(\frac{U_{Z^{He}(P_{sys,}T)}}{Z^{He}(P_{sys},T)}\right)^2+\\ \left(\frac{Z^{He}(P_{res,}T)}{V_{dead}}\cdot\frac{V_{res}\cdot Z^{He}(P_{sys},T)}{\left[-Z^{He}(P_{res},T)\right]^2}\cdot\left(\frac{P_{res}}{P_{sys}}-1\right)\right)^2\cdot\left(\frac{U_{Z^{He}(P_{res},T)}}{Z^{He}(P_{res},T)}\right)^2\end{array}} \tag{5.9}$$

As seen from Eq. (5.9), the uncertainty magnification factors (UMFs) of $U_{P_{res}}$ and $U_{P_{sys}}$ are the same and are functions of P_{res} and P_{sys}. Since the P_{res} term appears both in the numerator and denominator of the UMF, P_{sys} should be as small as possible to minimize the UMF which in turn dictates selecting V_{dead} to be as large as possible. However, selecting a very large V_{dead} compared to V_{res} may induce other measurement errors (i.e., temperature gradients within the dead volume, especially problematic for measurements at higher temperatures) and not practical (i.e., a bigger dead volume will limit the highest pressure attainable within the system for single step kinetics measurements). On the other hand, selecting the smallest possible dead volume will result in high uncertainty in V_{dead}. Blach et. al. [271] suggested selecting comparable reservoir and dead volumes to minimize the uncertainty due to sample's density. Therefore, by assuming $V_{res} \cong V_{dead}$, then $P_{res} \cong 2 \times P_{sys}$. The uncertainty in reservoir volume [271] and pressure measurements (i.e., uncertainty of a commercially available pressure transducer is typically 1 % of its reading or better) is taken as 1 %. Finally, the uncertainty in the compressibility factor for helium is calculated as detailed in Appendix B, and the compressibility factors for helium at 300 K for P_{res}=0.4 MPa and P_{sys}=0.2 MPa (i.e., typical pressure values during dead volume determination with PCTPro 2000 and in accordance with the assumption $P_{res} \cong 2 \times P_{sys}$) are determined from REFPROP 8 software [280]. By substituting all the variables into Eq. (5.9), the uncertainty in dead volume, $\frac{U_{V_{dead}}}{V_{dead}}$, is 3.16 %.

Once the uncertainty in dead volume is known, the uncertainty in system volume can be calculated from Eq. (5.10).

$$\frac{U_{V_{sys}}}{V_{sys}} = \sqrt{\left(\frac{U_{V_{res}}}{V_{res}}\right)^2 + \left(\frac{U_{V_{dead}}}{V_{dead}}\right)^2} = 3.32\ \% \tag{5.10}$$

$$\left(\frac{U_{\Delta n_{H_2}}}{\Delta n_{H_2}}\right)_{res} = \sqrt{\left(\frac{U_P}{P}\right)^2 + \left(\frac{U_{V_{res}}}{V_{res}}\right)^2 + \left(\frac{U_{Z(P,T)}}{Z(P,T)}\right)^2 + \left(\frac{U_T}{T}\right)^2} = 1.73\ \% \tag{5.11}$$

5.3.3. Uncertainty in Hydrogen Uptake and its Implications on Reservoir Volume Size Selection and Sample Mass Loading

The total uncertainty in the sample's hydrogen uptake (i.e., Eq. (5.3)) can be determined from Eqs. (5.11), (5.12) and (5.13). The uncertainty in R is significantly smaller (1.7E-4 %) than the uncertainties in P, T, V and Z(P,T), hence it is not included in the uncertainty analysis [281]. The details on the calculation of the uncertainty in Z(P,T) are given in Appendix A. All the uncertainties associated with Eqs. (5.11) and (5.12) are summarized in

By combining Eqs. (5.11) and (5.12), one can calculate the total uncertainty in the hydrogen uptake at the end of a single step measurement (i.e., absorption kinetics measurement) from Eq. (5.13).

Table 5.2. Uncertainties of measurements given in Eq. (5.3).

Measured parameter	**Uncertainty (%)**	**Source for uncertainty value**
Pressure (P)	1	Manufacturer's data
Temperature (T)	1	Manufacturer's data (typical for a K-type thermocouple)
Reservoir volume (V_{res})	1	Ref. [271]
System volume (V_{sys})	3.32	Calculated [in this work]
Compressibility factor for hydrogen (Z(P,T))	0.07	Calculated [in this work] & ref. [282]
Compressibility factor for helium (Z^{He}(P,T))	0.12	Calculated [in this work] & ref. [282]
Universal gas constant (R)	1.7E-4	ref. [281]

$$\frac{U_{\Delta n_{H_2}}}{\Delta n_{H_2}} = \sqrt{\left(\frac{U_{\Delta n_{H_2}}}{\Delta n_{H_2}}\right)_{res}^2 + \left(\frac{U_{\Delta n_{H_2}}}{\Delta n_{H_2}}\right)_{sys}^2} = 3.88\ \% \tag{5.13}$$

However, often hydrogen sorption measurements include the determination of the complete isotherm (i.e., PCT measurements) by gradually increasing the pressure in the sample at a constant temperature. Therefore, the total PCT isotherm comprises numerous single step measurements, and the total hydrogen uptake of a sample can be calculated from Eqs. (5.14) and (5.15) [271]. Nevertheless, the cumulative error analysis for the complete PCT isotherm is pressure dependent and not studied in this work. In other words, the analysis given in this work is only valid for a single dosing step.

$$n_{H_2}^k = \left(\frac{P_{res}^k}{Z\left(P_{res}^k, T\right)\cdot R\cdot T} - \frac{P_{sys}^k}{Z\left(P_{sys}^k, T\right)\cdot R\cdot T}\right)\cdot V_{res} - \left(\frac{P_{sys}^k}{Z\left(P_{sys}^k, T\right)\cdot R\cdot T} - \frac{P_{sys}^{k-1}}{Z\left(P_{sys}^{k-1}, T^{k-1}\right)\cdot R\cdot T^{k-1}}\right)\cdot V_{dead} \tag{5.14}$$

$$\Delta n_{H_2} = \sum_{k=1}^{N} \Delta n_{H_2}^k \tag{5.15}$$

The sample's hydrogen uptake is calculated by subtracting the initial hydrogen content in the reservoir volume from the final hydrogen content in the system volume as given in Eq. (5.3). Therefore, as the hydrogen content in the reservoir volume increases, the absolute uncertainty in the hydrogen content also increases which favors using a reservoir volume as small as possible.

Figure 5.2 shows how the uncertainty in hydrogen uptake varies for different sizes of reservoir volumes as a function of sample's intrinsic hydrogen storage capacity (wt. %) which can be calculated from Eq. (5.16).

$$wt.\% = \frac{\Delta n_{H_2} \cdot \rho_{H_2}}{m_{sample} + \Delta n_{H_2} \cdot \rho_{H_2}} \tag{5.16}$$

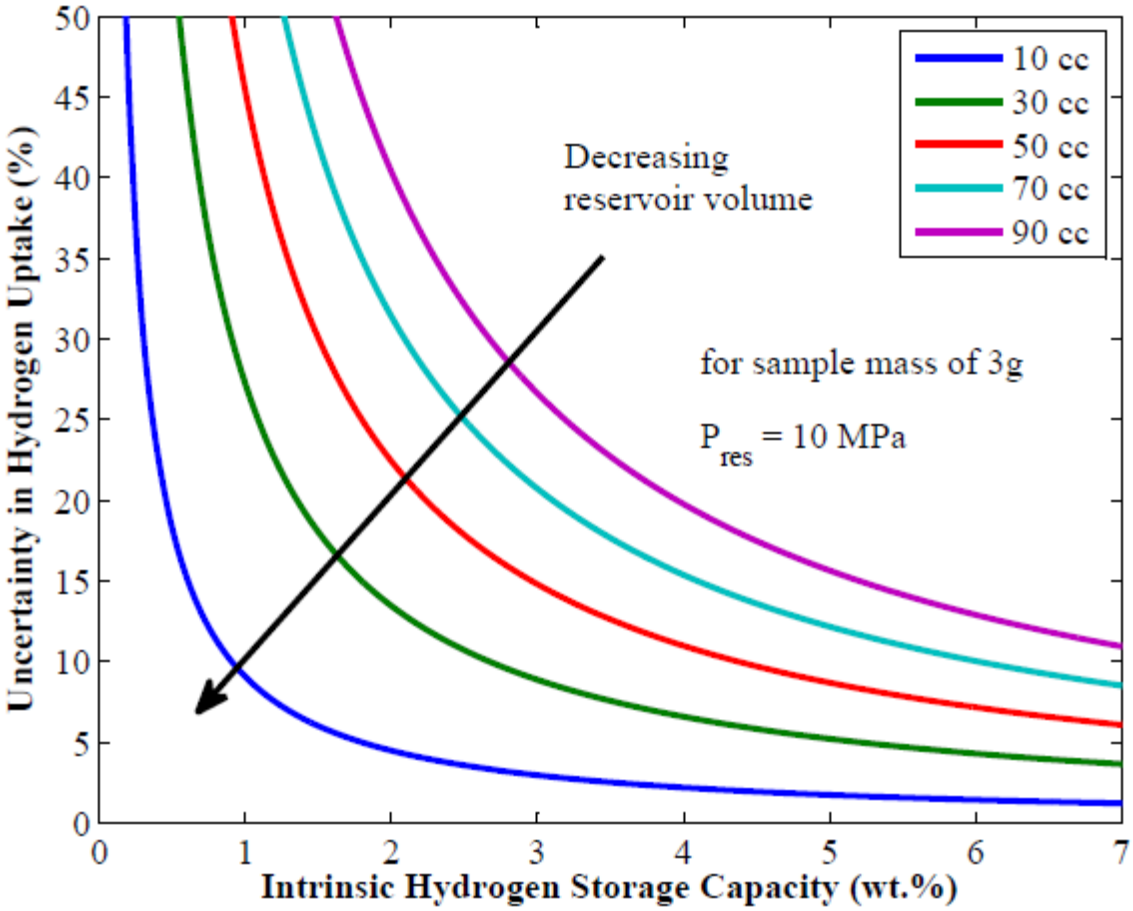

Figure 5.2. The effect of the reservoir volume size in a sample's hydrogen uptake uncertainty.

As stated previously, hydrogen sorption measurements are especially problematic for physisorption based materials where the intrinsic storage capacity is less than 1 wt. %. The rationale behind this phenomenon is clear from Figure 5.2; the uncertainty in the hydrogen uptake increases boundlessly as the sample's intrinsic storage capacity and sample mass loading decrease. This point is further investigated by varying the sample mass in a 10 cc reservoir volume, since a small reservoir volume is more likely to limit the uncertainty in hydrogen uptake.

Figure 5.3 shows that measurements of a small sample (i.e., less than 0.5 g) always result in very high uncertainty when using a 10 cc reservoir volume and should be avoided in high pressure sorption measurements.

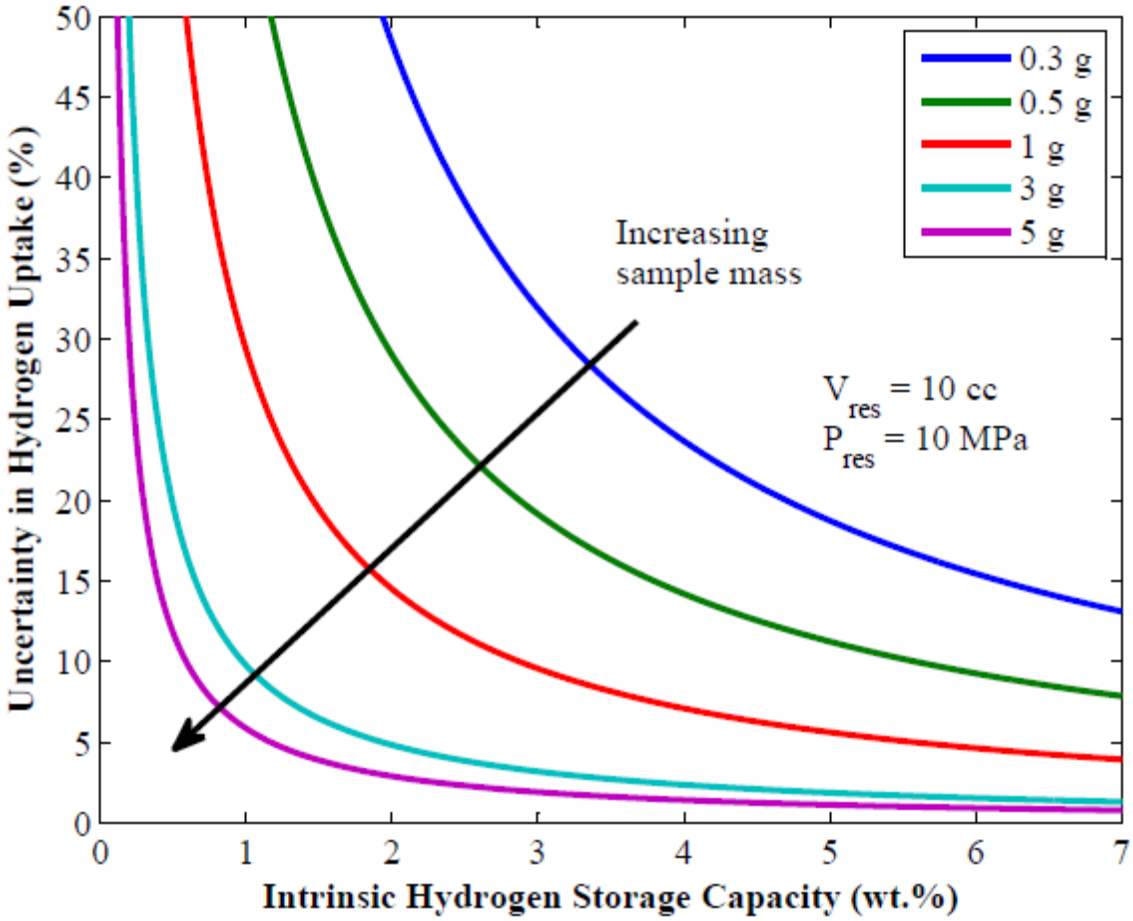

Figure 5.3. The effect of the sample mass loading in a sample's hydrogen uptake uncertainty.

In other words, optimum size of the sample mass loading depends on the size of the reservoir volume and the sample's intrinsic storage capacity, and regardless of the size of the reservoir volume, more sample loading is always favorable. Nevertheless, the selection of the reservoir volume size also depends on the purpose and the type of the experiment. For instance, for single step desorption kinetics measurements selecting a large volume is preferable to keep the back pressure as close as possible to vacuum

conditions, or for single step absorption kinetics measurements a larger volume is required to keep the charging pressure relatively constant over the time, and to keep the system pressure (i.e., charging pressure) close to the initial (i.e., before opening the isolation valve) reservoir pressure when the intention is to charge the sample with high pressure. On the other hand, in PCT measurements (i.e., charging sample with multiple doses) using a smaller volume is desirable due to reasons outlined in this work.

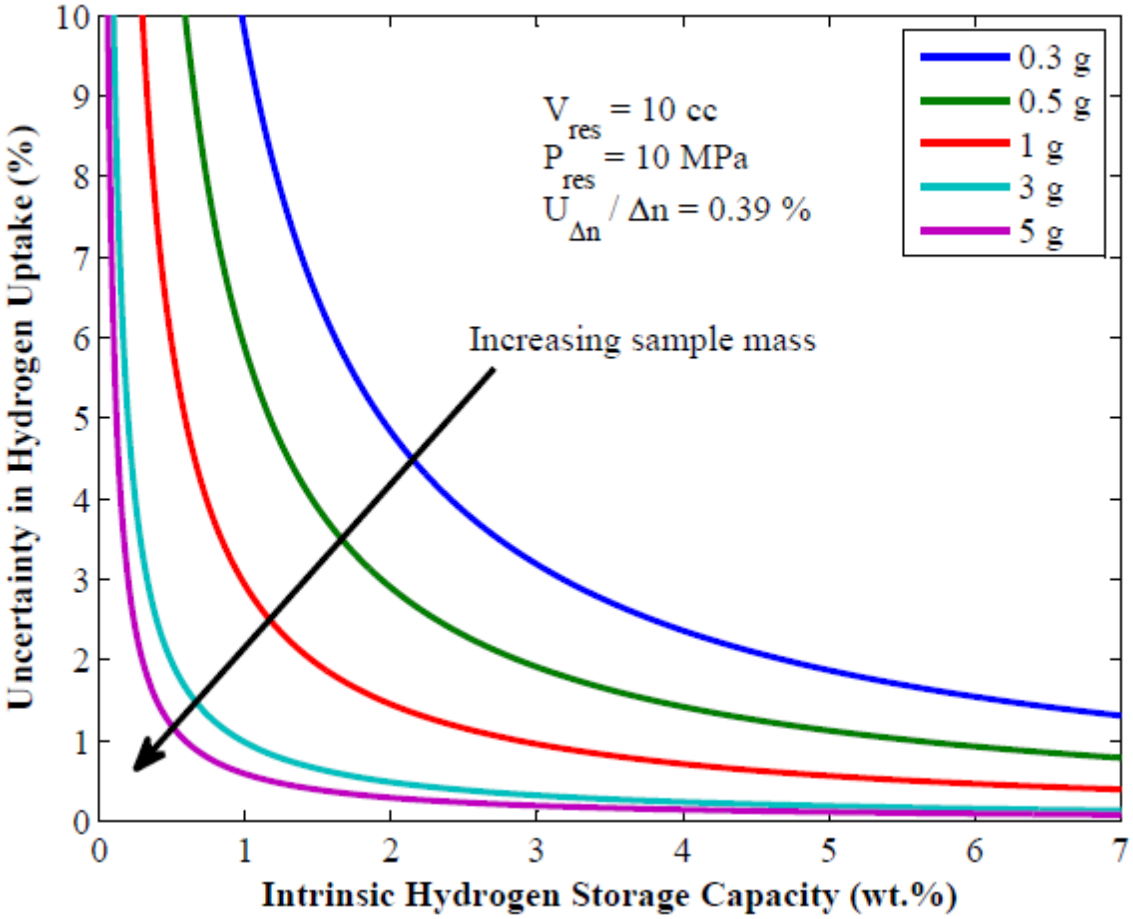

Figure 5.4. Uncertainty in hydrogen uptake for 0.1% uncertainty in pressure and temperature transducers, and reservoir volume.

For some materials it is not possible (i.e., it is time consuming and expensive) to prepare samples (i.e., carbon nanotubes) in gram quantities; in such cases, selecting high accuracy transducers and smallest possible reservoir volumes can alleviate the problem.

For comparison, the uncertainty in hydrogen uptake by assuming 0.1 % uncertainty (i.e., instead of 1 % uncertainty assumed in generating Figures 5.2 and 5.3) in P, T and V_{res} measurements is given in Figure 5.4.

5.3.4. The Effects of Thermal Equilibration Time and the Pseudo Hydrogen Sorption

The thermal equilibration time is one of the critical factors to be considered for accurate hydrogen storage measurements in a volumetric apparatus. Considering the simplified schematic of a volumetric apparatus given in Figure 5.1, if the instrument enclosure temperature (Zone 1) is different than the room temperature (Zone 2) or there is a temperature gradient inside the instrument enclosure, the thermal equilibration time must be considered to minimize the errors.

The thermal equilibration time is an important parameter to be considered at the start of the measurements (i.e., before opening the isolation valve in Figure 5.1). Since the temperature reading is taken from the external surface of the reservoir volume, the actual gas temperature inside the reservoir volume might be different. Therefore, if the measurements (i.e., P and T) start before thermal equilibration is reached, the change in gas temperature will result in an increase or decrease of the gas pressure inside the reservoir volume which in turn will cause erroneous hydrogen uptake values. The effect of the temperature difference between the thermocouple reading and the actual gas temperature (i.e., ΔT) is studied for ΔT = 1 K, 3 K, and 5 K using the real gas equation of state given in Eq. (5.17),

$$Z(p,T)=\frac{p}{\rho RT}=1+\sum_{i=1}^{9} a_i \left(\frac{100\ \mathrm{K}}{T}\right)^{b_i} \left(\frac{p}{1\ \mathrm{MPa}}\right)^{c_i} \tag{5.17}$$

where the constants a_i, b_i and c_i are taken from Lemmon et al. [282].

Figure 5.5 shows the pseudo hydrogen sorption due to changes in the actual hydrogen temperature (i.e., $\Delta T = T(t_o) - T(t_{th})$)[12] for three different calibrated volumes of PCTPro 2000 (see section 5.2.1 for details) at 100 atm.

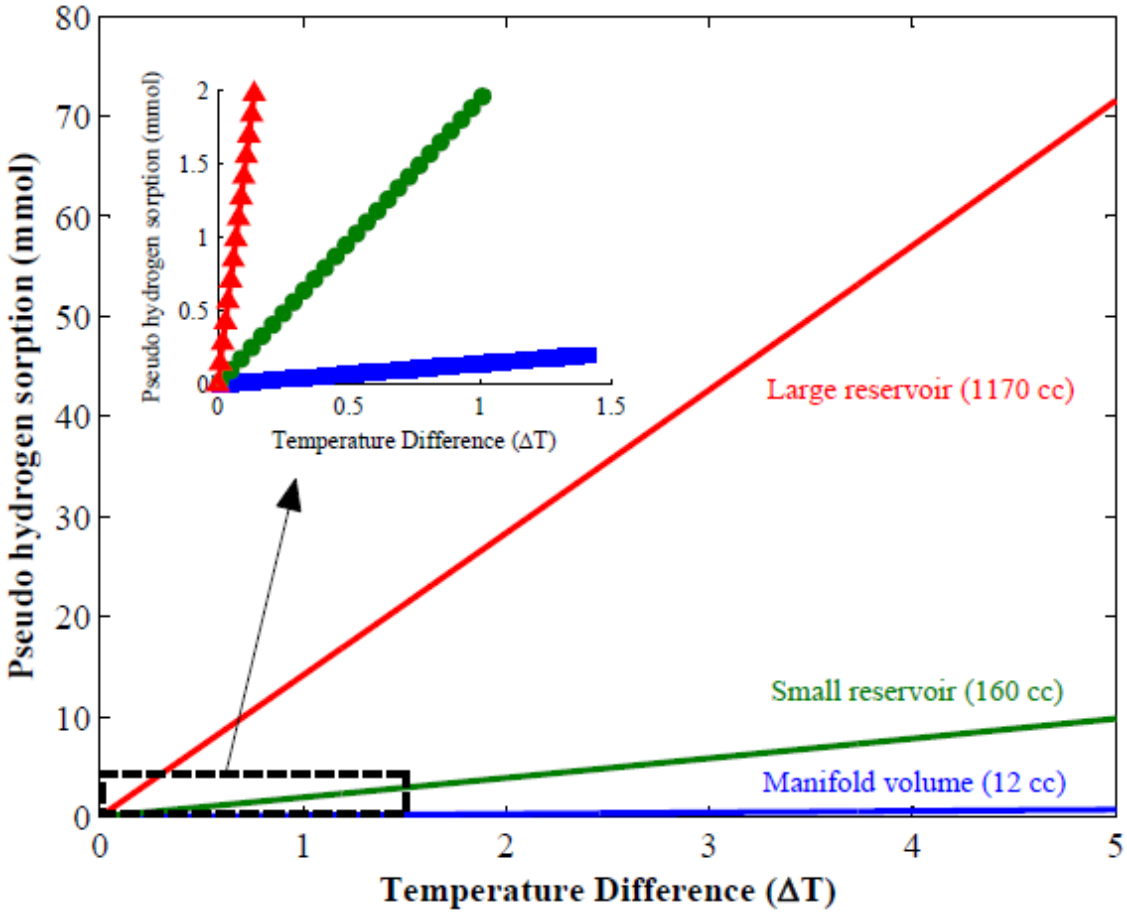

Figure 5.5. Pseudo hydrogen sorption as a function of ΔT at 100 atm.

The larger the calibrated volume the larger the error in the measurements, since the quantity of hydrogen gas in the larger volume (i.e., large reservoir) is considerably bigger than the one in the small volume (i.e. manifold volume). The inset in Figure 5.5 shows that even small temperature differences (ΔT=0.1 K) can cause significant pseudo

[12] $T(t_o)$ is the temperature of the hydrogen initially (at t = 0), $T(t_{th})$ is the temperature of the hydrogen when it is in thermal equilibrium with the instrument enclosure (i.e., when actual gas temperature is equal to the thermocouple reading and assuming instrument enclosure is isothermal).

sorption as the reservoir volume increases. This outcome is also in agreement with the uncertainty analysis which favors using a reservoir volume as small as possible; however, as discussed in section 5.3.3, the selection of the reservoir volume size also needs to be compatible with the goals of the experiment.

5.3.5. Computational Analysis of the Thermal Equilibration Times

From the foregoing discussion, it is clear that thermal equilibration is crucial for accurate hydrogen storage measurements. Therefore, the necessary thermal equilibration times for three different calibrated volumes were analyzed using COMSOL (see section 5.2.2 for details). In the analysis, the volume force is included to account for natural convection. Although, natural convection plays no role at steady state (i.e., all walls are isothermal), it has a significant effect in the transient regime. Figure 5.6 shows the effect of the natural convection as well as the orientation of the small reservoir on the thermal equilibration time.

Figure 5.7 shows the change of the actual hydrogen temperature under isothermal heating at 301 K for three different ΔT. The hydrogen gas inside the manifold volume reaches thermal equilibrium within 30 s at the worst case (i.e., $\Delta T = 5$ K), due its highest heat transfer surface area per hydrogen molecule (i.e., a narrow and long reservoir volume is favored over a wide and short one). However, for both the small and large reservoir volumes, thermal equilibrium is reached (i.e., $\Delta T < 0.1$ K) within 300 s. Therefore, before opening the isolation valve, shown in Fig. 1, it is necessary to wait for 5 min for thermal equilibrium. Figure 5.8 shows the corresponding increase in the hydrogen pressure due to the temperature increase in the calibrated volumes (initially at 100 atm), for $\Delta T = 5$ K, 3 K and 1 K.

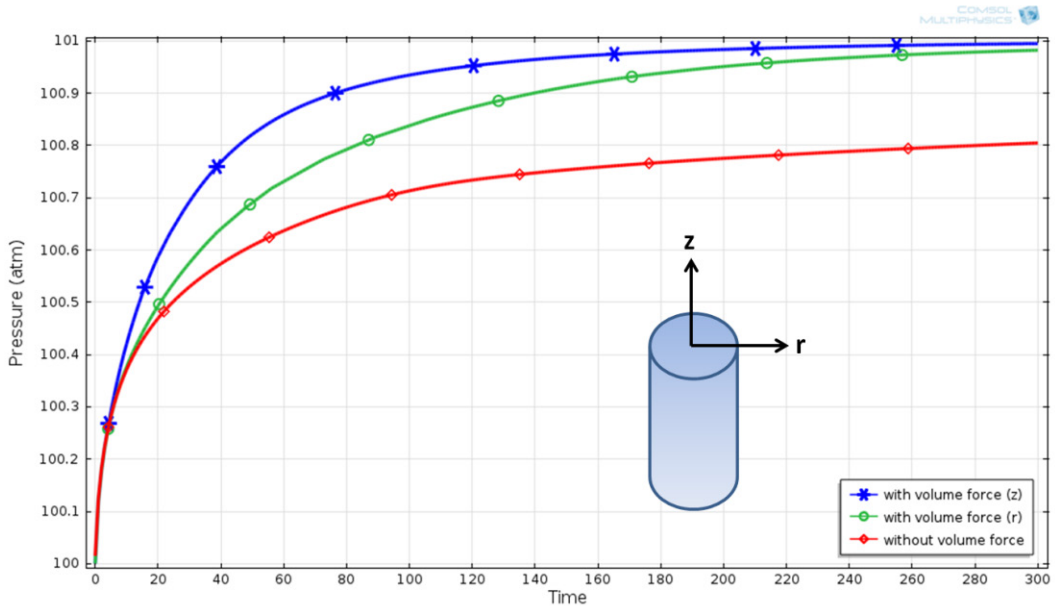

Figure 5.6. The effect of the natural convection and the orientation of the reservoir in thermal equilibration time for the 160 cc small reservoir volume.

To emphasize the effect of the thermal equilibration time on the measurement errors, the relative error due to pseudo hydrogen sorption for varying sample mass and intrinsic storage capacity of a sample is plotted in Figure 5.9. The relative error percentage is calculated as follows,

$$\text{Error (\%)} = \frac{\text{pseudo sorption (mol)}}{\text{pseudo sorption (mol)} + \text{sample's sorption (mol)}} \times 100 \qquad (5.18)$$

The results show that the error is quite high especially for low storage capacity materials (i.e., 0.5 wt. %) when using a small reservoir volume (i.e., 160 cc) even for a temperature difference as small as 1 K. In accordance with the previous results, the higher the sample mass loading is the smaller the error. Fortunately, thermal equilibration time related error can simply be avoided by waiting for the system to reach the thermal equilibrium.

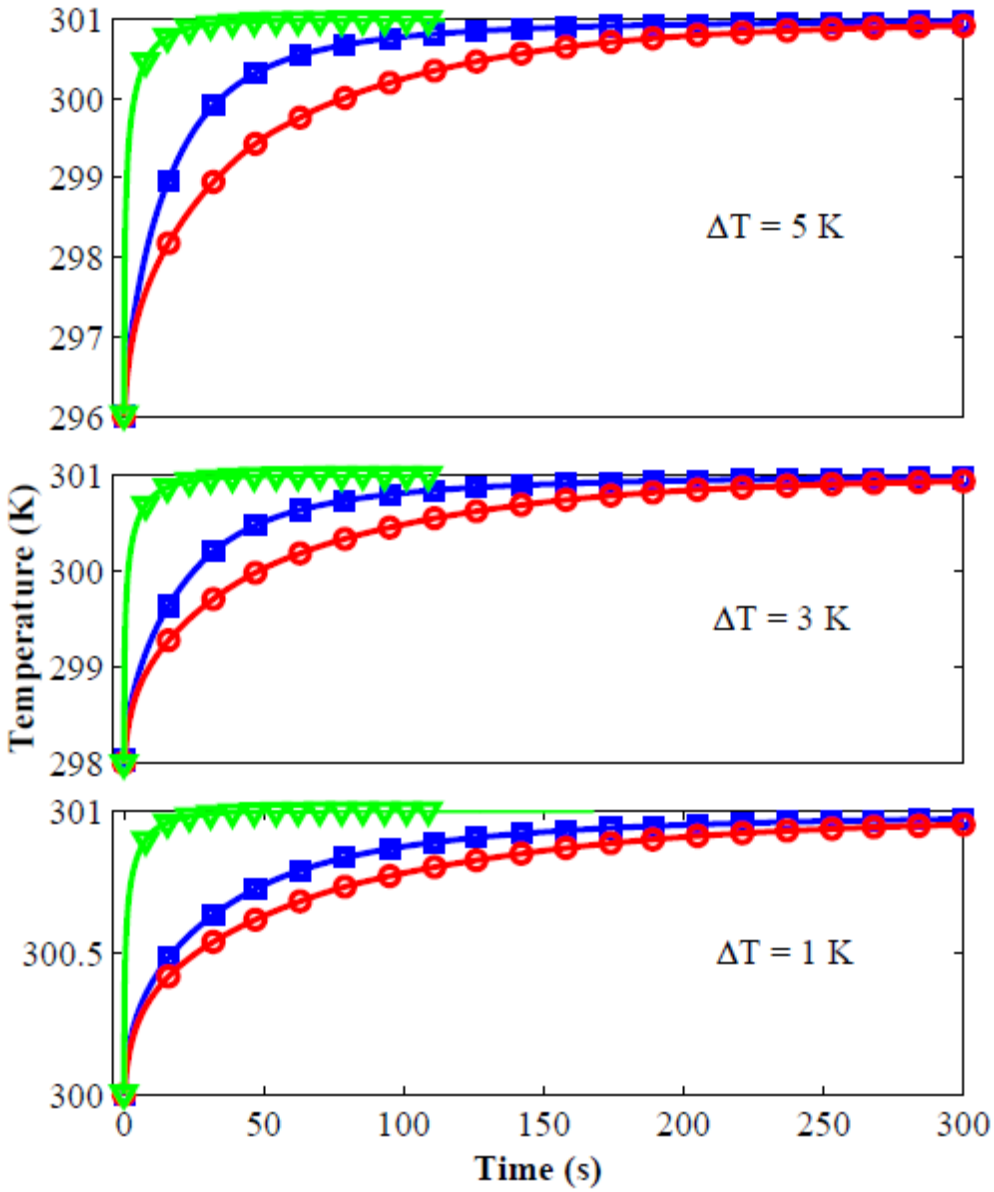

Figure 5.7. Thermal equilibration times of three different calibrated volumes for various ΔT (i.e., the difference between the actual gas temperature inside the reservoir and the thermocouple reading). Triangle, square and circle represent the manifold, large and small reservoir, respectively.

In other words, the errors due to thermal equilibration time are avoidable, not like the uncertainty errors in calculation of the hydrogen uptake of a sample which can be minimized but can never be eliminated. For comparison, the relative errors for the

manifold volume (i.e., 12 cc) and 1 K temperature difference are plotted in Figure 5.10 which shows less than 5 % error in the worst case.

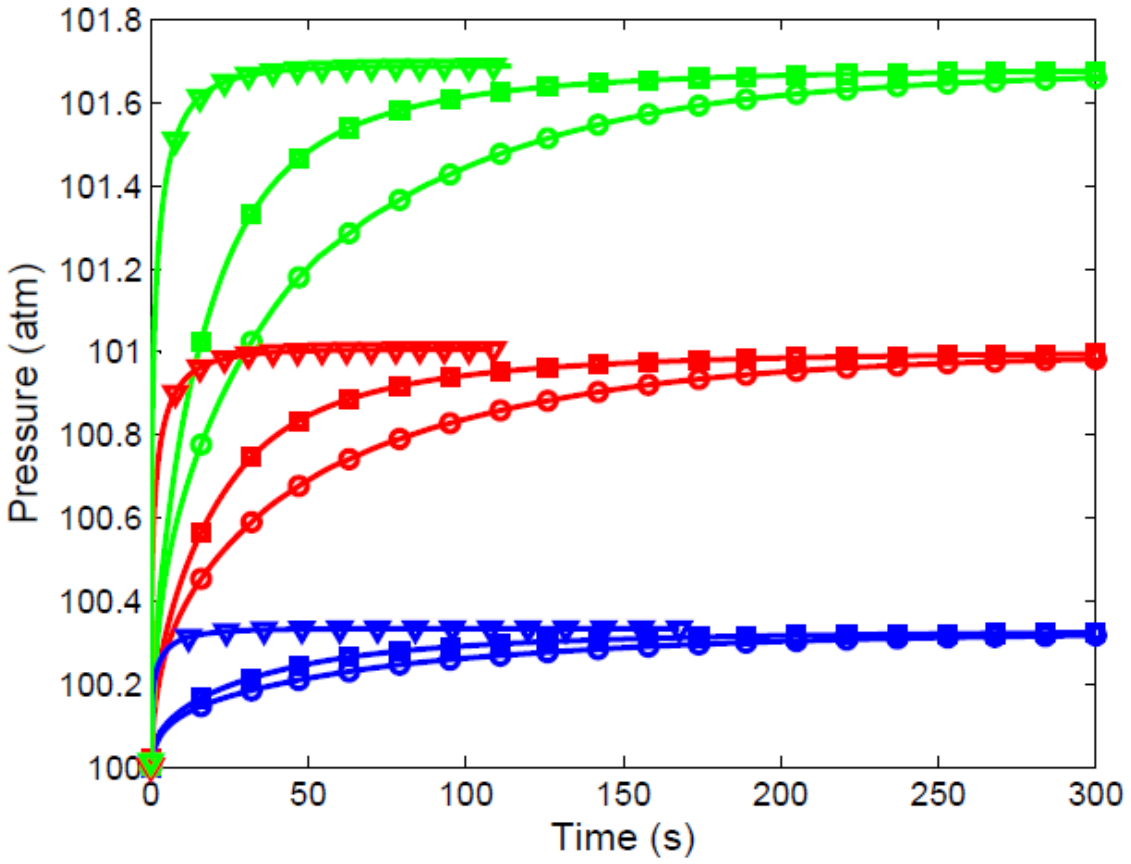

Figure 5.8. Pressure increase due to temperature increase during thermal equilibration. Green, red and blue represent ΔT = 5 K, 3 K and 1 K, respectively. Triangles, squares and circles represent manifold volume (i.e., 12 cc), large reservoir (i.e., 1170 cc) and small reservoir (i.e., 160 cc), respectively.

5.3.6. Significance of a Proper Experimental Procedure and Material Related Issues for Accurate Hydrogen Sorption Measurements

The study presented here is focused on the design stage uncertainty analysis of a volumetric apparatus and the importance of the thermal equilibration time for accurate measurements. However, most erroneous results reported in published hydrogen sorption measurements are related to the poor experimental procedures or material related issues, not due to poor design of an instrument. Therefore, experimentalists should keep in mind

it is extremely important to follow a very well defined protocol. Every measurement should start with testing a blank, non ab/desorbing sample (i.e., sea sand), to determine any systematic error within the volumetric apparatus. The hydrogen quantity desorbed from a sample should be in accordance with the absorbed quantity under identical conditions (i.e., isothermal conditions) if there is no sample related issue.

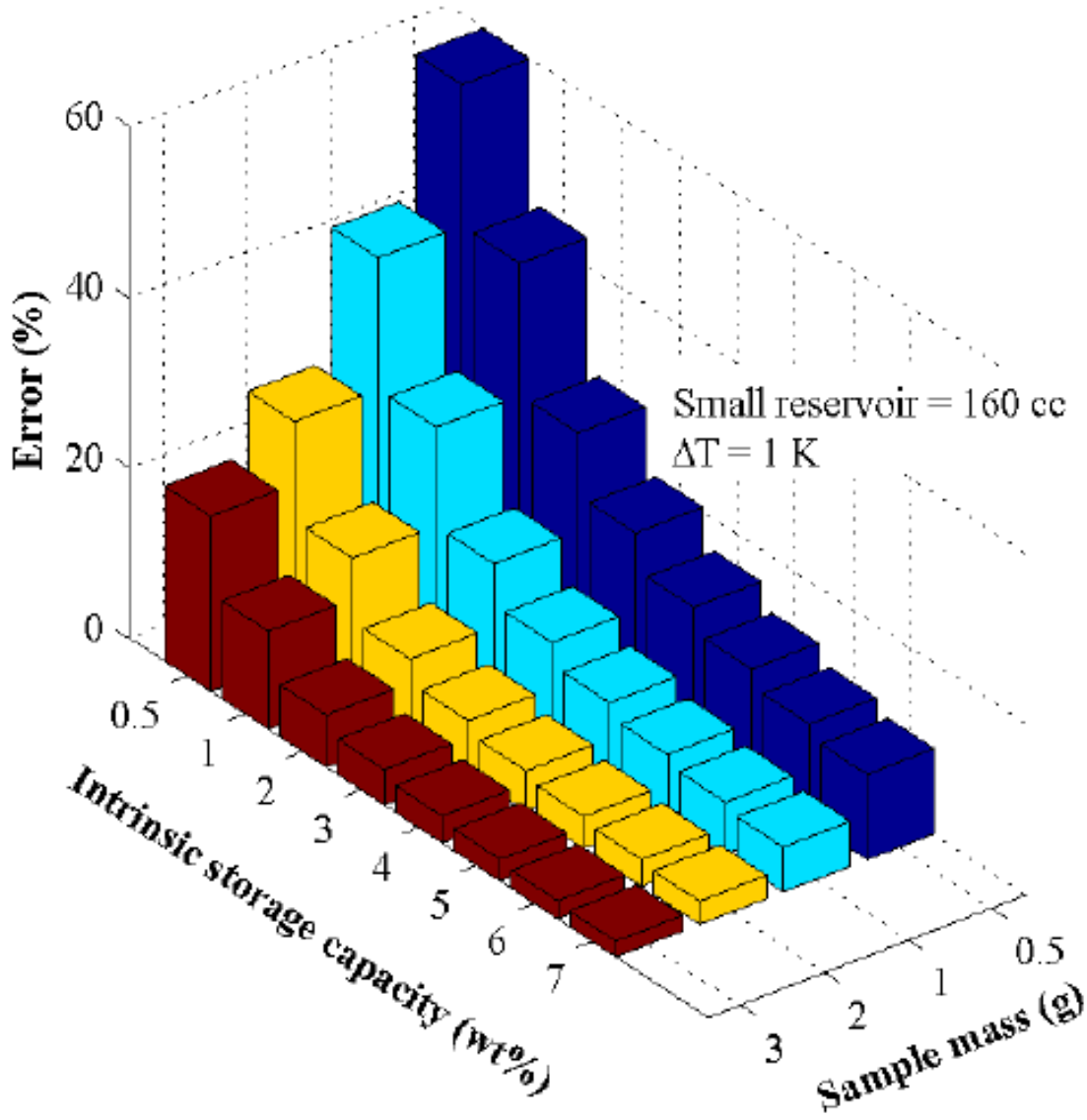

Figure 5.9. Relative error due to 1 K temperature increase of the hydrogen gas in the small reservoir for varying sample mass loading and intrinsic storage capacity of a sample.

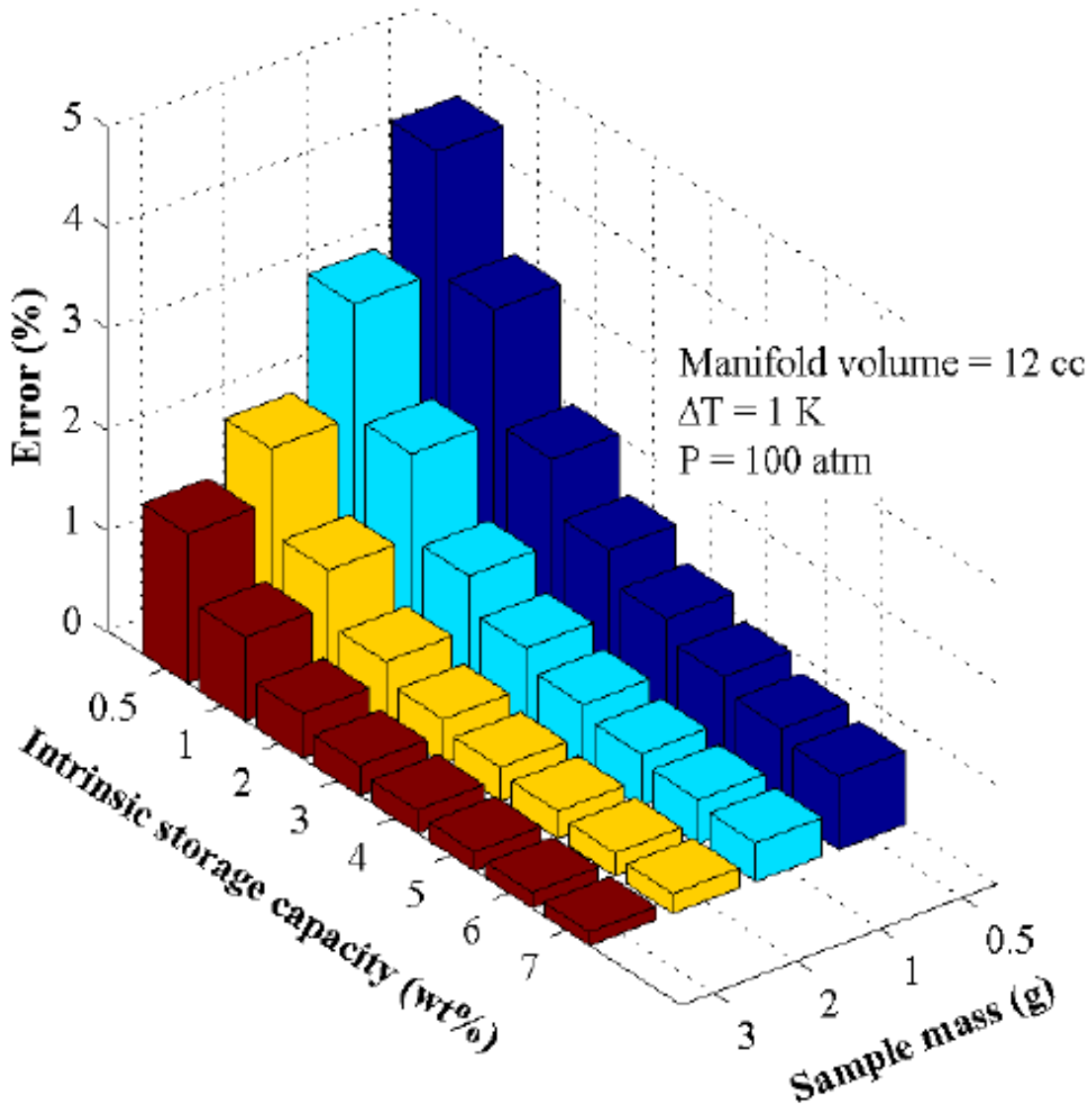

Figure 5.10. Relative error due to 1 K temperature increase of the hydrogen gas in the manifold volume for varying sample mass loading and intrinsic storage capacity of a sample.

For measurements conducted at a higher or lower temperature than the instrument enclosure temperature (i.e., $T_{zone1} \neq T_{zone2} \neq T_{zone3}$ in Figure 5.1), there will be temperature gradients within the sample and the gas surrounding it and needs to be considered for accurate measurements. Even for measurements conducted at isothermal conditions throughout the system (i.e., $T_{zone1} \neq T_{zone2} \neq T_{zone3}$ in Figure 5.1), the exothermic or

endothermic nature of the sorption process can cause temperature gradients within the sample and the gas surrounding it. For more complete discussion of the experimental and material related issues refer to Gross et al. [269].

5.4. Conclusions

In this study, the design of a volumetric apparatus for high pressure hydrogen sorption measurements was investigated in detail by an uncertainty analysis considering the sample mass loading, pressure and temperature transducer accuracy, reservoir and system volume, and the sample's intrinsic storage capacity. The sample mass loading is one of the most important parameters to be considered regardless of the characteristics of the system and the sample. In general, the higher the sample mass loading the lower the uncertainty in measurements, and the optimal loading being a function of the sample's intrinsic storage capacity. When the material to be tested is not available in gram quantities (i.e., larger sample mass loading is required for low capacity materials to keep the uncertainty low), using high accuracy pressure and temperature transducers can significantly alleviate the uncertainty in the measurements. The reservoir volume should be as small as possible (i.e., 10 cc) in high pressure sorption measurements to minimize the uncertainty. For highest accuracy, the system should not contain significantly more gas than the sample can absorb since the amount of hydrogen in the sample at a specific P and T is fixed, and the error in measuring this amount will depend on how large or small this amount is compared to the hydrogen in the gas phase. Moreover, the effect of thermal equilibration time on the hydrogen storage measurements was investigated. If there is a possibility (i.e., when the instrument enclosure temperature and the room temperature are not the same or there is a temperature gradient within the instrument

enclosure) that the actual gas temperature inside the reservoir volume could be different than the ambient temperature, then the thermal equilibration time needs to be taken into account. Depending on the size and shape of the reservoir volume, a temperature difference as small as 0.1 K can cause significant errors. According to the computational analysis, a 5 min wait time is required for thermal equilibrium to be established. In addition, temperature readings should be taken from multiple points, especially if the temperature gradients within the instrument enclosure are significant (i.e., more than 0.1 K). To minimize the thermal equilibration time, the heat transfer surface area of the reservoir volume needs to be maximized by using a long and narrow reservoir instead of a wide and short one.

5.5. Nomenclature

k	step number in a PCT measurement
m_{sample}	mass of a sample, g
n	gas quantity, mol
n_i	initial hydrogen content in the reservoir volume, mol
n_f	final hydrogen content in the system volume, mol
N	total number of steps in a PCT measurement
P	pressure, MPa
PCT	pressure-concentration-temperature
R	universal gas constant, J/(mol•K)
t	time, s
T	absolute temperature, K
T_{Zone1}	instrument enclosure temperature, K

T_{Zone2}	room temperature, K
T_{Zone3}	sample temperature, K
U	uncertainty
UMF	uncertainty magnification factor
V	volume, cm^3
V_{sys}	system volume, cm^3
V_{res}	reservoir volume, cm^3
V_{dead}	dead space volume, cm^3
V_{cell}	sample cell volume, cm^3
$V_{tubing@Zone2}$	tubing volume in between the isolation valve and the sample cell in Zone2, cm^3
Z	compressibility factor of hydrogen
Z^{He}	compressibility factor of helium

Greek symbols

ρ	density of a gas, g/mol
ρ_{H_2}	density of hydrogen, g/mol
ρ_{sample}	density of a sample, g/cm^3

Chapter 6. Conclusions

6.1. Overview

In this dissertation work, two types of promising solid state hydrogen storage materials have been studied. First, spillover enhancement in hypercrosslinked polystyrene, a porous polymer, is investigated in detail. Two different Pt doped hypercrosslinked polystyrene samples were prepared by the wet impregnation method and bridge building technique to study the effects of the spillover phenomenon. The sample prepared via the bridge building technique (MN270-bridged) showed enhanced storage capacity (0.36 wt. %) compared to the base sample (0.32 wt. %) at 294 K and 10 MPa; however, the storage capacity of the MN270-bridged is too low for practical applications. Second, the effects of SWCNTs supported ruthenium (Ru) catalyst on the kinetics and ammonia suppression in the Li-Mg-N-H complex hydride system, a reversible hydride, was investigated. Results showed that Ru doped SWCNTs is a promising catalyst to suppress the ammonia emission in the Li-Mg-N-H complex hydride. Moreover, structural defects in SWCNTs are shown to play an important role on kinetics enhancement in the Li-Mg-N-H system. Finally, the accuracy of the volumetric hydrogen storage measurements was investigated in detail. Since the progress in the hydrogen storage research is directly related to the accuracy and reliability of the results reported in the literature, guidelines are developed through uncertainty analysis and computational study for accurate hydrogen storage measurements. Main outcomes from

this dissertation work and the recommendations for future work are further discussed in the following sections.

6.2. Spillover Enhancement in Pt Doped Hypercrosslinked Polystyrene

The spillover phenomenon within the hydrogen storage context is the dissociation of the hydrogen molecules over transition metal atoms, and the subsequent diffusion and bonding of the spiltover hydrogen atoms in the support (i.e., carbon). Despite very promising results reported in the literature, spillover enhancement remains to be a highly disputable topic due to contrary results reporting no enhancement at all. The spillover enhancement was studied for activated carbons and metal organic frameworks (MOFs) extensively; however, there was no study on polymers. Therefore, the effects of spillover enhancement in Pt doped (2-5 nm) hypercrosslinked polystyrene (HPS) was investigated. The surface area is an important parameter (i.e., the higher the better) that needs to be considered for the highest possible hydrogen uptake at room temperature and high pressure. HPS was selected due to its relatively high surface area (≈ 1500 m^2/g) as compared to the hypercrosslinked polyaniline (≈ 350 m^2/g). The Pt doped HPS samples were prepared by two different synthetic procedures; namely incipient wetness impregnation and the bridge building technique. The results showed that the samples prepared by the bridge building technique performed slightly better (10%) than the samples prepared by the incipient wetness impregnation method. However, the hydrogen storage capacity (0.32 wt. %) of the best performing sample was still very low to be utilized in practical applications. Nevertheless, for the first time, the bridge building technique was shown to be effective in spillover enhancement in polymers.

6.3. Effects of SWCNTs Supported Ru Catalyst on Kinetics and Ammonia Suppression in the $LiNH_2$–MgH_2 Complex Hydride System

$LiNH_2$-MgH_2 (Li-Mg-N-H) is one of the promising reversible hydrogen storage materials that has been studied extensively. One of the drawbacks of the Li-Mg-N-H system is NH_3 emission which is detrimental to the proton exchange membrane fuel cells even at trace levels. In addition, NH_3 emission results in loss of gravimetric capacity over cycles. Therefore, it is of paramount importance to limit or eliminate the NH_3 emission in the Li-Mg-N-H system for practical applications. On the other hand, sluggish kinetics of the Li-Mg-N-H system also needs to be improved. According to the proposed reaction mechanisms, Li ion diffusion plays an important role in the Li-Mg-N-H system and the single walled carbon nanotubes (SWCNTs) with defects are suitable medium for Li ion diffusion. Moreover, Ru doped single walled carbon nanotubes (SWCNTs) is known to be an active catalyst for the NH_3 decomposition. Therefore, synergistic effects of Ru doped (≈ 2 nm) SWCNTs on NH_3 emission and kinetics of the Li-Mg-N-H system were studied. The pristine SWCNT doped Li-Mg-N-H system showed increased NH_3 emission as compared to the base Li-Mg-N-H sample. However, Ru doped SWCNT including Li-Mg-N-H sample released less NH_3 compared to the pristine SWCNT including sample. The results showed that NH_3 decomposition starts at a temperature as low as 200°C. Nevertheless, it was not possible to eliminate all NH_3 release. On the other hand, pristine SWCNTs including Li-Mg-N-H sample showed degraded performance in terms of kinetics, whereas Ru doped SWCNTs including Li-Mg-N-H sample showed similar performance as of Li-Mg-N-H base sample. Further studies are required to optimize the Ru particle size, and better ways other than the ball milling are required to mix the Ru doped SWCNTs with the Li-Mg-N-H sample to effectively control the structural defects

introduced into the SWCNTs. In summary, we have shown that through NH_3 decomposition it may be possible to completely eliminate NH_3 emission from the Li-Mg-N-H system.

6.4. Accuracy of Hydrogen Storage Measurements

The errors in hydrogen sorption measurements are of major concern in the hydrogen storage community which impede the down selection process of candidate materials and set back progress in the field. The volumetric (Sievert's type) apparatus is the most widely utilized instrument in the hydrogen storage literature since it is easy to operate and fabricate and better suited to the rapid screening of the samples. Through design stage uncertainty analysis, basic guidelines are developed to improve the accuracy of the volumetric hydrogen storage measurements. The results showed that reservoir volume should be as small as possible to minimize the uncertainty. In addition, sample loading has a profound effect on the measurement accuracy. In general, more sample loading is always favorable. The sample loading amount is an important parameter especially for physisorption based materials where the intrinsic storage capacity is low. Another way to improve the measurement accuracy is it to utilize high accuracy pressure and temperature transducers when the material to be tested is not available in gram quantities. More importantly, thermal equilibration time within the instrument enclosure shown to be an important parameter that can affect the measurement accuracy. The numerical analysis based on COMSOL showed that 5 min wait time is necessary to level off any temperature gradients due to temperature differences in between ambient and instrument enclosure temperatures.

6.5. Recommendations for Future Work

More fundamental research in spillover enhancement is required to address the discrepancies of the results reported by different labs. Ab initio studies showed that spillover enhancement has a great potential; however, it is not practically yet possible to disperse transition metal atoms in the atomic level. Therefore, synthetic procedures to disperse transition metals in the atomic level are highly desirable.

Further studies are required to optimize the Ru particle size, and better ways other than ball milling are required to mix the Ru doped SWCNTs with the Li-Mg-N-H sample to effectively control the structural defects introduced into the SWCNTs. In brief, we have shown that through NH_3 decomposition it may be possible to completely eliminate NH_3 emission from the Li-Mg-N-H system.

Further computational work based on the three dimensional thermal analysis of the volumetric apparatus would be beneficial to the designers of the Sievert's type instruments. Moreover, the analysis presented in this study is only valid for single step measurements (i.e., kinetics measurements); therefore, uncertainty analysis of multistep measurements, which includes pressure-concentration-temperature (PCT) type measurements, can also contribute to this field.

References

[1] Maggio G, Cacciola G. A variant of the Hubbert curve for world oil production forecasts. Energy Policy 2009;37:4761-70.

[2] Tsoskounoglou M, Ayerides G, Tritopoulou E. The end of cheap oil: Current status and prospects. Energy Policy 2008;36:3797-806.

[3] Houghton J. Global warming. Reports on Progress in Physics 2005;68:1343.

[4] Asif M, Muneer T. Energy supply, its demand and security issues for developed and emerging economies. Renewable and Sustainable Energy Reviews 2007;11:1388-413.

[5] Armaroli N, Balzani V. The future of energy supply: Challenges and opportunities. Angewandte Chemie International Edition 2006;46:52-66.

[6] Dincer I. Renewable energy and sustainable development: a crucial review. Renewable and Sustainable Energy Reviews 2000;4:157-75.

[7] White C, Steeper R, Lutz A. The hydrogen-fueled internal combustion engine: a technical review. International Journal of Hydrogen Energy 2006;31:1292-305.

[8] Steinfeld A. Solar thermochemical production of hydrogen-a review. Solar Energy 2005;78:603-15.

[9] Ni M, Leung MK, Leung DY, Sumathy K. A review and recent developments in photocatalytic water-splitting using TiO2 for hydrogen production. Renewable and Sustainable Energy Reviews 2007;11:401-25.

[10] Kalinci Y, Hepbasli A, Dincer I. Biomass-based hydrogen production: a review and analysis. International Journal of Hydrogen Energy 2009;34:8799-817.

[11] Marban G, Valdés-Solís T. Towards the hydrogen economy? International Journal of Hydrogen Energy 2007;32:1625-37.

[12] Turner JA. Sustainable hydrogen production. Science 2004;305:972-4.

[13] Crabtree GW, Dresselhaus MS, Buchanan MV. The hydrogen economy. Physics Today 2004;57:39.

[14] Abbas HF, Wan Daud W. Hydrogen production by methane decomposition: a review. International Journal of Hydrogen Energy 2010;35:1160-90.

[15] Gerboni R, Salvador E. Hydrogen transportation systems: Elements of risk analysis. Energy 2009;34:2223-9.

[16] Lattin W, Utgikar VP. Transition to hydrogen economy in the United States: A 2006 status report. International Journal of Hydrogen Energy 2007;32:3230-7.

[17] Satyapal S, Petrovic J, Read C, Thomas G, Ordaz G. The U.S. Department of Energy's national hydrogen storage project: Progress towards meeting hydrogen-powered vehicle requirements. Catalysis Today 2007;120:246-56.

[18] Bossel U. Does a hydrogen economy make sense? Proceedings of the IEEE 2006;94:1826-37.

[19] Bossel U, Eliasson B, Taylor G. The future of the hydrogen economy: bright or bleak? Cogeneration and Distributed Generation Journal 2003;18:29-70.

[20] Shinnar R. The hydrogen economy, fuel cells, and electric cars. Technology in Society 2003;25:455-76.

[21] G. Hoyer K, Holden E. Alternative fuels and sustainable mobility: is the future road paved by biofuels, electricity or hydrogen? International Journal of Alternative Propulsion 2007;1:352-68.

[22] Tarascon J-M. Key challenges in future Li-battery research. Philosophical Transactions of the Royal Society A: Mathematical, Physical and Engineering Sciences 2010;368:3227-41.

[23] Chalk SG, Miller JF. Key challenges and recent progress in batteries, fuel cells, and hydrogen storage for clean energy systems. Journal of Power Sources 2006;159:73-80.

[24] Zhou L. Progress and problems in hydrogen storage methods. Renewable and Sustainable Energy Reviews 2005;9:395-408.

[25] Eberle U, Felderhoff M, Schüth F. Chemical and physical solutions for hydrogen storage. Angewandte Chemie International Edition 2009;48:6608-30.

[26] Conte M, Iacobazzi A, Ronchetti M, Vellone R. Hydrogen economy for a sustainable development: state-of-the-art and technological perspectives. Journal of Power Sources 2001;100:171-87.

[27] Felderhoff M, Weidenthaler C, von Helmolt R, Eberle U. Hydrogen storage: the remaining scientific and technological challenges. Physical Chemistry Chemical Physics 2007;9:2643-53.

[28] Jensen C, Gross K. Development of catalytically enhanced sodium aluminum hydride as a hydrogen-storage material. Applied Physics A: Materials Science & Processing 2001;72:213-9.

[29] Bakker S. Hydrogen patent portfolios in the automotive industry–The search for promising storage methods. International Journal of Hydrogen Energy 2010;35:6784-93.

[30] Hamilton CW, Baker RT, Staubitz A, Manners I. B–N compounds for chemical hydrogen storage. Chemical Society Reviews 2009;38:279-93.

[31] Umegaki T, Yan J-M, Zhang X-B, Shioyama H, Kuriyama N, Xu Q. Boron-and nitrogen-based chemical hydrogen storage materials. International Journal of Hydrogen Energy 2009;34:2303-11.

[32] Thomas KM. Hydrogen adsorption and storage on porous materials. Catalysis Today 2007;120:389-98.

[33] Morris RE, Wheatley PS. Gas storage in nanoporous materials. Angewandte Chemie International Edition 2008;47:4966-81.

[34] US Department of Energy Office of Energy Efficiency and Renewable Energy and The FreedomCAR and Fuel Partnership.Targets for Onboard Hydrogen Storage Systems for Light-Duty Vehicles, 2009. [cited 2013 March 30]; Available from: http://www1.eere.energy.gov/hydrogenandfuelcells/storage/pdfs/targets_onboard_hydro_storage_explanation.pdf.

[35] Read C, Thomas G, Ordaz G, Satyapal S. U.S. Department of Energy's system targets for nn-board vehicular hydrogen storage. Material Matters 2007;2:3-5.

[36] Sakintuna B, Lamari-Darkrim F, Hirscher M. Metal hydride materials for solid hydrogen storage: a review. International Journal of Hydrogen Energy 2007;32:1121-40.

[37] Takagi H, Hatori H, Soneda Y, Yoshizawa N, Yamada Y. Adsorptive hydrogen storage in carbon and porous materials. Materials Science and Engineering: B 2004;108:143-7.

[38] Graetz J. New approaches to hydrogen storage. Chemical Society Reviews 2009;38:73-82.

[39] Zaluska A, Zaluski L, Ström-Olsen J. Structure, catalysis and atomic reactions on the nano-scale: a systematic approach to metal hydrides for hydrogen storage. Applied Physics A: Materials Science & Processing 2001;72:157-65.

[40] Chandra D, Reilly JJ, Chellappa R. Metal hydrides for vehicular applications: the state of the art. JOM Journal of the Minerals, Metals and Materials Society 2006;58:26-32.

[41] Noritake T, Aoki M, Towata S, Seno Y, Hirose Y, Nishibori E, Takata M, Sakata M. Chemical bonding of hydrogen in MgH2. Applied Physics Letters 2002;81:2008-10.

[42] Noritake T, Towata S, Aoki M, Seno Y, Hirose Y, Nishibori E, Takata M, Sakata M. Charge density measurement in MgH2 by synchrotron X-ray diffraction. Journal of Alloys and Compounds 2003;356:84-6.

[43] Oelerich W, Klassen T, Bormann R. Metal oxides as catalysts for improved hydrogen sorption in nanocrystalline Mg-based materials. Journal of Alloys and Compounds 2001;315:237-42.

[44] Liang G, Huot J, Boily S, Van Neste A, Schulz R. Catalytic effect of transition metals on hydrogen sorption in nanocrystalline ball milled MgH2 - Tm (Tm= Ti, V, Mn, Fe and Ni) systems. Journal of Alloys and Compounds 1999;292:247-52.

[45] Principi G, Agresti F, Maddalena A, Lo Russo S. The problem of solid state hydrogen storage. Energy 2009;34:2087-91.

[46] Bogdanović B, Schwickardi M. Ti-doped alkali metal aluminium hydrides as potential novel reversible hydrogen storage materials. Journal of Alloys and Compounds 1997;253:1-9.

[47] Jain I, Jain P, Jain A. Novel hydrogen storage materials: A review of lightweight complex hydrides. Journal of Alloys and Compounds 2010;503:303-39.

[48] Song Y, Guo Z. Electronic structure, stability and bonding of the Li-NH hydrogen storage system. Physical Review B 2006;74:195120.

[49] Chen J, Kuriyama N, Xu Q, Takeshita HT, Sakai T. Reversible hydrogen storage via titanium-catalyzed LiAlH4 and Li3AlH6. Journal of Physical Chemistry B 2001;105:11214-20.

[50] Resan M, Hampton MD, Lomness JK, Slattery DK. Effects of various catalysts on hydrogen release and uptake characteristics of LiAlH4. International Journal of Hydrogen Energy 2005;30:1413-6.

[51] Orimo S-i, Nakamori Y, Kitahara G, Miwa K, Ohba N, Towata S-i, Züttel A. Dehydriding and rehydriding reactions of LiBH4. Journal of Alloys and Compounds 2005;404:427-30.

[52] Chen P, Xiong Z, Luo J, Lin J, Tan KL. Interaction of hydrogen with metal nitrides and imides. Nature 2002;420:302-4.

[53] Luo W. (LiNH2-MgH2): a viable hydrogen storage system. Journal of Alloys and Compounds 2004;381:284-7.

[54] Nakamori Y, Orimo S. Destabilization of Li-based complex hydrides. Journal of Alloys and Compounds 2004;370:271-5.

[55] Sudik A, Yang J, Halliday D, Wolverton C. Hydrogen storage properties in (LiNH2)2-LiBH4-(MgH2) X Mixtures (X= 0.0-1.0). Journal of Physical Chemistry C 2008;112:4384-90.

[56] Niemann MU, Srinivasan SS, Kumar A, Stefanakos EK, Goswami DY, McGrath K. Processing analysis of the ternary LiNH2-MgH2-LiBH4 system for hydrogen storage. International Journal of Hydrogen Energy 2009;34:8086-93.

[57] Borgschulte A, Callini E, Probst B, Jain A, Kato S, Friedrichs O, Remhof A, Bielmann M, Ramirez-Cuesta A, Züttel A. Impurity Gas Analysis of the Decomposition of Complex Hydrides. Journal of Physical Chemistry C 2011;115:17220-6.

[58] Callini E, Borgschulte A, Ramirez-Cuesta T, Zuttel A. Diborane release and structure distortion in borohydrides. Dalton Transactions 2012.

[59] Ichikawa T, Hanada N, Isobe S, Leng H, Fujii H. Mechanism of novel reaction from LiNH2 and LiH to Li2NH and H2 as a promising hydrogen storage system. Journal of Physical Chemistry B 2004;108:7887-92.

[60] Luo W, Stewart K. Characterization of NH3 formation in desorption of Li-Mg-NH storage system. Journal of Alloys and Compounds 2007;440:357-61.

[61] Schüth F, Schmidt W. Microporous and mesoporous materials. Advanced Engineering Materials 2002;4:269-79.

[62] Yang Z, Xia Y, Mokaya R. Enhanced hydrogen storage capacity of high surface area zeolite-like carbon materials. Journal of the American Chemical Society 2007;129:1673-9.

[63] Schüth F. Endo-and exotemplating to create high-surface-area inorganic materials. Angewandte Chemie International Edition 2003;42:3604-22.

[64] Nijkamp M, Raaymakers J, Van Dillen A, De Jong K. Hydrogen storage using physisorption–materials demands. Applied Physics A: Materials Science & Processing 2001;72:619-23.

[65] Zhou L, Zhou Y, Sun Y. Studies on the mechanism and capacity of hydrogen uptake by physisorption-based materials. International Journal of Hydrogen Energy 2006;31:259-64.

[66] Imhof A, Pine D. Ordered macroporous materials by emulsion templating. Nature 1997;389:948-50.

[67] Cheetham AK, Férey G, Loiseau T. Open-framework inorganic materials. Angewandte Chemie International Edition 1999;38:3268-92.

[68] Rowsell JL, Yaghi OM. Metal–organic frameworks: a new class of porous materials. Microporous and Mesoporous Materials 2004;73:3-14.

[69] Davis ME. Ordered porous materials for emerging applications. Nature 2002;417:813-21.

[70] Jiang J-X, Cooper A, 2010. Microporous organic polymers: design, synthesis, and function in Functional Metal-Organic Frameworks: Gas Storage, Separation and Catalysis. Springer.

[71] Zhang H, Cooper AI. Synthesis and applications of emulsion-templated porous materials. Soft Matter 2005;1:107-13.

[72] Toyoda M, Nanbu Y, Kito T, Hiranob M, Inagaki M. Preparation and performance of anatase-loaded porous carbons for water purification. Desalination 2003;159:273-82.

[73] Shannon MA, Bohn PW, Elimelech M, Georgiadis JG, Mariñas BJ, Mayes AM. Science and technology for water purification in the coming decades. Nature 2008;452:301-10.

[74] Nakanishi K, Tanaka N. Sol–gel with phase separation. Hierarchically porous materials optimized for high-performance liquid chromatography separations. Accounts of Chemical Research 2007;40:863-73.

[75] Corma A. From microporous to mesoporous molecular sieve materials and their use in catalysis. Chemical Reviews 1997;97:2373-420.

[76] Horcajada P, Chalati T, Serre C, Gillet B, Sebrie C, Baati T, Eubank JF, Heurtaux D, Clayette P, Kreuz C. Porous metal-organic-framework nanoscale carriers as a potential platform for drug delivery and imaging. Nature Materials 2009;9:172-8.

[77] Horcajada P, Serre C, Vallet-Regí M, Sebban M, Taulelle F, Férey G. Metal-organic frameworks as efficient materials for drug delivery. Angewandte Chemie 2006;118:6120-4.

[78] Vallet-Regí M, Balas F, Arcos D. Mesoporous materials for drug delivery. Angewandte Chemie International Edition 2007;46:7548-58.

[79] Karageorgiou V, Kaplan D. Porosity of 3D biomaterial scaffolds and osteogenesis. Biomaterials 2005;26:5474-91.

[80] Sing K, Everett D, Haul R, Moscou L, Pierotti R, Rouquerol J, Siemieniewska T. Reporting physisorption data for gas/solid systems. Pure and Applied Chemistry 1985;57:603-19.

[81] Rosi NL, Eckert J, Eddaoudi M, Vodak DT, Kim J, O'Keeffe M, Yaghi OM. Hydrogen storage in microporous metal-organic frameworks. Science 2003;300:1127-9.

[82] Wong-Foy AG, Matzger AJ, Yaghi OM. Exceptional H2 saturation uptake in microporous metal-organic frameworks. Journal of the American Chemical Society 2006;128:3494-5.

[83] Dincă M, Long JR. Hydrogen storage in microporous metal-organic frameworks with exposed metal sites. Angewandte Chemie, International Edition 2008;47:6766-79.

[84] Han SS, Furukawa H, Yaghi OM, Goddard Iii WA. Covalent organic frameworks as exceptional hydrogen storage materials. Journal of the American Chemical Society 2008;130:11580-1.

[85] Ben T, Ren H, Ma S, Cao D, Lan J, Jing X, Wang W, Xu J, Deng F, Simmons JM. Targeted synthesis of a porous aromatic framework with high stability and exceptionally high surface area. Angewandte Chemie 2009;121:9621-4.

[86] Germain J, Fréchet JMJ, Svec F. Hypercrosslinked polyanilines with nanoporous structure and high surface area: potential adsorbents for hydrogen storage. Journal of Materials Chemistry 2007;17:4989-97.

[87] Germain J, Hradil J, Fréchet JMJ, Svec F. High surface area nanoporous polymers for reversible hydrogen storage. Chemistry of Materials 2006;18:4430-5.

[88] Wood CD, Tan B, Trewin A, Niu H, Bradshaw D, Rosseinsky MJ, Khimyak YZ, Campbell NL, Kirk R, Stöckel E. Hydrogen storage in microporous hypercrosslinked organic polymer networks. Chemistry of Materials 2007;19:2034-48.

[89] McKeown NB, Budd PM. Polymers of intrinsic microporosity (PIMs): organic materials for membrane separations, heterogeneous catalysis and hydrogen storage. Chemical Society Reviews 2006;35:675-83.

[90] McKeown NB, Gahnem B, Msayib KJ, Budd PM, Tattershall CE, Mahmood K, Tan S, Book D, Langmi HW, Walton A. Towards polymer-based hydrogen storage materials: Engineering ultramicroporous cavities within polymers of intrinsic microporosity. Angewandte Chemie, International Edition 2006;45:1804-7.

[91] Jiang JX, Su F, Trewin A, Wood CD, Niu H, Jones JTA, Khimyak YZ, Cooper AI. Synthetic control of the pore dimension and surface area in conjugated microporous polymer and copolymer networks. Journal of the American Chemical Society 2008;130:7710-20.

[92] Rzepka M, Lamp P, De La Casa-Lillo M. Physisorption of hydrogen on microporous carbon and carbon nanotubes. Journal of Physical Chemistry B 1998;102:10894-8.

[93] Schmitz B, Müller U, Trukhan N, Schubert M, Férey G, Hirscher M. Heat of adsorption for hydrogen in microporous high surface area materials. ChemPhysChem 2008;9:2181-4.

[94] Kajiura H, Tsutsui S, Kadono K, Kakuta M, Ata M, Murakami Y. Hydrogen storage capacity of commercially available carbon materials at room temperature. Applied physics letters 2003;82:1105-7.

[95] Hirscher M, Panella B. Nanostructures with high surface area for hydrogen storage. Journal of Alloys and Compounds 2005;404:399-401.

[96] Bhatia SK, Myers AL. Optimum conditions for adsorptive storage. Langmuir 2006;22:1688-700.

[97] Frost H, Düren T, Snurr RQ. Effects of surface area, free volume, and heat of adsorption on hydrogen uptake in metal-organic frameworks. Journal of Physical Chemistry B 2006;110:9565-70.

[98] Jhi SH, Ihm J. Developing high-capacity hydrogen storage materials via quantum simulations. MRS Bulletin 2011;36:198-204.

[99] Chung TCM, Jeong Y, Chen Q, Kleinhammes A, Wu Y. Synthesis of microporous boron-substituted carbon (B/C) materials using polymeric precursors for hydrogen physisorption. Journal of the American Chemical Society 2008;130:6668-9.

[100] Han SS, Goddard III WA. Lithium-doped metal-organic frameworks for reversible H2 storage at ambient temperature. Journal of the American Chemical Society 2007;129:8422-3.

[101] Li F, Zhao J, Johansson B, Sun L. Improving hydrogen storage properties of covalent organic frameworks by substitutional doping. International Journal of Hydrogen Energy 2010;35:266-71.

[102] Li Y, Yang RT. Significantly enhanced hydrogen storage in metal-organic frameworks via spillover. Journal of the American Chemical Society 2006;128:726-7.

[103] Wang L, Yang FH, Yang RT. Hydrogen storage properties of B-and N-doped microporous carbon. AIChE Journal 2009;55:1823-33.

[104] Zhou W, Wu H, Yildirim T. Enhanced H2 adsorption in isostructural metal-organic frameworks with open metal sites: Strong dependence of the binding strength on metal ions. Journal of the American Chemical Society 2008;130:15268-9.

[105] Farha OK, Eryazici I, Jeong NC, Hauser BG, Wilmer CE, Sarjeant AA, Snurr RQ, Nguyen ST, Yazaydın AOzr, Hupp JT. Metal-organic framework materials with ultrahigh surface areas: Is the sky the limit? Journal of the American Chemical Society 2012;134:15016-21.

[106] Yushin G, Dash R, Jagiello J, Fischer JE, Gogotsi Y. Carbide-derived carbons: Effect of pore size on hydrogen uptake and heat of adsorption. Advanced Functional Materials 2006;16:2288-93.

[107] Rowsell JL, Yaghi OM. Strategies for hydrogen storage in metal–organic frameworks. Angewandte Chemie International Edition 2005;44:4670-9.

[108] Lachawiec Jr AJ, Qi G, Yang RT. Hydrogen storage in nanostructured carbons by spillover: bridge-building enhancement. Langmuir 2005;21:11418-24.

[109] Ross D. Hydrogen storage: The major technological barrier to the development of hydrogen fuel cell cars. Vacuum 2006;80:1084-9.

[110] Paggiaro R, Bénard P, Polifke W. Cryo-adsorptive hydrogen storage on activated carbon. I: Thermodynamic analysis of adsorption vessels and comparison with liquid and compressed gas hydrogen storage. International Journal of Hydrogen Energy 2010;35:638-47.

[111] Paggiaro R, Michl F, Benard P, Polifke W. Cryo-adsorptive hydrogen storage on activated carbon. II: Investigation of the thermal effects during filling at cryogenic temperatures. International Journal of Hydrogen Energy 2010;35:648-59.

[112] MacDonald BD, Rowe AM. Impacts of external heat transfer enhancements on metal hydride storage tanks. International Journal of Hydrogen Energy 2006;31:1721-31.

[113] Pfeifer P, Wall C, Jensen O, Hahn H, Fichtner M. Thermal coupling of a high temperature PEM fuel cell with a complex hydride tank. International Journal of Hydrogen Energy 2009;34:3457-66.

[114] Sarkar A, Banerjee R. Net energy analysis of hydrogen storage options. International Journal of Hydrogen Energy 2005;30:867-77.

[115] Nikitin A, Ogasawara H, Mann D, Denecke R, Zhang Z, Dai H, Cho K, Nilsson A. Hydrogenation of single-walled carbon nanotubes. Physical Review Letters 2005;95:225507.

[116] Ganz E, Dornfeld M. Storage capacity of metal-organic and covalent-organic frameworks by hydrogen spillover. Journal of Physical Chemistry C 2012;116:3661-6.

[117] Psofogiannakis GM, Froudakis GE. Fundamental studies and perceptions on the spillover mechanism for hydrogen storage. Chemical Communications 2011;47:7933-43.

[118] Stadie NP, Purewal JJ, Ahn CC, Fultz B. Measurements of hydrogen spillover in platinum doped superactivated carbon. Langmuir 2010;26:15481-5.

[119] Luzan SM, Talyzin AV. Hydrogen adsorption in Pt catalyst/MOF-5 materials. Microporous and Mesoporous Materials 2010;135:201-5.

[120] Li B, Huang X, Gong R, Ma M, Yang X, Liang L, Tan B. Catalyzed hydrogen spillover for hydrogen storage on microporous organic polymers. International Journal of Hydrogen Energy 2012.

[121] Liu Y, Hu J, Wu G, Xiong Z, Chen P. Formation and equilibrium of ammonia in the Mg(NH2)2-2LiH hydrogen storage system. Journal of Physical Chemistry C 2008;112:1293-8.

[122] Uribe FA, Gottesfeld S, Zawodzinski TA. Effect of ammonia as potential fuel impurity on proton exchange membrane fuel cell performance. Journal of the Electrochemical Society 2002;149:A293-A6.

[123] Ikeda S, Kuriyama N, Kiyobayashi T. Simultaneous determination of ammonia emission and hydrogen capacity variation during the cyclic testing for LiNH2-LiH hydrogen storage system. International Journal of Hydrogen Energy 2008;33:6201-4.

[124] Serp P, Castillejos E. Catalysis in carbon nanotubes. ChemCatChem 2009;2:41-7.

[125] Meunier V, Kephart J, Roland C, Bernholc J. Ab initio investigations of lithium diffusion in carbon nanotube systems. Physical Review Letters 2002;88:75506.

[126] Broom DP. The accuracy of hydrogen sorption measurements on potential storage materials. International Journal of Hydrogen Energy 2007;32:4871-88.

[127] Zlotea C, Moretto P, Steriotis T. A Round Robin characterisation of the hydrogen sorption properties of a carbon based material. International Journal of Hydrogen Energy 2009;34:3044-57.

[128] Suryanarayana C. Mechanical alloying and milling. Progress in Materials Science 2001;46:1-184.

[129] Murty B, Ranganathan S. Novel materials synthesis by mechanical alloying/milling. International Materials Reviews 1998;43:101-41.

[130] Snyder JC, 1968. Preparation of metal hydrides. US Patent 3,387,933.

[131] Markmaitree T, Ren R, Shaw LL. Enhancement of lithium amide to lithium imide transition via mechanical activation. J Phys Chem B 2006;110:20710-8.

[132] Liu Y, Zhong K, Luo K, Gao M, Pan H, Wang Q. Size-dependent kinetic enhancement in hydrogen absorption and desorption of the Li-Mg-N-H system. Journal of the American Chemical Society 2009;131:1862-70.

[133] Varin R, Jang M, Polanski M. The effects of ball milling and molar ratio of LiH on the hydrogen storage properties of nanocrystalline lithium amide and lithium hydride ($LiNH_2$ + LiH) system. J Alloys Compd 2010;491:658-67.

[134] Shaw LL, Ren R, Markmaitree T, Osborn W. Effects of mechanical activation on dehydrogenation of the lithium amide and lithium hydride system. Journal of Alloys and Compounds 2008;448:263-71.

[135] Shahi RR, Yadav T, Shaz M, Srivastava O. Effects of mechanical milling on desorption kinetics and phase transformation of LiNH2/MgH2 mixture. International Journal of Hydrogen Energy 2008;33:6188-94.

[136] Fritsch Pulverisette P6, [cited 2013 March 30]; Available from: http://www.fritsch-milling.com/products/milling/planetary-mills/pulverisette-6-classic-line/.

[137] Innovative Technology, [cited 2013 March 30]; Available from: http://www.gloveboxes.com/.

[138] Coats A, Redfern J. Thermogravimetric analysis. A review. Analyst 1963;88:906-24.

[139] TA Instruments SDT Q600, [cited 2013 March 30]; Available from: http://www.tainstruments.com/product.aspx?siteid=11&id=22&n=1.

[140] Niemann, M.U. 2009. Development and investigation of novel nanostructures and complex hydrides for hydrogen storage [electronic resource]. PhD Dissertation, University of South Florida.

[141] Suryanarayana C, Norton MG, 1998. X-ray diffraction: a practical approach. Plenum Publishing Corporation.

[142] The International Centre for Diffraction Data - ICDD, [cited 2013 March 30]; Available from: http://www.icdd.com/.

[143] Reibenspies JH, Bhuvanesh N. A side-loading hermetic sample holder for X-ray powder diffraction. Powder Diffraction 2009;24:56-8.

[144] Patterson A. The Scherrer formula for X-ray particle size determination. Physical Review 1939;56:978.

[145] Goldstein J, Newbury DE, Joy DC, Lyman CE, Echlin P, Lifshin E, Sawyer L, Michael JR, 2003. Scanning electron microscopy and X-ray microanalysis. Springer.

[146] Williams DB, Carter CB, 1996. The Transmission Electron Microscope. Springer.

[147] Griffiths P, De Haseth JA, 2007. Fourier transform infrared spectrometry. Wiley-Interscience.

[148] Dillon AC, Yudasaka M, Dresselhaus MS. Employing Raman spectroscopy to qualitatively evaluate the purity of carbon single-wall nanotube materials. Journal of Nanoscience and Nanotechnology 2004;4:691-703.

[149] Olympus XI 71, [cited 2013 March 30]; Available from: http://www.olympusamerica.com/seg_section/product.asp?product=1023.

[150] Coheren Inc. Innova 70, [cited 2013 March 30]; Available from: http://www.coherent.com/products/?354/Innova-70.

[151] MKS Instruments, [cited 2013 March 30]; Available from: http://www.mksinst.com/product/product.aspx?ProductID=195.

[152] Quantachrome AS1C, [cited 2013 March 30]; Available from: http://www.quantachrome.com/gassorption/retired/autosorb1_series.html.

[153] Setaram Instrumentation, [cited 2013 March 30]; Available from: http://www.setaram.com/PCTPro-E-E.htm.

[154] Lowell S, Shields JE, Thomas MA, Thommes M, 2006. Characterization of porous solids and powders: surface area, pore size and density. Springer.

[155] Rouquerol J, Rouquerol F, Sing KS, 1998. Adsorption by powders and porous solids: Principles, Methodology and Applications. Academic press.

[156] Webb PA, Orr C, 1997. Analytical methods in fine particle technology. Micromeritics Norcross, GA.

[157] Schlapbach L, Züttel A. Hydrogen-storage materials for mobile applications. Nature 2001;414:353-8.

[158] Züttel A. Materials for hydrogen storage. Materials today 2003;6:24-33.

[159] Kubas GJ. Fundamentals of H2 binding and reactivity on transition metals underlying hydrogenase function and H2 production and storage. Chemical Reviews 2007;107:4152-205.

[160] Prins R. Hydrogen spillover. Facts and fiction. Chemical Reviews 2012;112:2714–38.

[161] Sermon P, Bond G. Hydrogen spillover. Catalysis Reviews - Science and Engineering 1974;8:211-39.

[162] Conner Jr WC, Falconer JL. Spillover in heterogeneous catalysis. Chemical Reviews 1995;95:759-88.

[163] Rozanov VV, Krylov OV. Hydrogen spillover in heterogeneous catalysis. Russian Chemical Reviews 1997;66:107-19.

[164] Contescu CI, Bhat VV, Gallego NC. Hydrogen spillover: Its 'diffusion' from catalysis to hydrogen storage community. Preprints of Papers - American Chemical Society, Division of Fuel Chemistry 2009;54:382-3.

[165] Psofogiannakis GM, Froudakis GE. DFT study of the hydrogen spillover mechanism on Pt-doped graphite. Journal of Physical Chemistry C 2009;113:14908-15.

[166] Lee K, Kim YH, Sun Y, West D, Zhao Y, Chen Z, Zhang S. Hole-mediated hydrogen spillover mechanism in metal-organic frameworks. Physical Review Letters 2010;104:236101.

[167] Psofogiannakis GM, Froudakis GE. Theoretical explanation of hydrogen spillover in metal-organic frameworks. Journal of Physical Chemistry C 2011;115:4047-53.

[168] Wang L, Yang RT. Hydrogen storage on carbon-based adsorbents and storage at ambient temperature by hydrogen spillover. Catalysis Reviews - Science and Engineering 2010;52:411-61.

[169] Wang L, Yang RT. New sorbents for hydrogenstorage by hydrogen spillover–a review. Energy & Environmental Science 2008;1:268-79.

[170] Mitchell PCH, Ramirez-Cuesta AJ, Parker SF, Tomkinson J, Thompsett D. Hydrogen spillover on carbon-supported metal catalysts studied by inelastic neutron scattering. Surface vibrational states and hydrogen riding modes. Journal of Physical Chemistry B 2003;107:6838-45.

[171] Tsao CS, Liu Y, Chuang HY, Tseng HH, Chen TY, Chen CH, Yu MS, Li Q, Lueking AD, Chen SH. Hydrogen spillover effect of Pt-doped activated carbon studied by inelastic neutron scattering. Journal of Physical Chemistry Letters 2011;2:2322-5.

[172] Tsao CS, Liu Y, Li M, Zhang Y, Leao JB, Chang HW, Yu MS, Chen SH. Neutron scattering methodology for absolute measurement of room-temperature hydrogen storage capacity and evidence for spillover effect in a Pt-doped activated carbon. Journal of Physical Chemistry Letters 2010;1:1569-73.

[173] Contescu CI, Brown CM, Liu Y, Bhat VV, Gallego NC. Detection of hydrogen spillover in palladium-modified activated carbon fibers during hydrogen adsorption. Journal of Physical Chemistry C 2009;113:5886-90.

[174] Zhang G, Qi P, Wang X, Lu Y, Mann D, Li X, Dai H. Hydrogenation and hydrocarbonation and etching of single-walled carbon nanotubes. Journal of the American Chemical Society 2006;128:6026-7.

[175] Bhowmick R, Rajasekaran S, Friebel D, Beasley C, Jiao L, Ogasawara H, Dai H, Clemens B, Nilsson A. Hydrogen spillover in Pt-single-walled carbon nanotube composites: Formation of stable C− H bonds. Journal of the American Chemical Society 2011;133:5580-6.

[176] Lin C, Yang Z, Xu T, Zhao Y. An in situ electrical study on primary hydrogen spillover from nanocatalysts to amorphous carbon support. Applied Physics Letters 2008;93:233110.

[177] Miller MA, Wang CY, Merrill GN. Experimental and theoretical investigation into hydrogen storage via spillover in IRMOF-8. Journal of Physical Chemistry C 2009;113:3222-31.

[178] Campesi R, Cuevas F, Latroche M, Hirscher M. Hydrogen spillover measurements of unbridged and bridged metal–organic frameworks—revisited. Physical Chemistry Chemical Physics 2010;12:10457-9.

[179] Li Y, Wang L, Yang RT. Response to "hydrogen adsorption in Pt catalyst/MOF-5 materials" by Luzan and Talyzin. Microporous and Mesoporous Materials 2010;135:206-8.

[180] Luzan SM, Talyzin AV. Comment to the "Response to "Hydrogen adsorption in Pt catalyst/MOF-5 materials"" by Li et al. Microporous and Mesoporous Materials 2011;139:216-8.

[181] Hirscher M. Remarks about spillover and hydrogen adsorption - Comments on the contributions of A.V. Talyzin and R.T. Yang. Microporous and Mesoporous Materials 2010;135:209-10.

[182] Ardelean O, Blanita G, Borodi G, Mihet M, Coros M, Lupu D. On the enhancement of hydrogen uptake by IRMOF-8 composites with Pt/carbon catalyst. International Journal of Hydrogen Energy 2012.

[183] Kiyobayashi T, Takeshita HT, Tanaka H, Takeichi N, Züttel A, Schlapbach L, Kuriyama N. Hydrogen adsorption in carbonaceous materials - How to determine the storage capacity accurately. Journal of Alloys and Compounds 2002;330:666-9.

[184] Li Y, Yang RT. Hydrogen storage on platinum nanoparticles doped on superactivated carbon. Journal of Physical Chemistry C 2007;111:11086-94.

[185] Contescu CI, van Benthem K, Li S, Bonifacio CS, Pennycook SJ, Jena P, Gallego NC. Single Pd atoms in activated carbon fibers and their contribution to hydrogen storage. Carbon 2011;49:4050-8.

[186] Zielinski M, Wojcieszak R, Monteverdi S, Mercy M, Bettahar M. Hydrogen storage on nickel catalysts supported on amorphous activated carbon. Catalysis Communications 2005;6:777-83.

[187] Kim HS, Lee H, Han KS, Kim JH, Song MS, Park MS, Lee JY, Kang JK. Hydrogen storage in Ni nanoparticle-dispersed multiwalled carbon nanotubes. Journal of Physical Chemistry B 2005;109:8983-6.

[188] Yang FH, Lachawiec Jr AJ, Yang RT. Adsorption of spillover hydrogen atoms on single-wall carbon nanotubes. Journal of Physical Chemistry B 2006;110:6236-44.

[189] Nikitin A, Li X, Zhang Z, Ogasawara H, Dai H, Nilsson A. Hydrogen storage in carbon nanotubes through the formation of stable CH bonds. Nano Letters 2008;8:162-7.

[190] Li Y, Yang RT. Hydrogen storage in low silica type X zeolites. Journal of Physical Chemistry B 2006;110:17175-81.

[191] Li Y, Yang RT. Hydrogen storage in metal-organic frameworks by bridged hydrogen spillover. Journal of the American Chemical Society 2006;128:8136-7.

[192] Tsao CS, Yu MS, Wang CY, Liao PY, Chen HL, Jeng US, Tzeng YR, Chung TY, Wu HC. Nanostructure and hydrogen spillover of bridged metal-organic frameworks. Journal of the American Chemical Society 2009;131:1404-6.

[193] Li Y, Yang RT. Hydrogen storage in metal-organic and covalent-organic frameworks by spillover. AIChE Journal 2008;54:269-79.

[194] Hasell T, Wood CD, Clowes R, Jones JTA, Khimyak YZ, Adams DJ, Cooper AI. Palladium nanoparticle incorporation in conjugated microporous polymers by supercritical fluid processing. Chemistry of Materials 2009;22:557-64.

[195] Sidorov S, Bronstein L, Davankov V, Tsyurupa M, Solodovnikov S, Valetsky P, Wilder E, Spontak R. Cobalt nanoparticle formation in the pores of hyper-cross-linked polystyrene: Control of nanoparticle growth and morphology. Chemistry of Materials 1999;11:3210-5.

[196] Sidorov S, Volkov I, Davankov V, Tsyurupa M, Valetsky P, Bronstein L, Karlinsey R, Zwanziger J, Matveeva V, Sulman E. Platinum-containing hyper-cross-linked polystyrene as a modifier-free selective catalyst for L-sorbose oxidation. Journal of the American Chemical Society 2001;123:10502-10.

[197] Bronstein LM, Goerigk G, Kostylev M, Pink M, Khotina IA, Peter M, Matveeva VG, Sulman EM, Sulman MG, Bykov AV. Structure and catalytic properties of Pt-modified hyper-cross-linked polystyrene exhibiting hierarchical porosity. Journal of Physical Chemistry B 2004;108:18234-42.

[198] Aberg CM, Seyam MA, Lassell SA, Bronstein LM, Spontak RJ. In situ growth of Pd nanoparticles in crosslinked polymer matrices. Macromolecular Rapid Communications 2008;29:1926-31.

[199] Tsao CS, Tzeng YR, Yu MS, Wang CY, Tseng HH, Chung TY, Wu HC, Yamamoto T, Kaneko K, Chen SH. Effect of catalyst size on hydrogen storage capacity of Pt-impregnated active carbon via spillover. Journal of Physical Chemistry Letters 2010;1:1060-3.

[200] Chen H, Yang RT. Catalytic effects of TiF3 on hydrogen spillover on Pt/carbon for hydrogen storage. Langmuir 2010;26:15394-8.

[201] Chen Y, Liu Q, Yan Y, Cheng X, Liu Y. Influence of sample cell physisorption on measurements of hydrogen storage of carbon materials using a Sieverts apparatus. Carbon 2010;48:714-20.

[202] Langford Jt, Wilson A. Scherrer after sixty years: a survey and some new results in the determination of crystallite size. Journal of Applied Crystallography 1978;11:102-13.

[203] Zlotea C, Campesi R, Cuevas F, Leroy E, Dibandjo P, Volkringer C, Loiseau T, Férey G, Latroche M. Pd nanoparticles embedded into a metal-organic framework: synthesis, structural characteristics, and hydrogen sorption properties. Journal of the American Chemical Society 2010;132:2991-7.

[204] Mailhot B, Gardette JL. Polystyrene photooxidation. 1. Identification of the IR-absorbing photoproducts formed at short and long wavelengths. Macromolecules 1992;25:4119-26.

[205] Wilhelm C, Gardette JL. Infrared identification of carboxylic acids formed in polymer photooxidation. Journal of Applied Polymer Science 1994;51:1411-20.

[206] Stuckert NR, Wang L, Yang RT. Characteristics of hydrogen storage by spillover on Pt-doped carbon and catalyst-bridged metal organic framework. Langmuir 2010.

[207] Wang L, Yang FH, Yang RT, Miller MA. Effect of surface oxygen groups in carbons on hydrogen storage by spillover. Industrial & Engineering Chemistry Research 2009;48:2920-6.

[208] Orimo S, Nakamori Y, Eliseo JR, Zuettel A, Jensen CM. Complex hydrides for hydrogen storage. Chemical Reviews 2007;107:4111-32.

[209] Schüth F, Bogdanović B, Felderhoff M. Light metal hydrides and complex hydrides for hydrogen storage. Chemical Communications 2004:2249-58.

[210] Hu YH, Ruckenstein E. Ultrafast reaction between LiH and NH3 during H2 storage in Li3N. Journal of Physical Chemistry A 2003;107:9737-9.

[211] Srinivasan S, McElwee-White L, Stefanakos E, Goswami Y, Dumbris S, 2006. Thermal and Volumetric Studies of Complex Chemical Hydrides: Li-modified/Ti-doped Mg2FeH6, Sonicated LiNH2/LiH and Zn-doped NaBH4, Materials Research Society Symposium Proceedings. Cambridge Univ Press, pp. A07-3.1.

[212] Luo W, Rönnebro E. Towards a viable hydrogen storage system for transportation application. Journal of Alloys and Compounds 2005;404:392-5.

[213] Luo W, Sickafoose S. Thermodynamic and structural characterization of the Mg-Li-NH hydrogen storage system. Journal of Alloys and Compounds 2006;407:274-81.

[214] Liang C, Liu Y, Fu H, Ding Y, Gao M, Pan H. Li-Mg-N-H-based combination systems for hydrogen storage. Journal of Alloys and Compounds 2011;509:7844-53.

[215] Leng HY, Ichikawa T, Hino S, Hanada N, Isobe S, Fujii H. New metal-NH system composed of Mg (NH2)2 and LiH for hydrogen storage. Journal of Physical Chemistry B 2004;108:8763-5.

[216] Xiong Z, Hu J, Wu G, Chen P, Luo W, Gross K, Wang J. Thermodynamic and kinetic investigations of the hydrogen storage in the Li-Mg-NH system. Journal of Alloys and Compounds 2005;398:235-9.

[217] Chen P, Xiong Z, Yang L, Wu G, Luo W. Mechanistic investigations on the heterogeneous solid-state reaction of magnesium amides and lithium hydrides. Journal of Physical Chemistry B 2006;110:14221-5.

[218] David WIF, Jones MO, Gregory DH, Jewell CM, Johnson SR, Walton A, Edwards PP. A mechanism for non-stoichiometry in the lithium amide/lithium imide hydrogen storage reaction. Journal of the American Chemical Society 2007;129:1594-601.

[219] Borgschulte A, Jones MO, Callini E, Probst B, Kato S, Züttel A, David WIF, Orimo S. Surface and bulk reactions in borohydrides and amides. Energy & Environmental Science 2012.

[220] Wu H. Structure of ternary imide Li2Ca(NH)2 and hydrogen storage mechanisms in amide - hydride system. Journal of the American Chemical Society 2008;130:6515-22.

[221] Li W, Wu G, Xiong Z, Feng YP, Chen P. Li+ ionic conductivities and diffusion mechanisms in Li-based imides and lithium amide. Physical Chemistry Chemical Physics 2012;14:1596.

[222] Matsuo M, Orimo S. Lithium fast-ionic conduction in complex hydrides: Review and prospects. Advanced Energy Materials 2011;1:161-72.

[223] Nishidate K, Hasegawa M. Energetics of lithium ion adsorption on defective carbon nanotubes. Physical Review B 2005;71:245418.

[224] Li J, Li H, Liang X, Zhang S, Zhao T, Xia D, Wu Z. First principles study on the diffusion of alkali-metal ions on the armchair single-wall nanotubes. Journal of Physical Chemistry A 2009;113:791-6.

[225] Song B, Yang J, Zhao J, Fang H. Intercalation and diffusion of lithium ions in a carbon nanotube bundle by ab initio molecular dynamics simulations. Energy & Environmental Science 2011;4:1379-84.

[226] Markmaitree T, Osborn W, Shaw LL. Comparisons between MgH2-and LiH-containing systems for hydrogen storage applications. International Journal of Hydrogen Energy 2008;33:3915-24.

[227] Markmaitree T, Osborn W, Shaw LL. Comparative studies of reaction rates of NH3 with MgH2 and LiH. Journal of Power Sources 2008;180:535-8.

[228] Luo W, Wang J, Stewart K, Clift M, Gross K. Li-Mg-NH: Recent investigations and development. Journal of Alloys and Compounds 2007;446:336-41.

[229] Ikeda S, Tokoyoda K, Kiyobayashi T, Kuriyama N. Cyclic properties and ammonia by-product emission of Li/Mg-N-H hydrogen storage material. International Journal of Hydrogen Energy 2011;36:8373-80.

[230] Yin SF, Xu BQ, Ng CF, Au CT. Nano Ru/CNTs: a highly active and stable catalyst for the generation of CO< sub> x</sub>-free hydrogen in ammonia decomposition. Applied Catalysis B: Environmental 2004;48:237-41.

[231] Yin SF, Xu BQ, Zhou XP, Au CT. A mini-review on ammonia decomposition catalysts for on-site generation of hydrogen for fuel cell applications. Applied Catalysis A: General 2004;277:1-9.

[232] Choudhary TV, Sivadinarayana C, Goodman DW. Catalytic ammonia decomposition: COx-free hydrogen production for fuel cell applications. Catalysis Letters 2001;72:197-201.

[233] Li L, Zhu ZH, Yan ZF, Lu GQ, Rintoul L. Catalytic ammonia decomposition over Ru/carbon catalysts: The importance of the structure of carbon support. Applied Catalysis A: General 2007;320:166-72.

[234] Garcia-Garcia FR, Alvarez-Rodriguez J, Rodriguez-Ramos I, Guerrero-Ruiz A. The use of carbon nanotubes with and without nitrogen doping as support for ruthenium catalysts in the ammonia decomposition reaction. Carbon 2010;48:267-76.

[235] Jacobsen C, Dahl S, Clausen BS, Bahn S, Logadottir A, Nørskov JK. Catalyst design by interpolation in the periodic table: bimetallic ammonia synthesis catalysts. Journal of the American Chemical Society 2001;123:8404.

[236] Logadottir A, Rod TH, Nørskov JK, Hammer B, Dahl S, Jacobsen CJH. The brønsted–evans–polanyi relation and the volcano plot for ammonia synthesis over transition metal catalysts. Journal of Catalysis 2001;197:229-31.

[237] Wu C, Cheng HM. Effects of carbon on hydrogen storage performances of hydrides. Journal of Materials Chemistry 2010;20:5390-400.

[238] Chen Y, Wang P, Liu C, Cheng HM. Improved hydrogen storage performance of Li-Mg-NH materials by optimizing composition and adding single-walled carbon nanotubes. International Journal of Hydrogen Energy 2007;32:1262-8.

[239] Ma LP, Dai HB, Liang Y, Kang XD, Fang ZZ, Wang PJ, Wang P, Cheng HM. Catalytically enhanced hydrogen storage properties of Mg(NH2)2 + 2LiH material by graphite-supported Ru nanoparticles. Journal of Physical Chemistry C 2008;112:18280-5.

[240] Hu J, Fichtner M. Formation and stability of ternary imides in the Li-Mg-N-H hydrogen storage system. Chemistry of Materials 2009;21:3485-90.

[241] Markmaitree T, Shaw LL. Synthesis and hydriding properties of Li2Mg(NH)2. Journal of Power Sources 2010;195:1984-91.

[242] Ma LP, Wang P, Dai HB, Cheng HM. Catalytically enhanced dehydrogenation of Li-Mg-NH hydrogen storage material by transition metal nitrides. Journal of Alloys and Compounds 2009;468:L21-L4.

[243] Rijssenbeek J, Gao Y, Hanson J, Huang Q, Jones C, Toby B. Crystal structure determination and reaction pathway of amide–hydride mixtures. Journal of Alloys and Compounds 2008;454:233-44.

[244] Leng H, Ichikawa T, Fujii H. Hydrogen storage properties of Li-Mg-N-H systems with different ratios of LiH/Mg(NH2)2. Journal of Physical Chemistry B 2006;110:12964-8.

[245] Okamoto K, Tokoyoda K, Ichikawa T, Fujii H. A process for synthesizing the Li-Mg-N-H hydrogen storage system from Mg and LiNH2. Journal of Alloys and Compounds 2007;432:289-92.

[246] Yang J, Sudik A, Wolverton C. Activation of hydrogen storage materials in the Li-Mg-NH system: Effect on storage properties. Journal of Alloys and Compounds 2007;430:334-8.

[247] Lordi V, Yao N, Wei J. Method for supporting platinum on single-walled carbon nanotubes for a selective hydrogenation catalyst. Chemistry of Materials 2001;13:733-7.

[248] Demirocak DE, Srinivasan SS, Ram MK, Goswami DY, Stefanakos EK. Volumetric hydrogen sorption measurements–Uncertainty error analysis and the importance of thermal equilibration time. International Journal of Hydrogen Energy 2013;38:1469-77.

[249] Castillo VA, Kuhn JN. Role of the Ni: Fe ratio in ethylene hydrogenation activity for silica-supported Ni–Fe clusters prepared by dendrimer-templating. Journal of Physical Chemistry C 2012;116:8627-33.

[250] Varin RA, Jang M, Polanski M. The effects of ball milling and molar ratio of LiH on the hydrogen storage properties of nanocrystalline lithium amide and lithium hydride (LiNH2 + LiH) system. Journal of Alloys and Compounds 2010;491:658-67.

[251] Nayebossadri S. Kinetic rate-limiting steps in dehydrogenation of Li-N-H and Li-Mg-N-H systems - Effects of elemental Si and Al. International Journal of Hydrogen Energy 2011;36:8335-43.

[252] Eswaramoorthy M, Sen R, Rao CNR. A study of micropores in single-walled carbon nanotubes by the adsorption of gases and vapors. Chemical Physics Letters 1999;304:207-10.

[253] Peigney A, Laurent C, Flahaut E, Bacsa RR, Rousset A. Specific surface area of carbon nanotubes and bundles of carbon nanotubes. Carbon 2001;39:507-14.

[254] Hrbek J, Van Campen DG, Malik IJ. The early stages of ruthenium oxidation. Journal of Vacuum Science & Technology A 1995;13:1409-12.

[255] Surnev L, Rangelov G, Bliznakov G. Interaction of oxygen with a Ru (OO1) surface. Surface Science 1985;159:299-310.

[256] Karim AM, Prasad V, Mpourmpakis G, Lonergan WW, Frenkel AI, Chen JG, Vlachos DG. Correlating particle size and shape of supported Ru/γ-Al2O3 catalysts with NH3 decomposition activity. Journal of the American Chemical Society 2009;131:12230-9.

[257] Pierard N, Fonseca A, Colomer JF, Bossuot C, Benoit JM, Van Tendeloo G, Pirard JP, Nagy JB. Ball milling effect on the structure of single-wall carbon nanotubes. Carbon 2004;42:1691-7.

[258] Rubio N, Fabbro C, Herrero MA, de la Hoz A, Meneghetti M, Fierro JLG, Prato M, Vázquez E. Ball-milling modification of single-walled carbon nanotubes: Purification, cutting, and functionalization. Small 2011;7:665-74.

[259] Lee J, Jeong T, Heo J, Park SH, Lee DH, Park JB, Han HS, Kwon YN, Kovalev I, Yoon SM. Short carbon nanotubes produced by cryogenic crushing. Carbon 2006;44:2984-9.

[260] Liu F, Zhang X, Cheng J, Tu J, Kong F, Huang W, Chen C. Preparation of short carbon nanotubes by mechanical ball milling and their hydrogen adsorption behavior. Carbon 2003;41:2527-32.

[261] Dresselhaus MS, Dresselhaus G, Saito R, Jorio A. Raman spectroscopy of carbon nanotubes. Physics Reports 2005;409:47-99.

[262] Alimi K, Zaidi B, Chemek M. About grafting of single-walled carbon nanotubes on the oligo-N-vinyl carbazole and copolymer involving N-vinylcarbazole and hexylthiophene. Carbon Nanotubes 2011:301-30.

[263] Von Zeppelin F, Haluska M, Hirscher M. Thermal desorption spectroscopy as a quantitative tool to determine the hydrogen content in solids. Thermochimica acta 2003;404:251-8.

[264] Murray LJ, Dincă M, Long JR. Hydrogen storage in metal-organic frameworks. Chemical Society Reviews 2009;38:1294-314.

[265] Hirscher M, Becher M, Haluska M, Quintel A, Skakalova V, Choi YM, Dettlaff-Weglikowska U, Roth S, Stepanek I, Bernier P, Leonhardt A, Fink J. Hydrogen storage in carbon nanostructures. Journal of Alloys and Compounds 2002;330:654-8.

[266] Cho SJ, Song KS, Kim JW, Kim TH, Choo K. Hydrogen sorption in HCl-treated polyaniline and polypyrrole: new potential hydrogen storage media. Fuel Chemistry Division Preprints 2002;47:790-1.

[267] Panella B, Kossykh L, Dettlaff-Weglikowska U, Hirscher M, Zerbi G, Roth S. Volumetric measurement of hydrogen storage in HCl-treated polyaniline and polypyrrole. Synthetic Metals 2005;151:208-10.

[268] Broom DP, Moretto P. Accuracy in hydrogen sorption measurements. Journal of Alloys and Compounds 2007;446:687-91.

[269] Gross KJ, Carrington KR, Barcelo S, Karkamkar A, Purewal J, Ma S, Zhou HC, Dentzer P, Ott K, Burrell T, Semeslberger T, Pivak Y, Dam B, Chandra D, 2012. Recommended best practices for the characterization of storage properties of hydrogen storage materials (ver. 3.34, Feb 21, 2012).

[270] Lee YW, Clemens BM, Gross KJ. Novel Sieverts' type volumetric measurements of hydrogen storage properties for very small sample quantities. Journal of Alloys and Compounds 2008;452:410-3.

[271] Blach TP, Gray E. Sieverts apparatus and methodology for accurate determination of hydrogen uptake by light-atom hosts. Journal of Alloys and Compounds 2007;446:692-7.

[272] Langohr D, Berthon-Fabry S, Gonzalez-Aguilar J, Fulcheri L, Achard P. Development of a volumetric method-experimental test bench for hydrogen storage characterization. International Journal of Hydrogen Energy 2007;32:1846-54.

[273] Belmabkhout Y, Frere M, De Weireld G. High-pressure adsorption measurements. A comparative study of the volumetric and gravimetric methods. Measurement Science and Technology 2004;15:848.

[274] Checchetto R, Trettel G, Miotello A. Sievert-type apparatus for the study of hydrogen storage in solids. Measurement Science and Technology 2004;15:127.

[275] Moffat RJ. Describing the uncertainties in experimental results. Experimental thermal and fluid science 1988;1:3-17.

[276] Maggs FAP, Schwabe PH, Williams JH. Adsorption of helium on carbons: influence on measurement of density. Nature 1960;186:956-8.

[277] Kini KA, Stacy WO. The adsorption of helium by carbonaceous solids. Carbon 1963;1:17-24.

[278] Malbrunot P, Vidal D, Vermesse J, Chahine R, Bose TK. Adsorbent helium density measurement and its effect on adsorption isotherms at high pressure. Langmuir 1997;13:539-44.

[279] Coleman HW, Steele WG, 2009. Experimentation, validation, and uncertainty analysis for engineers. Wiley.

[280] Lemmon EW, Huber ML, McLinden MO. NIST Standard Reference Database 23: Reference Fluid Thermodynamic and Transport Properties-REFPROP, Version 9.0, National Institute of Standards and Technology, Standard Reference Data Program, Gaithersburg, 2010.

[281] Moldover MR, Trusler JPM, Edwards TJ, Mehl JB, Davis RS. Measurement of the universal gas constant R using a spherical acoustic resonator. Journal of Research of the National Bureau of Standards 1988;93:85-144.

[282] Lemmon EW, Huber ML, Leachman JW. Revised standardized equation for hydrogen gas densities for fuel consumption applications. Journal of Research of the National Institute of Standards and Technology 2008;113:341-50.

[283] Lemmon EW. Personal communication. Oct 24, 2012.

Appendices

Appendix A. Uncertainty in the Compressibility Factor of Hydrogen, Z(P,T), due to Uncertainty in Pressure and Temperature Readings

Real gas equation of state (Eq. (A.1)) and the constants a_i, b_i and c_i in the equation of state are taken from Lemmon et al. [282].

$$Z(P,T)=1+\sum_{i=1}^{9} a_i \left(\frac{100\ \mathrm{K}}{T}\right)^{b_i} \left(\frac{P}{1\ \mathrm{MPa}}\right)^{c_i} \tag{A.1}$$

Uncertainty in Z(P,T) due to uncertainty in pressure and temperature readings can be expressed as follows,

$$\left(U_{Z(P,T)}\right)^2=\left(\frac{\partial Z(P,T)}{\partial T}\right)^2 (U_T)^2+\left(\frac{\partial Z(P,T)}{\partial P}\right)^2 (U_P)^2 \tag{A.2}$$

Dividing each term in Eq. (A.2) by $[Z(P,T)]^2$ and multiplying the first and second terms on the right-hand side by $\left(\frac{T}{T}\right)^2$ and $\left(\frac{P}{P}\right)^2$, respectively, we can obtain,

$$\left(\frac{U_{Z(P,T)}}{Z(P,T)}\right)^2 = \left(\frac{T}{Z(P,T)}\frac{\partial Z(P,T)}{\partial T}\right)^2 \left(\frac{U_T}{T}\right)^2 + \left(\frac{P}{Z(P,T)}\frac{\partial Z(P,T)}{\partial P}\right)^2 \left(\frac{U_P}{P}\right)^2 \tag{A.3}$$

where partial derivatives of Z(P,T) with respect to T and P are given in Eqs. (A.4) and (A.5), respectively.

$$\frac{\partial Z(P,T)}{\partial T}=\sum_{i=1}^{9} a_i b_i \left(\frac{100\ \mathrm{K}}{T}\right)^{b_i-1} \left(-\frac{100\ \mathrm{K}}{T^2}\right) \left(\frac{P}{1\ \mathrm{MPa}}\right)^{c_i} \tag{A.4}$$

$$\frac{\partial Z(P,T)}{\partial P}=\sum_{i=1}^{9} a_i \left(\frac{100\ \mathrm{K}}{T}\right)^{b_i} c_i \left(\frac{P}{1\ \mathrm{MPa}}\right)^{c_i-1} \tag{A.5}$$

By inserting Eq. (A.5), Eq. (A.6), $\frac{U_T}{T}=0.01$ and $\frac{U_P}{P}=0.01$ into Eq. (A.3) we can calculate the uncertainty in the compressibility factor Z(P,T) due to uncertainty in pressure and temperature readings.

Appendix A (Continued)

At 10 MPa and 300 K, the uncertainty in Z(P,T) is 0.07 %, and the uncertainty in the equation of state (i.e., Eq. (A.1)) is 0.01 % [282]. Therefore, the overall uncertainty in Z(P,T) is,

$$\frac{U_{Z(P,T)}}{Z(P,T)} = \sqrt{(0.0007)^2 + (0.0001)^2} \cong 0.07\ \% \qquad (A.6)$$

Appendix B. Uncertainty in the Compressibility Factor of Helium, $Z^{He}(P,T)$

A helium equation of state (EOS) similar to the hydrogen EOS given in Eq. (A.1) is under development [283283]. Therefore, we assumed the uncertainty in Z^{He} due to uncertainty in temperature and pressure readings is the same as in hydrogen's compressibility factor (i.e., 0.07%) as given in Appendix A. On the other hand, helium EOS in REFPROP 8 software has a 0.1 % uncertainty. Hence, the total uncertainty in Z^{He} is calculated as follows,

$$\frac{U_{Z^{He}(P,T)}}{Z^{He}(P,T)} = \sqrt{(0.0007)^2+(0.001)^2} \cong 0.12\ \% \qquad \text{(B.1)}$$

Appendix C. Copyright Information

Elsevier gives permission to the authors to include their published articles (by full acknowledgment of the original published articles) in their thesis or dissertation[13]. See the footnotes on pages 1, 32 and 85 for acknowledgements of the original articles.

Table of Authors' Rights

	Preprint version (with a few exceptions- see below *)	Accepted Author Manuscript	Published Journal Articles
Use for classroom teaching by author or author's institution and presentation at a meeting or conference and distributing copies to attendees	Yes	Yes with full acknowledgement of final article	Yes with full acknowledgement of final article
Use for internal training by author's company	Yes	Yes with full acknowledgement of final article	Yes with full acknowledgement of final article
Distribution to colleagues for their research use	Yes	Yes	Yes
Use in a subsequent compilation of the author's works	Yes	Yes with full acknowledgement of final article	Yes with full acknowledgement of final article
Inclusion in a thesis or dissertation	Yes	Yes with full acknowledgement of final article	Yes with full acknowledgement of final article
Reuse of portions or extracts from the article in other works	Yes	Yes with full acknowledgement of final article	Yes with full acknowledgement of final article
Preparation of derivative works (other than for commercial purposes)	Yes	Yes with full acknowledgement of final article	Yes with full acknowledgement of final article
Preprint servers	Yes	Yes with the specific written permission of Elsevier	No

Figure C.1. Elsevier table of authors' rights.

[13] http://www.elsevier.com/authors/author-rights-and-responsibilities